Spectral Analysis of Breast Ultrasound Data with Application to Mass Sizing and Characterization

Rui Teixeira Ribeiro

Department of Engineering Science
St. Hilda's College
2014

This thesis is submitted to the Department of Engineering Science, University of Oxford, in partial fulfilment of the requirements for the degree of Doctor of Philosophy (DPhil) in Engineering Science. The thesis is entirely my own work and, except where otherwise stated, describes my own research.

Rui Teixeira Ribeiro, 2014 .

Abstract

Spectral Analysis of Breast Ultrasound Data with Application to Mass Sizing and Characterization

Rui A. F. Teixeira Ribeiro
DPhil in Engineering Science

Michaelmas Term, 2014
St. Hilda's College

Ultrasound is a commonly used imaging modality in diagnosis and pre-operative assessment of breast masses. However, radiologists often find it very difficult to correctly size masses using conventional ultrasound images. Consequently, there exists a strong need for more accurate sizing tools to avoid either the removal of an over-estimated amount of tissue or a second surgical procedure to remove margins involved by tumour not removed in the primary operation.

In this thesis, we propose a new method of processing the backscattered ultrasound signals from breast tissue (based on the Fourier spectral analysis) to better estimate the degree of echogenicity and generate parametric images where the visibility of breast mass boundaries is improved (SPV parametric image). Moreover, an algorithm is proposed to recover some anatomical structures (particularly, Cooper's ligaments) which are shadowed during the image acquisition process (LWSPV parametric image). The information from both algorithms is combined to generate a final SPV+LWSPV parametric image.

A 20-case pilot study was conducted on clinical data, which showed that the SPV+LWSPV parametric image added useful information to the B-mode image for clinical assessment in 85% of the cases (increase in diagnostic confidence in at least

one boundary). Moreover, in 35% of the cases, the SPV+LWSPV parametric image provided a better definition of the entire boundary. Note that the radiologist knew the final diagnosis from histopathology.

In addition, the SPV+LWSPV method has the advantage that it uses the I/Q data from a standard ultrasound equipment without the need for additional hardware.

On the basis of these facts, we believe there to be a case for further investigation of the SPV+LWSPV imaging as a useful clinical tool in the pre-operative assessment of breast mass boundaries.

Acknowledgements

I would like to thank Prof. Alison Noble for her guidance and support; Dr Ruth English, who followed the clinical component of this project; and everyone inside and outside academia that somehow made this work possible.

I would also like to thank *Fundação para a Ciência e a Tecnologia (FCT)* – a Portuguese Governmental Body – for financially supporting my DPhil research project: grant BD/48401/2008.

To *Clara* and *Agostinho*,

my parents.

Contents

1. Introduction and Motivation

Breast cancer is the most common cancer occurring in women in the Western world. In the UK in 2010 more than 49,500 women were diagnosed with breast cancer [1]. In the European Union (EU-27) more than 332,000 new cases of breast cancer were diagnosed in 2008 [1].

The use of ultrasound for breast evaluation has become popular for around three decades [2] with the introduction of important technological developments in ultrasound imaging systems [3], [4], [5], particularly in terms of beam-forming and signal processing [6], [7], as well as transducer piezoelectric crystal developments [8], [9]. To illustrate current state-of-art, in figure 1, the external components of the ultrasound imaging system used in our research – *Zonare z.one (Zonare Medical Systems, Inc., California, USA)* – are shown [10].

Conventional breast cancer screening typically consists of physical examination (palpation), followed by a mammogram (X-ray imaging) of the breast where any non palpable lumps may also be discovered. If the diagnosis still remains unclear, the assessment is followed by ultrasound (US) imaging or/and a core biopsy [11]. US imaging is, in fact, the preferred modality for image guided biopsy [12]. Thus, nowadays, ultrasound appears as the principal adjunctive imaging modality in breast cancer diagnosis.

An important advantage of ultrasound imaging over mammography is the fact that it uses non-ionizing radiation. Therefore, ultrasound is recognized as the modality of

choice in the evaluation of women who are symptomatic and younger than 30 years old, pregnant or lactating [13]. Furthermore, some studies have shown that in non-fatty breasts, ultrasound and magnetic resonance imaging (MRI) were more sensitive than mammography for invasive cancer [14].

In some instances, the patient may undergo a magnetic resonance imaging breast examination that entails injection of a vascular contrast enhancing material incorporating gadolinium, although it is impractical for use in general screening [15]. Note that, as a diagnostic test, MRI is much more expensive than mammography and ultrasound imaging [15].

Breast screening should incorporate safe and comfortable procedures using accurate (but inexpensive) equipment in order for women to feel encouraged to screen regularly and for the healthcare system to be able to afford it. Apart from being relatively inexpensive and safe, the ability of current ultrasound technology to generate images in real-time (video capabilities) with a small, portable machine has significantly contributed to its wide acceptance in clinical practice.

Another field where ultrasound imaging may play an important role is in the breast cancer therapy monitoring. Dynamic contrast-enhanced magnetic resonance imaging (DCE-MRI), which uses *gadopentetate dimeglumine* as the contrast agent [16] [17], and ^{18}*F-fludeoxyglucose* positron emission tomography (FDG-PET) [18] [19] have recently been developed to evaluate treatment response. Although, initial reported results are promising, frequent repetitive scanning would be problematic because of the toxicity of the contrast agents ([20]) and the costs of MRI and PET scanning. Thus, using ultrasound imaging, patients could be imaged as often as

desired by a radiologist without concerns in terms of side effects. Consequently, there is a strong incentive to develop additional ultrasound-based tools.

The use of contrast enhancement agents has also been investigated in ultrasonography [4], [21], [22]. In this case, microbubbles – small (typically about 3μm in diameter [23]) gas filled bubbles – are injected intravenously, which are several hundred times more reflective than soft tissues at diagnostic ultrasound frequencies [23]. Due to tumour angiogenesis (i.e. the development of new vascular networks essential for tumour growth [24]), the malignant masses become more echoic because of the presence of microbubbles in those tumour vessels [4] [25].

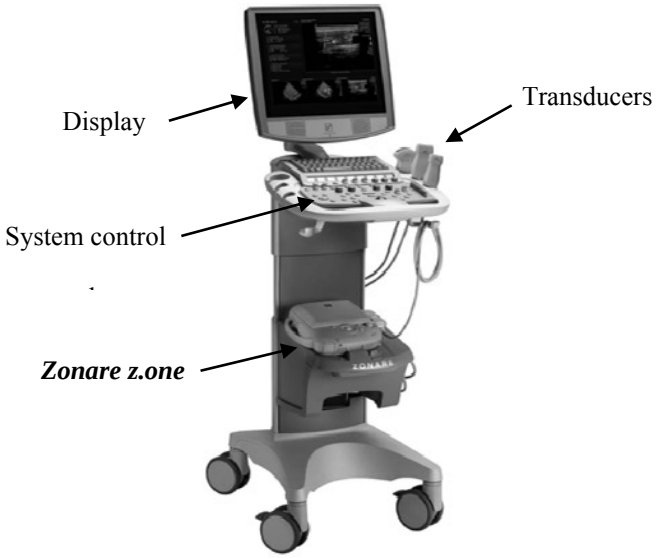

Figure 1 – External components of the ultrasound imaging system used in our research: *Zonare z.one*. The image display is mounted on a chassis with wheels for portability.

In this work we propose a new method of processing the backscattered ultrasound signals from breast tissue (based on the Fourier spectral analysis) to better estimate the degree of echogenicity and generate parametric images where the visibility of the breast mass boundaries is improved. Moreover, an algorithm is proposed to recover some anatomical structures (particularly, Cooper's ligaments) which are shadowed during the image acquisition process and, therefore, to improve the conspicuity of mass boundaries. Furthermore, this methodology has the advantage that it uses the I/Q data from a standard ultrasound equipment without the need for additional hardware.

We propose that that methodology can potentially aid radiologists in assessing the breast mass boundaries, providing additional diagnostic information to augment conventional B-mode images. The practical importance of this is that it may be possible to achieve a more accurate pre-operative sizing of those masses, avoiding either the removal of an over-estimated amount of tissue or a second surgical procedure to remove margins involved by tumour not removed in the primary operation.

Another strong motivation for the improvement of non-invasive diagnostic techniques is the potential to reduce the number of unnecessary biopsies.

1.1. Thesis Outline

Chapter 2 introduces the physics background of ultrasound imaging and relevant research on ultrasonic tissue characterization, especially focussing on work looking at the frequency domain. Chapters 3 and 4 present novel methods to generate the

Spectral Peak Value (SPV) parametric images and the *Local Weight of the Spectral Peak Value* (LWSPV) parametric images, respectively. Finally, in chapter 5 we summarise the key findings and present ideas for possible future work.

1.2. Summary of this Thesis' Research Contributions

This thesis makes two main contributions.

Firstly, the spectral peak value (SPV) was investigated in chapter 3. This spectral parameter was investigated to better estimate the degree of echogenicity for each pixel on the scan plane and to generate parametric images where the visibility of the breast mass boundaries is improved. This estimate was quantitatively compared with other estimates of the degree of echogenicity proposed in the literature. A 20-case pilot study was also conducted on clinical data to investigate if the SPV imaging provided supplementary diagnostic information to the B-mode imaging.

Secondly, an algorithm aimed at recovering some anatomical structures (particularly, Cooper's ligaments), which are shadowed during the ultrasound image acquisition process, was developed (cf. chapter 4). The information from both algorithms was then combined to generate a final SPV+LWSPV parametric image. A second 20-case pilot study was performed on clinical data that showed that the SPV+LWSPV imaging provided supplementary diagnostic information to the B-mode imaging in cases where the SPV imaging had not.

2. Background and Literature Critique

In this chapter we start by describing key concepts in biomedical ultrasonics. Next, we review relevant topics in the field of theoretical acoustics, signal processing and image formation as well as pertinent literature to this doctoral thesis.

2.1. Sound Propagation

Ultrasound is defined as an acoustic (pressure) wave with a frequency higher than the upper limit of the human hearing range (20 kHz).

It is often assumed that acoustic waves in soft tissues are like waves propagating in liquids [26]. In this case, ultrasound travels mostly as a longitudinal wave. When an acoustic wave propagates through a homogeneous liquid, it causes compressions and rarefactions across the propagation direction (say z), creating regions of over- and under-pressure respectively. As demonstrated in [26], that instantaneous pressure $p(z,t)$ is governed by the wave equation

$$\frac{\partial^2 p}{\partial z^2} = \frac{1}{c^2}\frac{\partial^2 p}{\partial t^2}$$

where the speed of sound c depends on both the density ρ and the bulk modulus B of the medium and is given by

$$c = \sqrt{\frac{B}{\rho}}$$

The bulk modulus B is a characteristic of each substance [27] and is defined by [†]

$$B = -V\frac{\partial p}{\partial V}$$

where V denotes the volume of liquid.

In words, B measures the degree of compressibility of a substance: the greater the bulk modulus value, the greater the pressure required to produce the same volume change. The compressibility κ of a substance is the inverse of the bulk modulus, i.e.

$$\kappa = \frac{1}{B}$$

The mean speed of sound in human soft tissue is normally assumed to be around 1540 m/s [28].

Another concept that characterizes a medium is its characteristic acoustic impedance Z, which is defined as the product of its density and the speed of sound, i.e.

$$Z = c\rho\,.$$

2.2. Scattering and Ultrasound Imaging

Tissue is, by its very nature, inhomogeneous and when acoustic waves travel through it, structures of different size and with irregular boundaries scatter waves in several directions and consequently cause (constructive or destructive) interference between neighbouring waves. In general, there are three categories of scattering: *specular scattering* from objects much bigger than the wavelength; *diffusive scattering* from objects much smaller than the wavelength; and *diffractive scattering*

[†] It holds only for purely elastic media (Hooke's law).

from objects in between the extremes described above, which is the largest category [28] (for further details on *diffractive scattering* see section 2.4).

Part of the scattered sound reaches the transducer (backscattered echo) where, after its translation into electric signals, the echo information received by each element of the transducer is aligned and summed to form the RF (radio-frequency) signal of each scan line (beamforming) [29].

To build up a conventional B-mode image (B stands for brightness), the envelope of each RF signal is detected and followed by a logarithmic compression in order to reduce the dynamic range of the amplitude values (see figure 2).

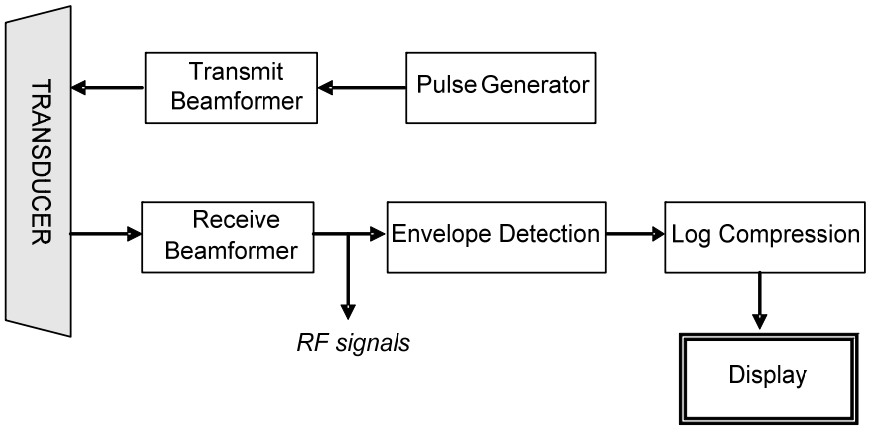

Figure 2 – Simplified Conventional Ultrasound System Block Diagram.

An important parameter that affects the quality of the final image is the frequency of the insonifying ultrasound signal. In practice, part of the signal energy is absorbed by tissue, resulting in attenuation of the signal. The higher the frequency, the greater the absorption (cf. section 2.3). Therefore, lower frequency probes can image deeper

tissues, but give rise to images with a lower spatial resolution and consequently small objects may not be as clear in them.

2.3. Attenuation in the Frequency Domain

When acoustic waves propagate in tissue, losses of energy are involved, which causes the attenuation of them. Absorption of wave energy results in its degradation to heat. Although other factors (especially scattering) contribute to the total loss of sound energy in tissue (see reference [26] for a detailed discussion), in this section we will consider attenuation as mainly caused by absorption and consider scattering later.

Attenuation in tissue can be described by an exponential law with depth [28], [26]. For a single-frequency (f_c) plane wave of amplitude P_0 travelling in the positive z-direction, the acoustic pressure, $p(z,t)$, can be written as

$$p(z,t) = P_0 e^{j(2\pi f_c t - kz)}$$

Then, the acoustic pressure considering absorption, $p_a(z,t)$, can be written as

$$p_a(z,t) = e^{-\bar{\alpha}z} p(z,t)$$

where $\bar{\alpha}$ is the attenuation coefficient and is often expressed in terms of cm^{-1}.

Experimental data indicate that the attenuation coefficient has a power law dependence on frequency [26] and can be defined as

$$\bar{\alpha}(f) = \alpha f^{y}$$

in which the values of α and y depend on the type of tissue (see below).

Let us now consider a certain fractional region on the scan plane at a distance Z (cm) from the transducer and that the average attenuation coefficient of the intervening tissues is $\bar{\alpha}$. In the frequency domain, considering the effects of absorption, the measured spectrum is equal to

$$\mathrm{V_a(f)} = \mathrm{e}^{-\alpha \mathrm{f}^{y} \cdot 2\mathrm{Z}} \cdot \mathrm{V(f)} \qquad \text{(eq. 1)}$$

where the factor 2 accounts for beam round-trip and V(f) is the spectrum assuming an attenuation-free medium. In decibels, the spectrum is given by

$$20\log(V_a(f)) = 20\log\big(V(f)\big) - 20\log\left(e^{\alpha f^{y} \cdot 2Z}\right)$$

$$\Leftrightarrow V_{a_{dB}}(f) = V_{dB}(f) - 8.686\alpha f^{y} \cdot 2Z$$

$$\Leftrightarrow V_{a_{dB}}(f) = V_{dB}(f) - \alpha_{dB} f^{y} \cdot 2Z$$

where α_{dB} is usually expressed in terms of $\mathrm{dB/(MHz^{y}cm)}$.

In [26], a compilation of attenuation coefficients of various tissues and biologically relevant liquids as a function of frequency is presented. According to [30], in the case of normal breast tissue, the values of α_{dB} and y are 0.75 ± 0.3 $\mathrm{dB/(MHz^{y}cm)}$ and 1.5 (for 0.5–6 MHz at 37ºC), respectively.

Interestingly, considering the case that $V(f)$ takes a Gaussian shape, equation 1 suggests a progressive downshift in the peak frequency (i.e., centre-frequency) of $V(f)$ as depth increases. In practice, we can estimate the centre-frequency downshift of the received echo as follows (cf. [10])

$$f_{c_{echo}} = f_c - \Delta_{f_c} \cdot 2Z$$

where the rate of frequency change with depth Δ_{f_c} (in Hz/mm) is dependent on the medium properties and is *a priori* experimentally determined.

2.3.1. Time Gain Compensation and *Z.one* Ultrasound Machine

In order to compensate for effects of absorption, most commercial ultrasound systems have a method known as *time gain compensation* (TGC). The scan plane is divided into horizontal (or radial) strips, each of which is associated with a different variable-gain amplifier. Those gains are often manually adjusted by the operator. In the case of the ultrasound machine used in our research – *Zonare z.one (Zonare Medical Systems, Inc., California, USA)* – the received signal amplification is variable with depth and controlled by TGC curves which have been pre-computed for various imaging modes and stored on a database [10]. It also compensates for the attenuation-induced centre-frequency downshift using the method previously described where the values of Δ_{f_c} are pre-stored on a database.

2.4. Scattering and Scatterer Characterization

Some researchers have proposed models based upon physical principles to predict the behaviour of acoustic waves inside tissue and to characterize tissue scatterers: [31], [32], [33] and more recently [34], [35]. Here we review some theoretical results that underpin those ideas and relate the backscattered power to scatterer properties, such as size. For a more detailed discussion on the ultrasonic propagation properties

of biological tissue, from tissue sections all the way down to cellular scale, see [36] and [37].

As several phenomena that affect wave propagation are complex and not fully understood, the existing models rely on several simplistic assumptions to make the problem tractable. Typically, those models are based on the single-scattering approximation, also known as the Born approximation [31]. In this approximation, the incident wave is essentially unchanged as it propagates through the scattering medium and the scatterers (particles) are assumed to interact with the incident wave only once, i.e. multiple scatterings are assumed to be negligible [31], [38].

In terms of spectrum, it is convenient to work with scattered power (W_s). When a wave of intensity I_i (power per unit area) is incident on a scatterer, W_s is related to I_i by

$$W_s = \sigma_{ts} I_i$$

where σ_{ts} is the *total scattering cross-section*, which has units of area.

Let us consider a plane wave of frequency f incident on a small volume where there is a spherical scatterer of radius a (the value of a is such that the scattering is diffractive), with acoustic impedance ($\sqrt{\rho_s/\kappa_s}$) slightly different from its surroundings. The fractional variation in medium compressibility γ_κ and density γ_ρ can be defined as

$$\gamma_\kappa = \frac{\kappa_s - \kappa_0}{\kappa_0} \quad ; \quad \gamma_\rho = \frac{\rho_s - \rho_0}{\rho_s}$$

where κ_0 and ρ_0 are the average values of compressibility and density respectively for the surrounding medium.

For a spherical scatterer, the fraction of power of the incident plane wave that is scattered per unit solid angle, $\sigma_{ds}(\theta)$, can be estimated as follows (see figure 3). It is usually termed the *differential scattering cross-section* [33], [39].

$$\sigma_{ds}(\theta) = \left[\frac{k^2}{k_s^3}(\gamma_\kappa + \gamma_\rho \cos\theta)(\sin k_s a - k_s a \cdot \cos k_s a)\right]^2 \qquad \text{(eq. 2)}$$

where $k_s = 2k\sin(\theta/2)$ and k is the wavenumber ($k = 2\pi f/c$).

If θ equals 180º, i.e. in the opposite direction of the incident wave and towards the transducer, equation 2 reduces to

$$\sigma_{bs} = \sigma_{ds}(180^o) = \left[\frac{1}{8k}(\gamma_\kappa - \gamma_\rho)(\sin 2ka - 2ka \cdot \cos 2ka)\right]^2 \qquad \text{(eq. 3)}$$

which is usually termed the *backscattering cross-section*.

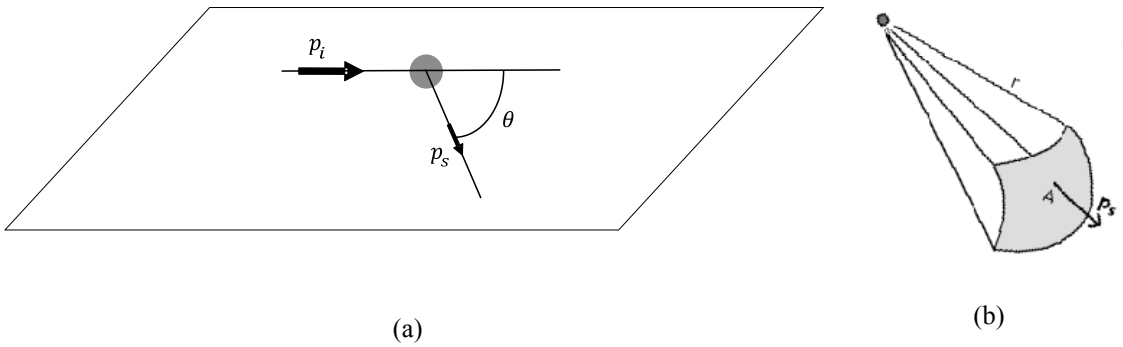

(a) (b)

Figure 3 – (a) scattering geometry on the scan plane: incident pressure (p_i) and scattered pressure (p_s) for a certain angle θ. (b) 3D view of the scattered wavefront (spherical wave); solid angle $\Omega = A/r^2$ (steradians).

As illustrated in figure 4, the amount of scattered power can vary significantly with angle and *ka* number (wavenumber × scatterer radius). It is worth noting the frequency dependence of backscattered power. For the same physical object, changing the wavelength (equivalent to change the frequency inside the same medium), changes the fraction of backscattered power considerably (see figure 4).

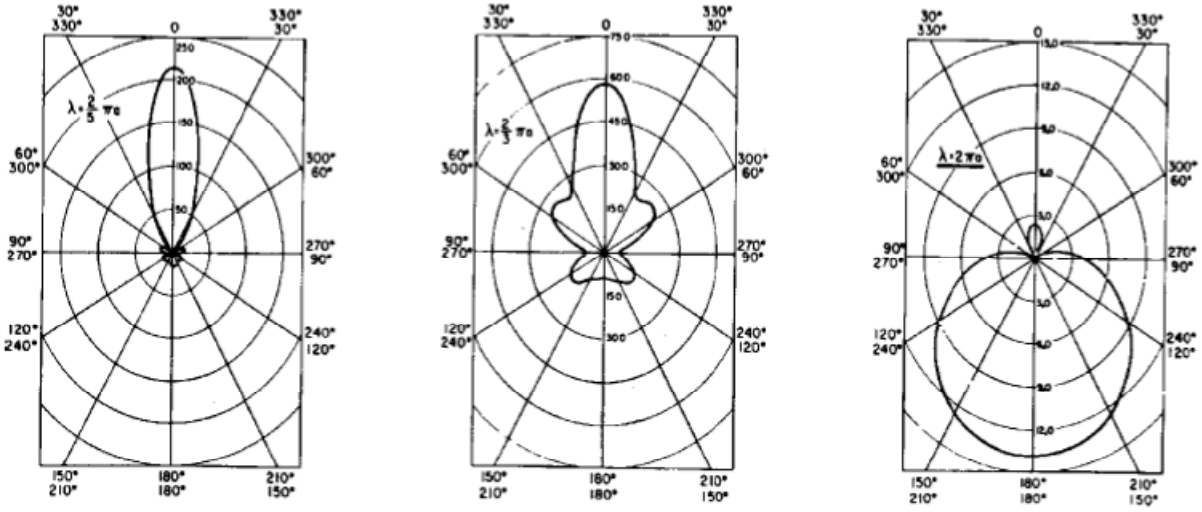

Figure 4 – Polar scattering diagrams for a rigid sphere for different values of *ka*. They show the scattered intensity versus angle θ, where the incident acoustic wave is a plane wave of unit amplitude. Note that 0º is the incident direction and 180º is the backscattering direction. (These diagrams were taken from [40].)

When an acoustic wave traverses an ensemble of particles, the waves scattered by each one will interfere and the overall scattering will depend on the configuration of the set of scatterers. Some researchers have suggested that biological tissues can be considered as stochastic tissues made up of several randomly positioned discrete scatterers per unit volume [41]. They have also observed that it has proved useful to

interpret experimental results in terms of a spatial distribution of effective, discrete scatterers [41].

If we assume a fractional region which contains discrete scatterers and further assume that the interference between scattered waves causes no loss of energy, then the total backscattered energy flux (power) equals the sum of individual backscattered energy fluxes. In this case, the overall *backscattering cross-section* is the sum of individual *backscattering cross-sections*.

It is also common to define a *differential scattering coefficient* μ_{ds} as a measure of the overall *differential scattering cross-section* per unit volume [28]. In a similar way, a *backscattering coefficient* μ_{bs} can be defined as the overall *backscattering cross-section* per unit volume.

2.5. Fourier Transform and Practical Considerations

Let $v(t)$ denote a signal expressed as some function of time. By definition, the Fourier Transform (FT) of $v(t)$ is given by the integral

$$V(f) = \int_{-\infty}^{\infty} v(t) e^{-j2\pi f t} dt$$

Given the Fourier Transform $V(f)$, the original signal $v(t)$ is exactly recovered using the Inverse Fourier Transform:

$$v(t) = \int_{-\infty}^{\infty} V(f) e^{j2\pi f t} df$$

In practice, the RF signal collected from an ultrasound system is a finite-length digitized signal, sampled at frequency f_s. To obtain the spectrum of the RF signal or segments of it, $v[n]$, we can use the Discrete Fourier Transform (DFT) [42], an adaptation of the FT principle to discrete signals, which is given by the finite summation

$$V[m] = \sum_{n=0}^{N-1} v[n]\, \mathrm{e}^{-\mathrm{j}2\pi\left(\frac{\mathrm{mn}}{\mathrm{N}}\right)}, \qquad m = 0, 1, \ldots, N-1$$

where N is the number of samples.

In our work, to calculate the DFT we employed the Fast Fourier Transform (FFT) algorithm available in *Matlab*® (*version 7.9.0.529*) [43].

2.5.1. The Effect of Windowing on Spectral Analysis

The choice of the window function is an important aspect when computing the spectrum of a certain segment of the signal, i.e. when we are only interested in "viewing" what is happening within that interval in the frequency domain.

Ideally, the discrete Fourier transform of a window function should have a main lobe (centred at zero Hz) as narrow as possible and the maximum side lobe level should be as low as possible in relation to the main lobe. However, both requirements cannot be optimized simultaneously [44] [42] and, thus, there is a trade-off between the main lobe width and the relative side lobe attenuation when we are choosing the window function. Some commonly used window functions are defined in [42], namely *rectangular*, *Hamming*, *Hanning* (or *hann*) and *Blackman* windows.

Two effects are related to the window properties: *resolution* and *leakage*. In signal processing, *resolution* refers to the ability to resolve closely spaced spectral features. On the other hand, *leakage* is present when the component at one frequency leaks into the vicinity of another component due to the spectral smearing introduced by the window [42], [45]. The *resolution* is influenced primarily by the *main lobe width* (width of the main lobe at 3dB below the main lobe peak) whereas the degree of *leakage* depends on the *relative side lobe attenuation* (difference in height from the main lobe peak to the highest side lobe peak) [42], [45].

2.5.2. Zero-padding

In order to assess spectral features with more accuracy, zero-padding may be applied to the windowed sequence, $v[n]w[n]$, which is extended by padding it with zeros to obtain a longer sequence before computing the FFT. As a result, the frequency-domain sampling spacing is decreased and a less coarse spectrum is obtained.

2.6. Frequency Domain Backscattering Simulator

Let us consider a sinusoidal acoustic wave modulated by a Gaussian-pulse with standard deviation σ. In the frequency domain, its spectrum is also a Gaussian curve centred around the sinusoid frequency and with standard deviation

$$\sigma_f = \frac{1}{2\pi\sigma}$$

In fact, the Fourier transform of a Gaussian curve is as follows [46],

$$v(t) = e^{\frac{-t^2}{2\sigma^2}} \quad \overset{FT}{\leftrightarrow} \quad V(f) = \sqrt{2\pi\sigma}e^{-2\pi^2 f^2 \sigma^2}$$

Note that the right-hand side expression can be rewritten as

$$V(f) = \sqrt{2\pi\sigma}e^{\left[\frac{-f^2}{2\left(\frac{1}{2\pi\sigma}\right)^2}\right]}$$

Next, consider that the acoustic wave is diffractively scattered by tiny structures. As discussed above, for a scatterer of a certain size, some frequency components are backscattered with lower magnitudes, i.e. some frequencies are more attenuated than others. Recalling equation 3 (cf. section 2.4), in the backscattered signal, frequencies are more attenuated when the value of σ_{bs} approaches zero, or equivalently, when $\sin 2ka - 2ka\cos 2ka$ approaches zero.

The first six numerically-calculated positive roots of this equation and the corresponding values of *a* for some specific frequencies are shown in Table 1.

In order to explore the frequency dependence of the backscattering coefficient, a *Frequency Domain Backscattering Simulator* (*FDBSimulator*) was developed based on equation 3 (cf. section 2.4).

Considering a sinusoidal acoustic wave modulated by a Gaussian-pulse with f_c = 6.3 MHz (and $\sigma_f = 10^6$) propagating through a medium and interacting with four separable spherical scatterers of different radii (namely, 60 µm, 70 µm, 80 µm and 90 µm). The backscattered spectra obtained theoretically using the *FDBSimulator* (not considering attenuation along the propagation in the intervening medium) are plotted in figure 5 and for f_c = 8.3 MHz in figure 6. It is noticeable that there is a change in spectral shape with an alteration in the scatterer radius *a* or in the centre-frequency f_c.

For instance, when the backscattered coefficient at f_c (given a certain a) is close to zero, it gives rise to an M-shaped spectrum around f_c. On the other hand, if that coefficient is close to a peak, a predominantly bell-shaped spectrum is observed. The different spectral shapes of the received echoes are influenced by the undulation of the backscattered coefficient value as a function of both the scatterer radius and the emitted wave centre-frequency (red line in those figures).

	5.70	6.30	8.30	f (MHz)
	270.2	244.4	186.0	λ (μm)
roots (ka)		a (μm)		
2.2467	96.608	87.407	66.345	
3.8626	166.09	150.27	114.06	
5.4521	234.44	212.11	161.00	
7.0331	302.42	273.62	207.69	
8.6104	370.25	334.98	254.26	
10.1857	437.98	396.27	300.78	

Table 1 – First six roots (ka) of the backscattering coefficient of a spherical scatterer and the corresponding values of the effective radius a in the case of 5.7 MHz, 6.3 MHz and 8.3 MHz (assuming c = 1540 m/s).

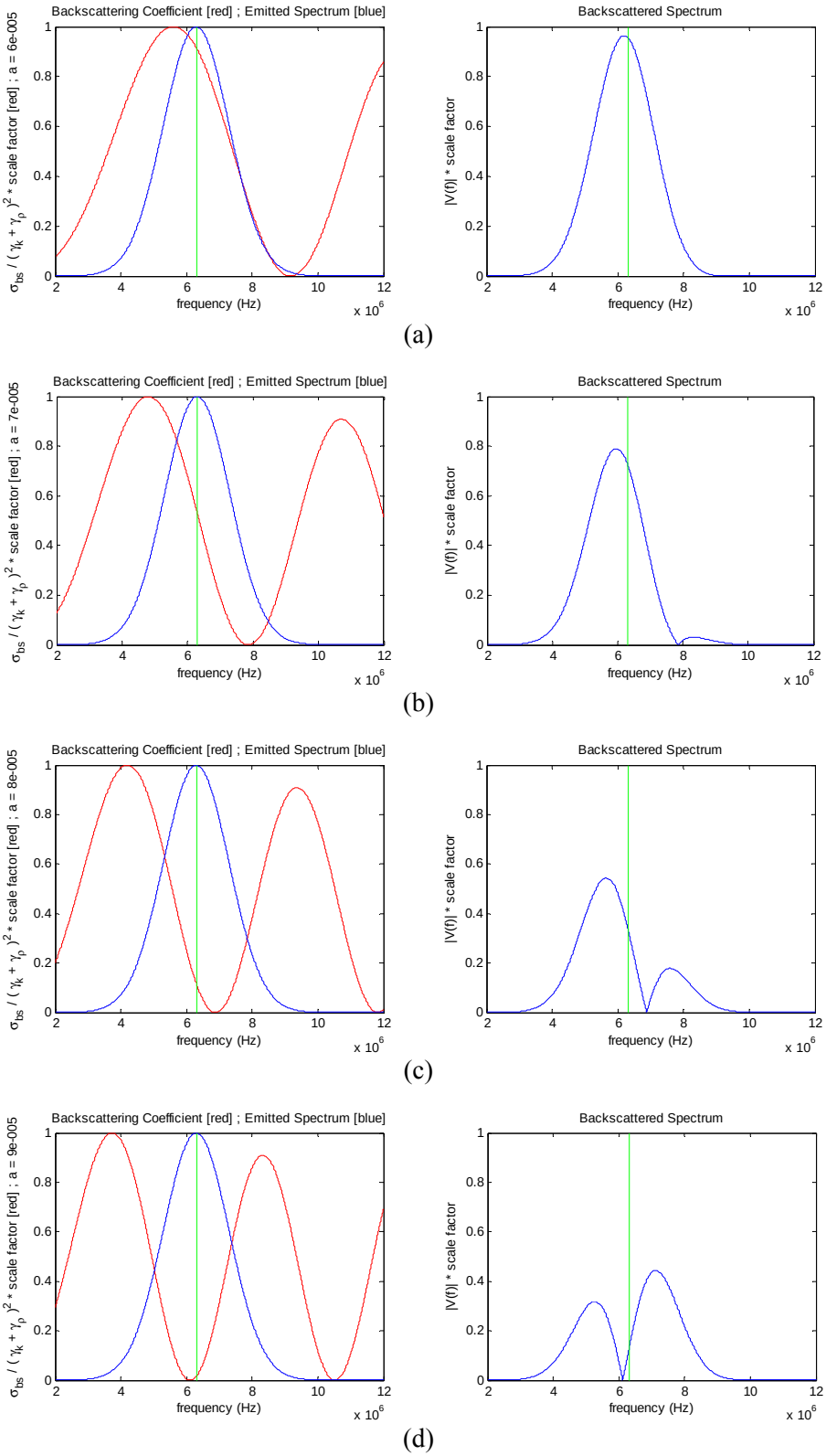

Figure 5 – *FDBSimulator* results, using a centre-frequency f_c = 6.3 MHz, for four spherical scatterers of different radii: 60 µm (a), 70 µm (b), 80 µm (c) and 90 µm (d). We assumed c = 1540 m/s and $\sigma_f = 10^6$.

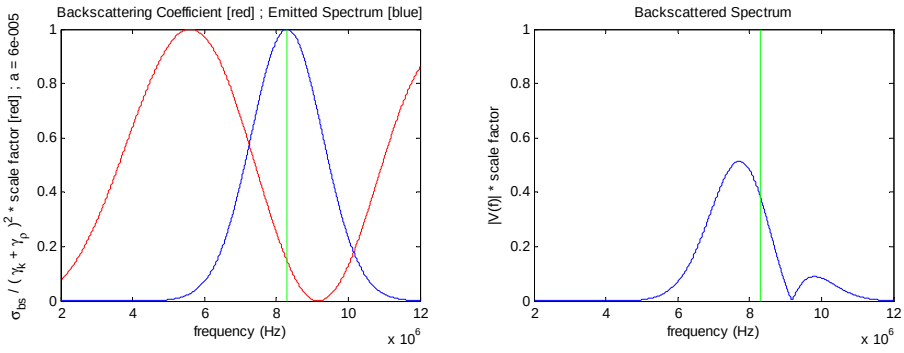

(a)

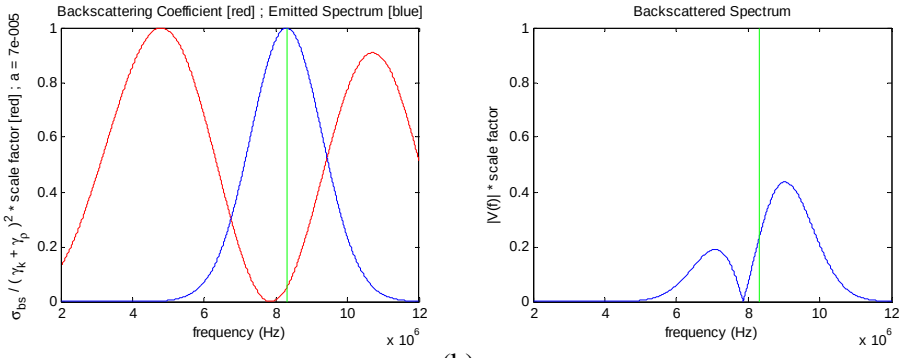

(b)

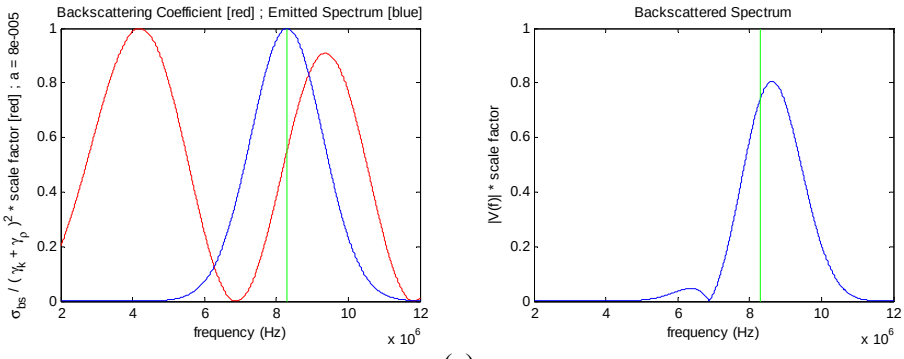

(c)

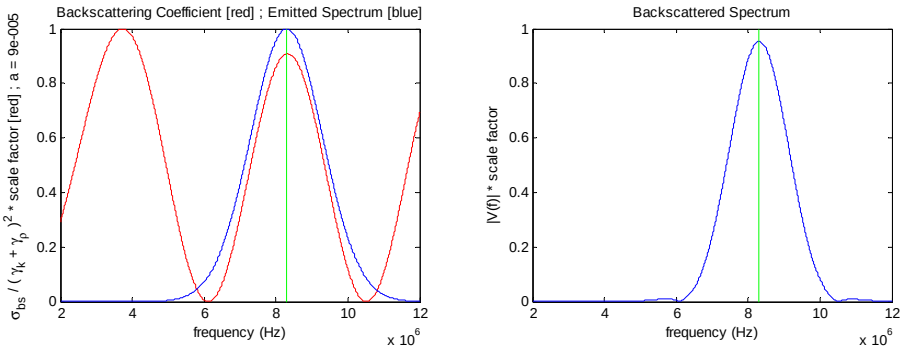

(d)

Figure 6 – *FDBSimulator* results, using a centre-frequency f_c = 8.3 MHz, for four spherical scatterers of different radii: 60 μm (a), 70 μm (b), 80 μm (c) and 90 μm (d). We assumed c = 1540 m/s and $\sigma_f = 10^6$.

2.7. Ultrasonic Tissue Characterization

The research field of ultrasonic tissue characterization (UTC) – also termed by some authors as quantitative ultrasound (QUS) imaging [47] – deals with the development of methods which use tissue-related information from the ultrasound backscattered echoes to estimate tissue properties and generate parametric images.

In order to place the diverse UTC approaches in perspective, we categorize UTC methodologies as summarised in figure 7 (which also serves as a summary to the remaining contents of this chapter). To contextualize the methodology proposed in this thesis (SPV+LWSPV imaging), it has been included in the diagram (dashed line) under the corresponding category.

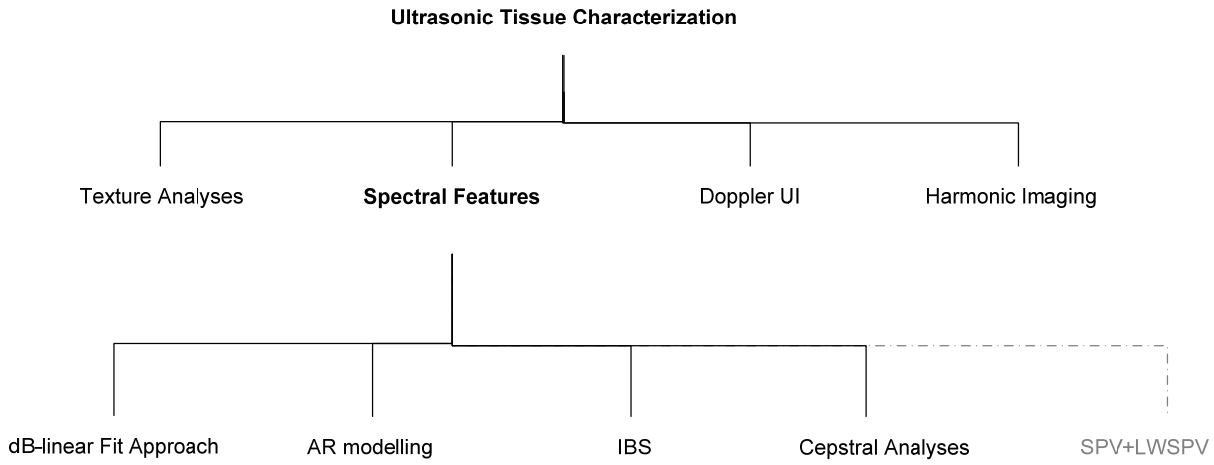

Figure 7 – Diagram of ultrasonic tissue characterization approaches.

In [48], Lizzi et al. first proposed an approach for measuring spectral features from the backscattered echoes, considering that the spectrum exhibits (in dB) a quasi-linear shape. The aim was to utilise spectral parameters to differentiate among different types of tissue. Let us analyse this methodology in detail, which entails three main steps: spectrum computation and calibration, dB-linearization of the spectrum and spectral parameters extraction.

For a selected region of interest (*ROI*) with length *L* (number of pixels along the axial direction) and width *W* (number of adjacent scan lines), the squared spectral magnitude $|V(f)|^2_{ROI}$, also called the power spectrum, can be computed by averaging the squared spectral magnitudes for each line $|V(f)|^2_{line}$ calculated over the RF signal segment of length *L* ([48])

$$|V(f)|^2_{ROI} = \frac{1}{W} \sum_{line=1}^{W} |V(f)|^2_{line}$$

Then, the calibrated spectrum is calculated by dividing the estimated spectrum by the spectrum obtained from an acoustic mirror located in the transducer focal zone inside a water tank ([48], [49]). This is to reduce the spectral shaping introduced by the electro-acoustic properties of the transducer and diffraction effects during transmission and reception, i.e. to reduce ultrasound-system-dependent artefacts. In theory, the reference acoustic mirror should be placed at the same distance from the transducer as the sample volume. A calibration spectrum and a typical power spectrum (in dB) for a region of prostate obtained in [50] is shown in figure 8(a). Next, a linear regression over *"the frequency range that exhibits an adequate signal-to-noise ratio (SNR)"* [50], [51] was computed (see figure 8(b)). That frequency

range is a band of spectral points above a certain threshold related to the value at the centre frequency.

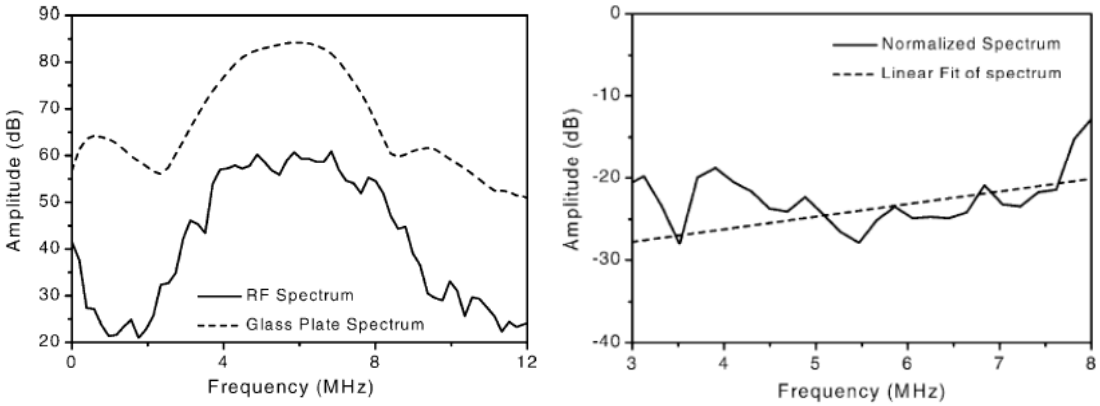

(a) (b)

Figure 8 – RF spectrum (a), calibration spectrum (a) and calibrated power spectrum (b) for a region of prostate obtained in [50], using a7 MHz transducer. (these pictures were taken from [41])

Three parameters extracted from the linear fit of spectrum were then used for tissue characterization: *spectral slope (dB/MHz)*; *midband fit (dB)*, i.e. the value of the regression line at the centre frequency; and *spectral intercept (dB)*, the extrapolation of the regression line to zero frequency (i.e. its intercept at zero frequency) [51] [52], which were utilized to generate parametric images using a colour-coded representation. Fundamentally, that set of quantitative descriptors summarizes the key features of the calibrated power spectrum (in dB) considering that it exhibits a quasi-linear shape (over the previously defined frequency range). However, in our view, it is possible that useful information to estimate tissue properties might be lost during the linearization of spectrum, since it wipes out spectral peaks and notches (see figure 8).

Some relations between those spectral parameters and the underlying scatterer structures of the tissue are discussed in [53], [54] and [55]. They conclude that the *spectral slope* is a function of the average effective radius of scatterers and that the *spectral intercept* is a function of the average effective radius of scatterers and the average acoustic concentration of scatteres.

For instance, in [50], [56] and [57], the incorporation of the *spectral slope*, the *midband fit* and the *spectral intercept* into a multi-feature approach is reported to better assist radiologists in the detection of malignant areas. In [58] [59], those three spectral parameters were also employed in breast tissue differentiation. In that work, they estimate the echogenicity of a region as the average of the *spectral intercept* values for the pixels within that region. Heterogeneity is estimated as the standard deviation of the *midband fit* values. They also use the difference between the mean *midband fit* values within the mass region and the posterior regions as an estimate of shadowing. Those spectral descriptors were used together with morphological descriptors of tumour shapes, to differentiate benign and malignant tumours. Although they report good results, it is not clear how much the spectral parameters alone contribute to those results. As noted in [58] [59], the use of those three spectral parameters alone (*spectral slope*, *midband fit* and *spectral intercept*) was not enough to differentiate among different types of breast mass.

In [60] a performance comparison is presented between spectral parameters (in particular, *spectral slope*, *spectral intercept* and total area under the non-linearized dB spectrum) and texture parameters from the gray-level co-occurrence matrix (GLCM), which measures spatial intensity dependence. The results indicate an

improvement in differentiation of breast malignant regions based on spectral parameters over texture-based features [60]. The co-occurrence matrix had already been investigated for breast tissue classification, for example, in [61], [62] and [63], where it was concluded that *contrast* and *correlation* computed from GLCMs were the best texture descriptors to distinguish between breast lesions [63].

Spectral features have also been used to monitor tumour cell death during therapy [64], [65]. In [64], two parameters were investigated: *spectral slope* and *midband fit*. To do so, the *RF* data was collected from cell pallets exposed to chemotherapeutics that induce apoptosis (programmed cell death, *cf.* [66]). To increase spatial resolution, high-frequency transducers were used (30 and 35 MHz), which, however, have limited penetration *in vivo* due to attenuation. During the experiment, an increase in the *spectral slope* over time was observed [64] but, as for the *midband fit*, a clear pattern was not identified.

Another often used spectral parameter is the integrated backscatter (IBS) coefficient [67], which can be estimated from the (discrete) squared spectral magnitude, $|V[m]|^2$, over the bandwidth, BW, as follows. The IBS provides an estimate of the backscattered power over the bandwidth [68].

$$IBS = \sum_{BW} |V[m]|^2$$

In [69] and [70], it is reported that apoptotic cells exhibited an increase in the integrated backscatter coefficient (transducer centre frequency of 20MHz [69] and 40MHz [70]; both in vitro experiments).

In the proprietary *HistoScanning* methodology [71] [72], instead of a Fourier spectral analysis, a wavelet analysis is performed. The output coefficients of the bi-orthogonal filters available on *Matlab* are used to differentiate between three types of tissue: 'healthy', 'benign', 'malignant' [71]. To refine the results, that information is combined with an estimate of the backscattered energy (similar to the previous IBS coefficient) and measurements of local contrast [71]. Very preliminary results for breast cancer using a small sample (including 6 malignant cases) are reported in [73].

Another technique some researchers have investigated in the frequency domain is cepstral analysis. They have applied this technique to the backscattered echoes to estimate some properties of the underlying scatterer structures of the tissue. First, the magnitude component of the spectrum is log-compressed, $log|V(f)|$ (this step reduces the dynamic range of the amplitude values, making small values more prominent). Next, the crucial observation leading to the cepstral analysis is that the log-compressed spectrum can be treated as a waveform and subject to further Fourier analysis [74]. Thus, the final step is to compute either the *Fourier Transform* of $log|V(f)|^2$, [75], or the *Inverse Fourier Transform* of $log|V(f)|$, [76], [77]. In doing so, we can analyse periodicity properties of $log|V(f)|$ and the components at low *quefrencies*[‡] to characterize the "amplitude modulation" of $log|V(f)|$. In [75], [76] and [78], the incorporation of a cepstral parameter to tissue characterization is discussed. Assuming that the ultrasound signal is backscattered from quasi-regularly distributed scatterers in biological tissues, the *quefrency* corresponding to the maximum cepstral value, $\boldsymbol{q}_{max}$, is used to estimate the *mean scatterer spacing*

[‡] The name of the independent variable of the cepstrum is known as quefrency.

(*MSS*). The lower the $\boldsymbol{q}_{max}$, the lower the *MSS* [75], [76]. Observations from breast tissue *in vivo* experiments concluded that malignant regions exhibited lower *mean scatterer spacing* than normal tissue [76]. The use of cepstral features together with texture features is also discussed in [79].

Lastly, it is pertinent to discuss another way of estimating the spectrum which has been often proposed by some researchers – the use of autoregressive modelling for spectral estimation [80], [81], [82]. In the particular case of breast tissue, the autoregressive (AR) model [75], [76], [83] and the autoregressive moving average (ARMA) model [84] have been investigated. The main challenge with this methodology is the finding of an accurate order for the data under analyses.

The autoregressive approach entails three main steps: first, selection of the type and size (order) of model; second, estimation of the model parameters based on the available data; third, computation of the spectrum from those parameters. The most general linear model is termed an autoregressive moving average (ARMA) model of order *(p, q)*, and its output sequence, $x[n]$, is defined as [81] [85].

$$x[n] = -\sum_{k=1}^{p} a[k]x[n-k] + \sum_{k=0}^{q} b[k]\eta[n-k]$$

where $a[k]$ and $b[k]$ are the ARMA parameters and $\eta[n]$ is an input driving sequence (for instance noise). If all $\mathrm{b}[k]$ terms are zero, except $\mathrm{b}[0] = 1$, we have the AR model of order p [81]. When all $\mathrm{a}[k]$ terms are zero, it is termed a moving average (MA) model of order q [81]. This methodology uses a different approach to spectral estimation: instead of trying to estimate the spectrum directly from the data, it models the data as the output of a linear system (driven by white noise) and then

attempts to estimate the parameters of that linear system. One of the promising aspects of the modelling approach to spectral estimation is that if an accurate model for the data under analyses is found, better resolution can be obtain compared to FFT based models in cases when the signal length is short [80], [81], [86] but, in UTC, finding an accurate model has been the problem.

2.7.1. Harmonic Imaging

In this ultrasound imaging modality the focus of analysis is not around the centre frequency (also known as the fundamental frequency) but around the harmonic frequencies [87], [88], [89].

The formation of harmonics stems from the nonlinear propagation of the acoustic waves – see figure 9. During propagation through tissue, different points of the ultrasound pulse travel at slightly different sound speeds – the high pressure components of the acoustic wave travel faster – causing distortions on the ultrasound pulse that give rise to harmonic frequencies [28], [90]. The information in the harmonic bands, usually the information in the second harmonic band [28], is then used to generate the image.

In comparison with conventional B-mode imaging, some improvements in breast ultrasound imaging have been reported: greater contrast, less clutter and phase aberration and fewer reverberation artifacts [91], [92]. Although harmonic imaging could provide important breast tissue information in clinical practice, this area has been only partially explored [90].

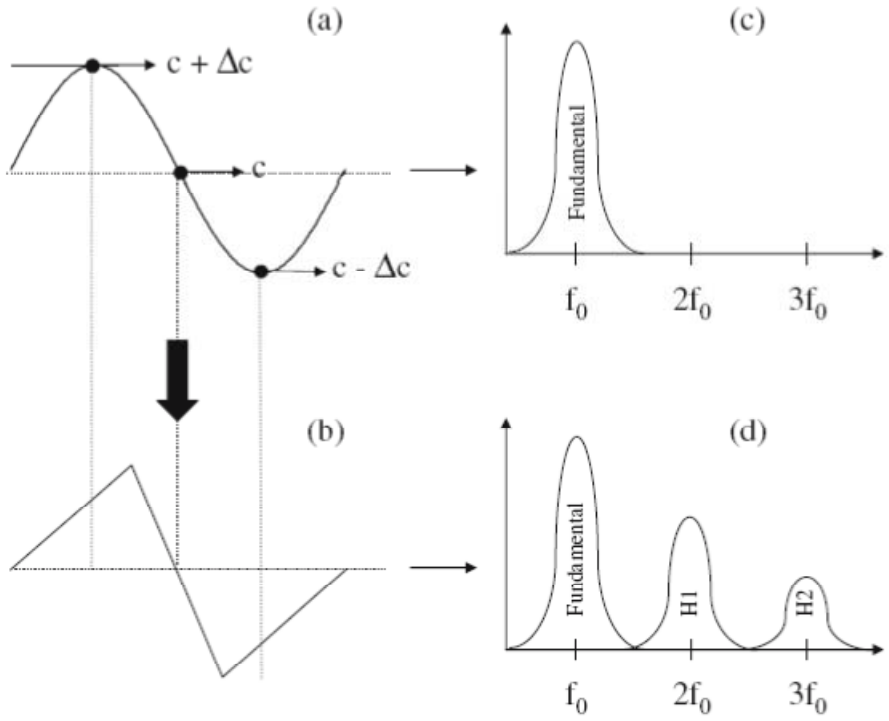

Figure 9 – (a) emitted ultrasound pulse; (b) distorted pulse – during propagation through the tissue, different points of the ultrasound pulse travel at slightly different sound speeds, causing distortions on the ultrasound pulse that give rise to harmonic frequencies; (c) the spectrum of the emitted ultrasound pulse; (d) the spectrum of the distorted pulse, where *H1* and *H2* represents the second and third harmonic band, respectively. This figure was taken from [90].

2.7.2. Doppler Ultrasound Imaging

This ultrasound imaging modality has proved particularly useful in detecting blood vessels. The basic principle behind this imaging modality is described next. The Doppler effect is the perceived change in frequency as a sound source moves towards or away from the receiver [28]. Let us consider the simplified situation of a transducer sensing the flow of blood in a vessel flowing with velocity v_b at an angle

θ to the vessel, as depicted in figure 10. The Doppler shift frequency, Δ_f, can be given by the following equation (cf. [28] for further details).

$$\Delta_f = f_D - f_0 = \left[2\left(\frac{v_b}{c_0}\right)\cos\theta\right] f_0$$

where f_0 is the transmitted frequency, f_D is the received frequency, or Doppler frequency, and c_0 is the speed of sound in the intervening medium.

This acoustic phenomenon is then used to generate ultrasound parametric images where color-coded pixels are superimposed to the B-mode image in the regions where blood flow is detected. Figure 11 shows an example clinical image. See [93] and [28] for a detailed discussion.

In terms of breast cancer, Doppler ultrasound imaging can be used to identify regions on the scan plane with high vascularity (area covered by blood vessels per unit area) [94], [95], [96]. However, as pointed out in [97], [98] and [99], the simple assumption that higher vascularity indicates higher probability of malignancy results in a weak diagnostic performance (i.e. using the vascularity parameter alone is not enough to differentiate between tumour/non-tumour regions).

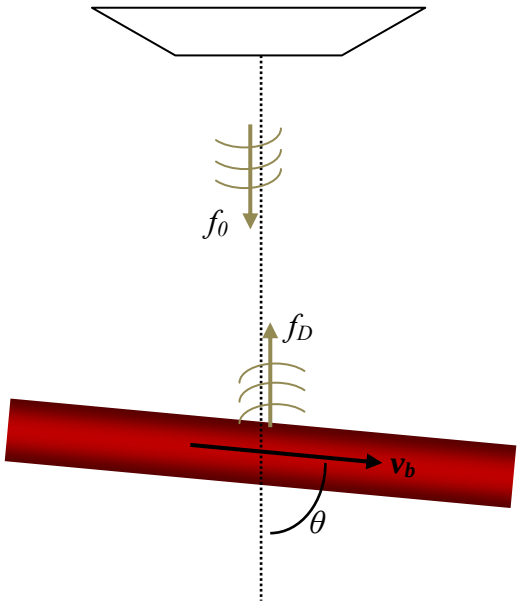

Figure 10 – Ultrasonic wave intercepting blood moving at velocity v_b in a vessel tilted at angle θ; f_0 is the transmitted frequency and f_D is the received frequency, or Doppler frequency.

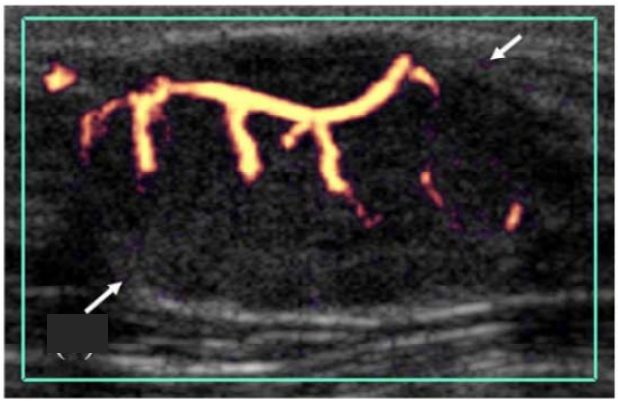

Figure 11 – Tumour vessels imaged by Doppler ultrasound. The malignant mass is between the arrows. This figure was taken from [90].

2.8. Final Considerations

In this chapter, we have discussed relevant methodologies proposed in the literature to characterize soft-tissue based on the acoustic properties of the backscattered ultrasound signals. In particular, we noted that spectral (or frequency-domain) techniques afford a convenient means of analysing the spectral content of the backscattered echoes and hence extracting frequency-dependent acoustic information not available on conventional B-mode images.

In the next chapter we propose a new methodology where the spectral information is employed to better estimate the degree of echogenicity and generate parametric images where the visibility of breast mass boundaries is improved. This methodology can potentially aid radiologists in assessing the mass boundaries, providing additional diagnostic information to augment conventional B-mode images. The practical importance of this is that it may be possible to achieve a more accurate pre-operative sizing of those masses, avoiding either the removal of an over-estimated amount of tissue or a second surgical procedure to remove margins involved by tumour not removed in the primary operation.

3. SPV Parametric Images

In this chapter, we explore the use of the spectral information in a novel way, where the spectral peak values (*SPV*) are used to estimate the degree of echogenicity. This information is then employed to generate a parametric image where the visibility of breast mass boundaries is improved relative to a B-mode image. A high-level diagram of the algorithm for generating a SPV parametric image is depicted in figure 12.

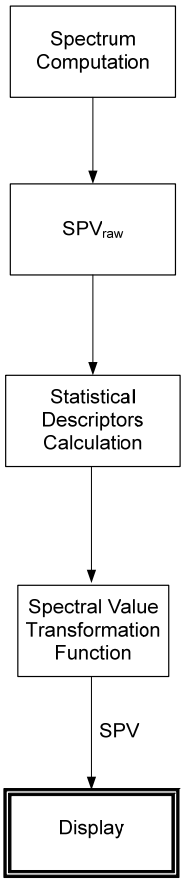

Figure 12 - High-level diagram of the algorithm for generating a SPV parametric image.

3.1. Spectrum Computation

For the ultrasound machine used in this research, data is generated as *in-phase* and *quadrature* (I/Q) data whereas for analysis we need the spectrum from the RF data. We therefore start by explaining how we reconstruct the RF spectrum from the I/Q data.

3.1.1. Reconstruction of the RF Spectrum from the I/Q Data

Converting the I/Q data back to the RF signal is impossible without upsampling and consequently introducing artificial samples. Instead, in this work, we have employed a different approach whereby the spectra of the *in-phase* and *quadrature* components are combined to reconstruct the RF spectrum at baseband (low frequencies), as detailed next.

A traditional I/Q demodulator is depicted in figure 13, where f_d denotes the demodulation frequency.

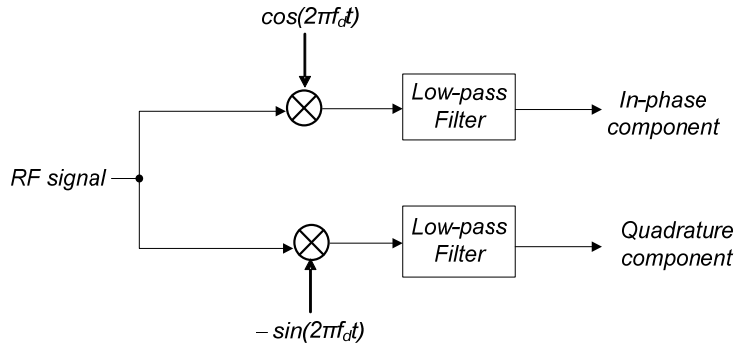

Figure 13 – A traditional I/Q demodulator where f_d denotes the demodulation frequency.

The *in-phase* component is given by

$$v_I(t) = v_{LPF}(t) * [v_{RF}(t)\cos(2\pi f_d t)] \qquad \text{(eq. 4)}$$

where $*$ denotes convolution and v_{RF} is the RF signal. Assuming that the low-pass filter is ideal, i.e.

$$V_{LPF}(f) = \begin{cases} 1, & |f| \le f_{cutoff} \\ 0, & otherwise \end{cases}$$

and rewriting equation 4 in terms of complex exponentials, yields

$$v_I(t) = v_{LPF}(t) * \left[v_{RF}(t) \frac{e^{j2\pi f_d t} + e^{-j2\pi f_d t}}{2} \right]$$

In the frequency domain, after applying the frequency-shift property of the Fourier transform, we have

$$V_I(f) = \frac{1}{2} V_{RF}(f - f_d) + \frac{1}{2} V_{RF}(f + f_d), \qquad |f| < f_{cutoff}$$

Similarly, for the *quadrature* component,

$$v_{\mathrm{Q}}(\mathrm{t}) = v_{\mathrm{LPF}}(\mathrm{t}) * [-v_{RF}(t)\sin(2\pi f_d t)] = v_{LPF}(t) * \left[-v_{RF}(t) \frac{e^{j2\pi f_d t} - e^{-j2\pi f_d t}}{2j} \right]$$

and, in the frequency domain,

$$\mathrm{V_Q(f)} = -\frac{1}{2j} V_{RF}(f - f_d) + \frac{1}{2j} V_{RF}(f + f_d), \qquad |f| < f_{cutoff}$$

Finally, the reconstructed RF spectrum is given by

$$\mathrm{V_{RF}}, \mathrm{(f)} = \mathrm{V_I(f)} + \mathrm{jV_Q(f)} = \mathrm{V_{RF}(f + f_d)}, \qquad |f| < f_{cutoff}$$

In summary, the reconstructed RF spectrum is a replica of the positive-frequency-spectrum of the RF signal down-shifted by an amount equal to f_d.

An advantage of using I/Q data is that a lower sampling frequency is employed without violating the Nyquist theorem. This means that a smaller number of samples have to be processed compared to RF data, reducing the computational cost in terms of both time and required memory.

3.1.2. Choice of the Windowing Function and its Length

It is desirable to resolve closely spaced spectral features as accurately as possible, which means reducing the *main lobe width* as much as possible (cf. section 2.5). Although the *rectangular* window has the narrowest main lobe, the first side lobe is only 13dB below the main peak, resulting in a huge degree of *leakage* [42]. Therefore, we selected the *Hamming* window, which exhibits the second narrowest main lobe amongst the windows mentioned in the previous chapter. The price paid is a lower relative side lobe attenuation (41dB) when compared with the *Blackman* window (57dB) [42].

The next step was to select the window length L. The value of L should be such that the window encompasses the ultrasound pulse length. In addition, L should be a power of two to optimize the speed of the FFT algorithm [43]. The length of the ultrasound pulse emitted by the *Zonare z.one* is unknown, so a phantom was built, consisting of an acoustic mirror (metal plate) immersed in water (see figure 14). The machine parameters were set to typical breast imaging values and a *L10-5 probe* (linear array, selected central frequency 8.3MHz) was used.

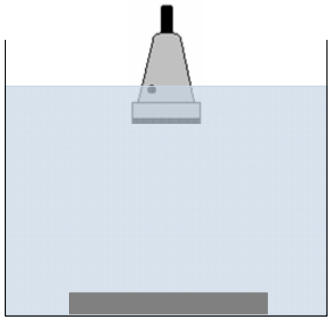

Figure 14 – Schematic of the phantom used in this experiment, consisting of a metal plate (at the bottom) immersed in water.

We observed that the received pulse had an average length of 20 samples. Thus, the closest power of two, $16 = 2^4$, was selected as the first value of L. Other window lengths (32, 64 and 128) were also investigated – this topic will be later discussed in this chapter.

3.2. Definition of the Spectral Peak Value

After emitting an acoustic signal with a given centre-frequency (more specifically, a Gaussian-pulse-modulated sinusoid) and computing the frequency spectrum of the backscattered echo from a subregion, the raw spectral peak value (SPV) for that region is defined as the maximum value of its frequency spectrum [100].

In practice, to reduce the effect of potential outliers, the raw SPV was computed as a weighted average of the maximum value and the values at the two neighbour discrete-frequencies (see figure 15).

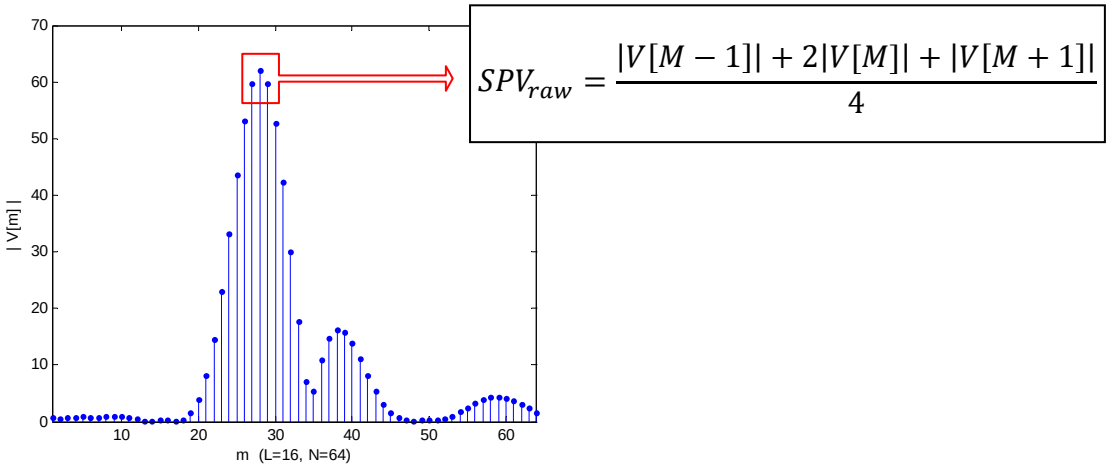

Figure 15 – Practical computation of raw SPVs. *M* is the discrete frequency *m* for which the spectrum *V* is maximum (in this case *M* = 28).

3.3. Computation of the raw SPVs for the Entire Scan Plane

Figure 16 depicts a schematic of the key implementation steps employed for the computation of the raw SPV for each pixel on the ultrasound scan plane from the *in-phase* and *quadrature* data available on the ultrasound machine. Let us take the pixel in red for example. First, the *Short-term Fourier Transform* of the coloured region (16-pixel window) is computed, as described in section 3.1. Next, the respective raw SPV is calculated, as described in section 3.2.

This process is repeated for each pixel on the scan plane. At the end, a 2D-matrix of raw SPVs is obtained.

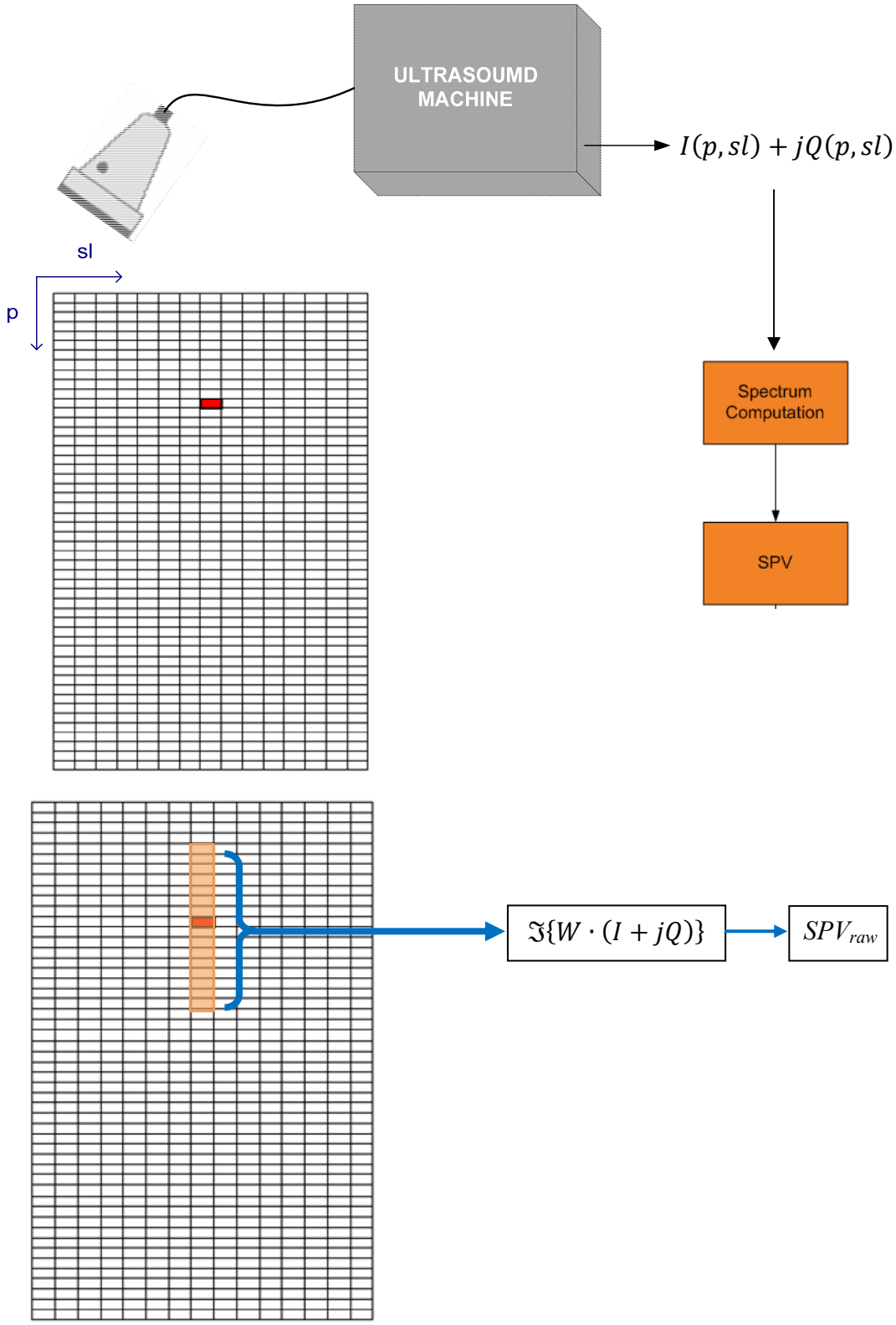

Figure 16 – Schematic of the key implementation steps employed for the computation of the raw SPV for each pixel *(p,sl)* on the scan plane from the I/Q data available on the ultrasound machine. Let us take the pixel in red for example. First, the *Short-term Fourier Transform* of the coloured region (window) is computed. Next, the respective raw SPV is calculated.

3.4. Spectral Peak Values and the Anatomy of the Breast

To better understand the spatial distribution of raw spectral peak values, *Quartile Maps* were plotted for different clinical cases. Specifically, pixels with a raw SPV lower than the first quartile (Q_1) were labelled in blue, between the first and second quartile (Q_2) in cyan, between the second and third quartile (Q_3) in yellow, and the remainder in red. Example *Quartile Maps* are shown in figure 17 to figure 19.

We observed that masses were consistently among the regions with a low raw SPV (raw SPV less than the median). Nonetheless, because of the wide dynamic range of *SPV* values, regions with low raw SPVs exhibit a poor contrast, making the assessment of those regions more difficult. On the other hand, high raw SPVs were mainly associated with the transducer–body interface (for example, at the top of figure 18(a)) or other strong reflections caused by anatomic structures, such as the *Cooper's ligaments* (for example, red arrows in figure 18(a)). The *Cooper's ligaments*, also known as suspensory ligaments of the breast [66], are composed of fibrous connective tissue that courses through the breast and helps maintain structural integrity (cf. figure 21) [12]. These ligaments are projected as linear or curvilinear bright structures on 2-D ultrasound images (for example, red arrows in figure 18(a)).

Due to its more homogenous composition, fat appears less echoic than the surrounding breast tissue (parenchyma) [12]. In addition to the subcutaneous and retromammary adipose tissue that surrounds the breast (cf. figure 22), fat is also interspersed throughout it, giving rise to darker areas on ultrasound images (for example, red arrows in figure 19). A schematic representation of the basic anatomy of the breast is presented in figure 22.

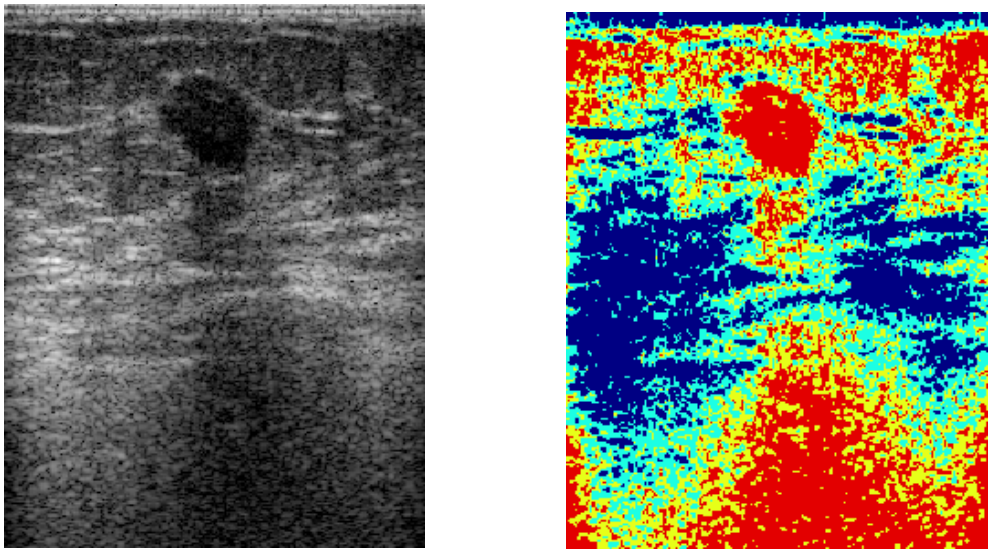

(a) (b)

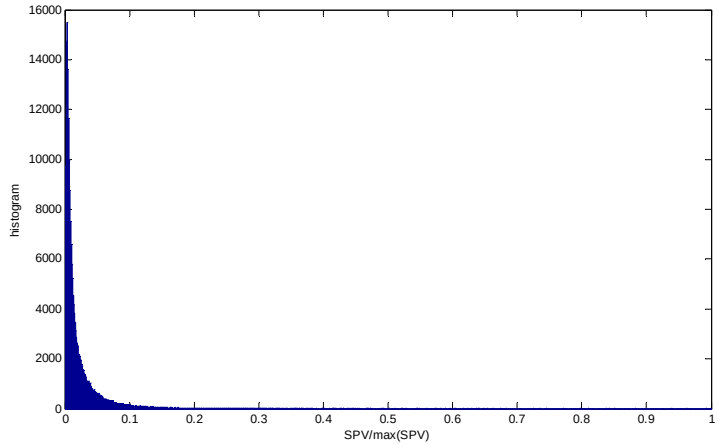

(c)

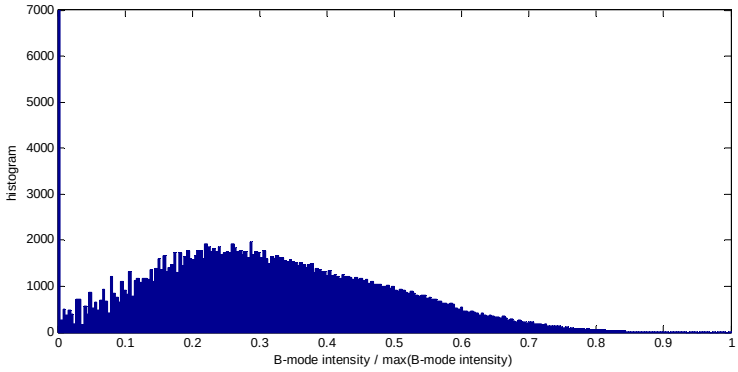

(d)

Figure 17 – Clinical case *#1* (DCIS, cf. annex II): (a) B-mode image; (b) *Quartile Map* of the raw *SPV*s – RED: $min \leq SPV \leq Q1$, $YELLOW$: $Q1 < SPV \leq Q2$, $CYAN$: $Q2 < SPV \leq Q3$, $BLUE$: $Q3 < SPV \leq max$; (c) histogram of the raw *SPV*s; (d) histogram of the B-mode intensities.

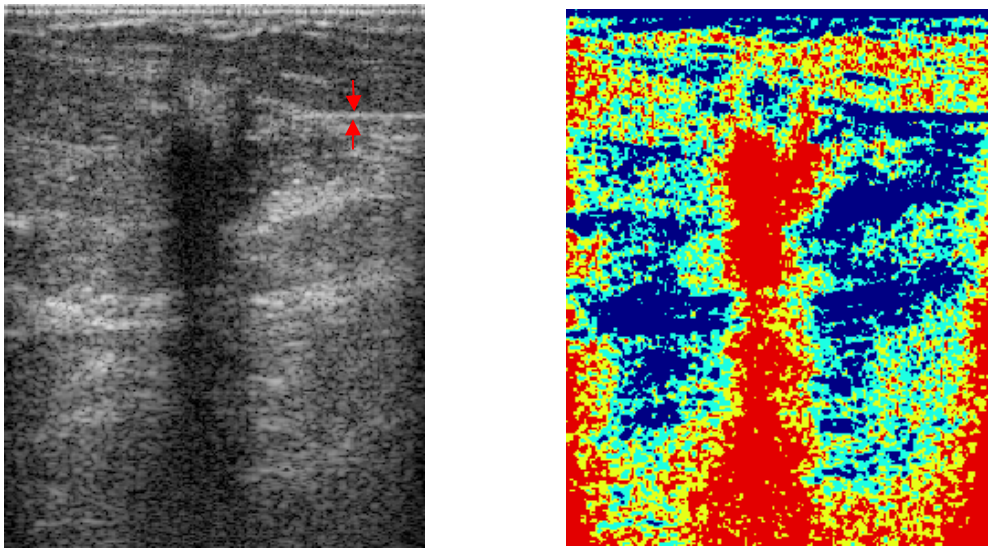

(a) (b)

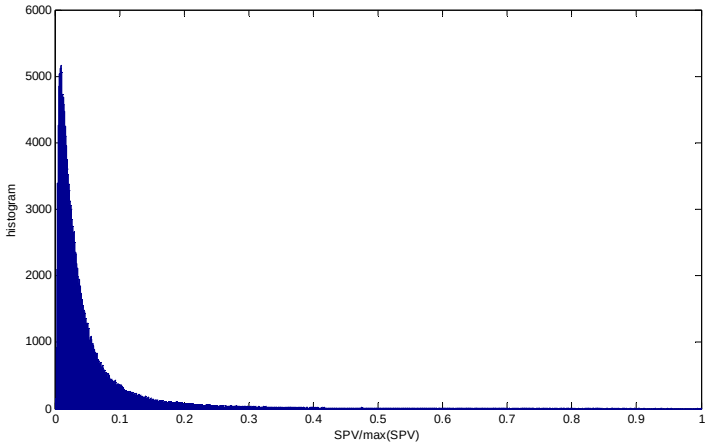

(c)

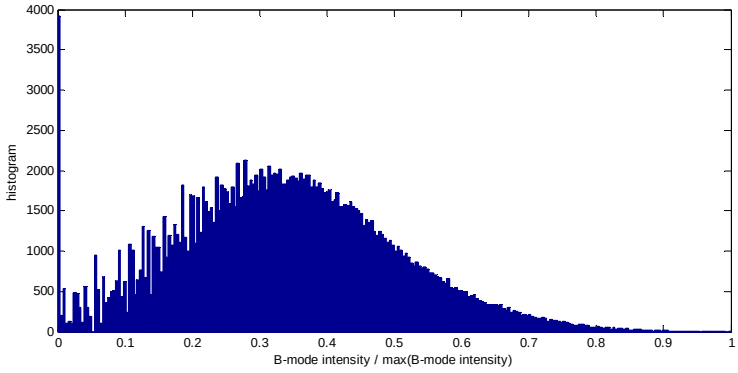

(d)

Figure 18 – Clinical case *#11* (DCIS+IDC, cf. annex II): (a) B-mode image – the arrows point to a Cooper's ligament; (b) *Quartile Map* of the raw *SPV*s – RED: $min \leq SPV \leq Q1$, $YELLOW$: $Q1 < SPV \leq Q2$, $CYAN$: $Q2 < SPV \leq Q3$, $BLUE$: $Q3 < SPV \leq max$; (c) histogram of the raw *SPV*s; (d) histogram of the B-mode intensities.

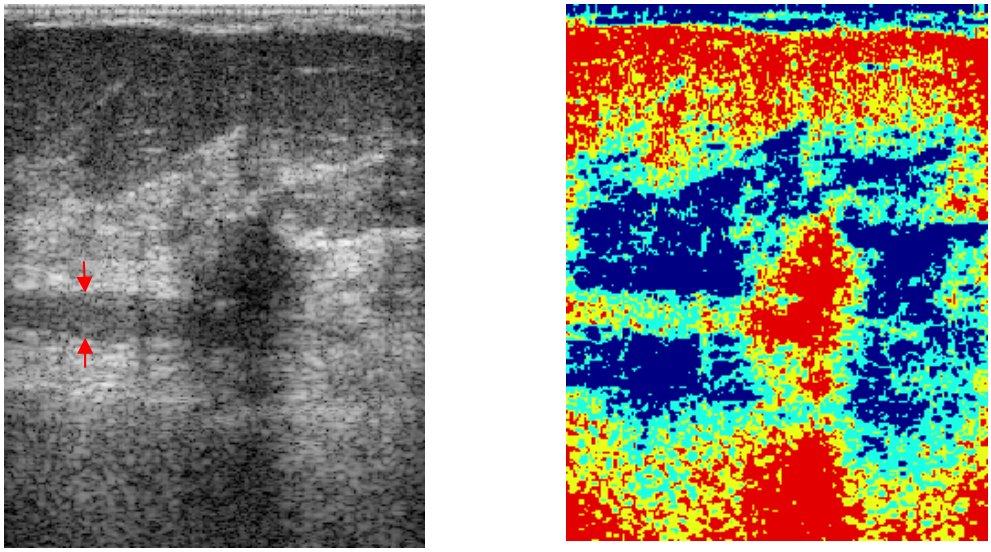

(a) (b)

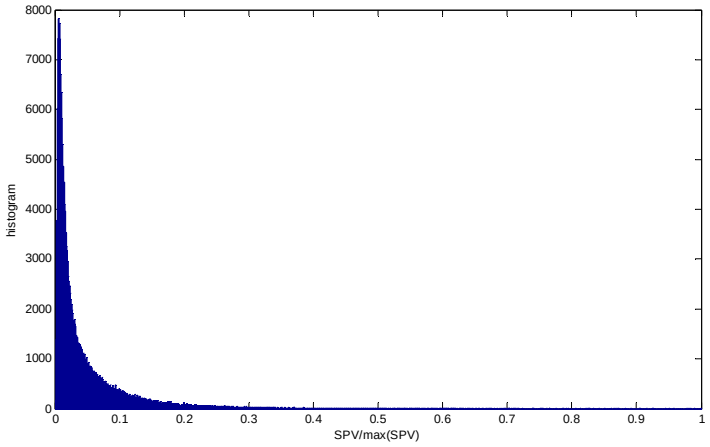

(c)

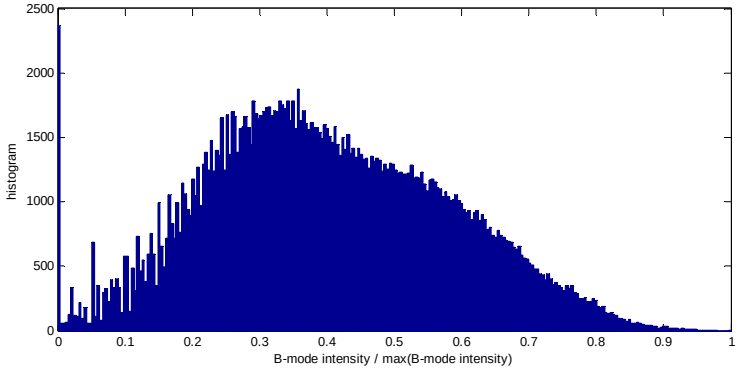

(d)

Figure 19 – Clinical case *#8* (IDC, cf. annex II): (a) B-mode image – the arrows point to adipose tissue (fat); (b) *Quartile Map* of the raw *SPV*s – RED: $min \leq SPV \leq Q1$, $YELLOW$: $Q1 < SPV \leq Q2$, $CYAN$: $Q2 < SPV \leq Q3$, $BLUE$: $Q3 < SPV \leq max$; (c) histogram of the raw *SPV*s; (d) histogram of the B-mode intensities.

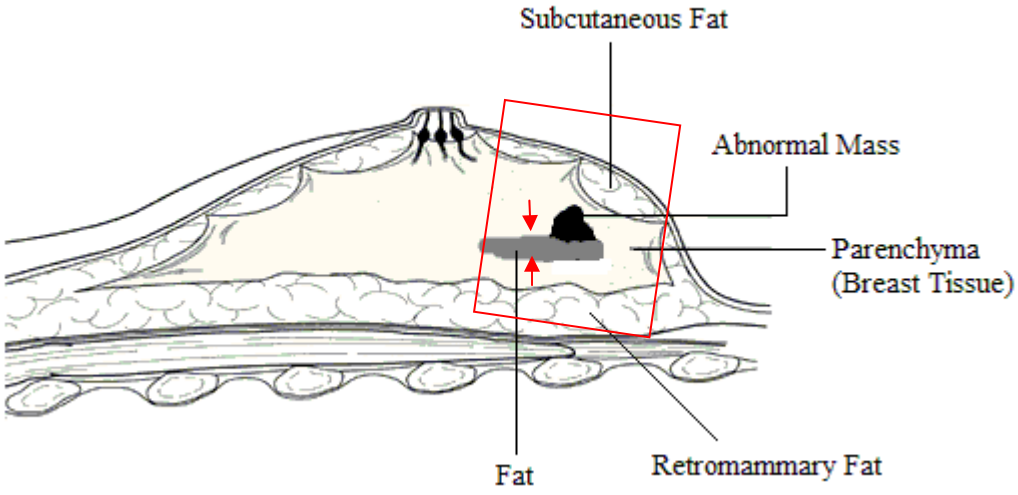

Figure 20 - This schematic depicts the key anatomic structures visible on figure 19 (a). Note that fatty tissue appears less echoic than the parenchyma (breast tissue).

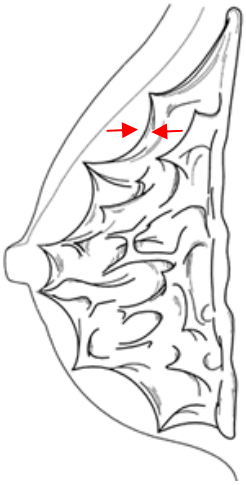

Figure 21 - If the glandular and fat portions of the breast are removed, what remains are the Cooper's ligaments (fibrous connective tissue) [12]. The arrows point to one of those ligaments.

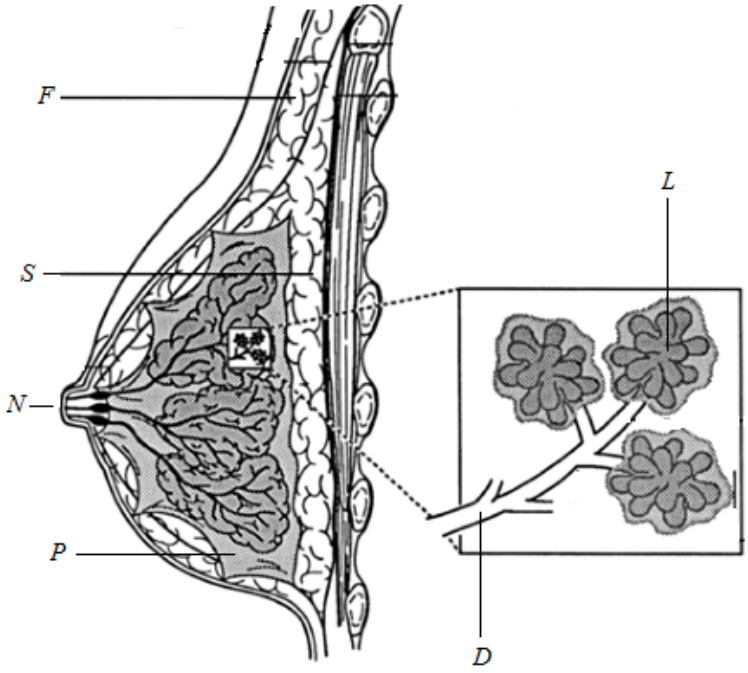

Figure 22 - Schematic representation of the basic anatomy of the breast: subcutaneous fat (*F*); retromammary fat (*S*); parenchyma (*P*); lactiferous ducts (*D*), which conduct the milk secreted in the lobules (*L*) to the nipple (*N*). This picture was adapted from [12].

3.4.1. Clinical Sample

The methods proposed in this work were tested on clinical data from 20 patients. The study had gained full ethical approval from the *NHS Health Research Authority* and each patient had given signed consent. Scanning of patients was conducted in clinic using the *Zonare z.one* ultrasound machine *(Zonare Medical Systems, Inc., California, USA)* and a *L10-5 probe* (linear array, selected central frequency of 8.3MHz, axial depth set to 50mm). During the scan, patients were asked to lay on

their backs on an elevated examination table (as in any standard ultrasound scan) and the raw I/Q data from the ultrasound machine was saved on disc. Each patient later underwent a surgical excision and the final diagnostic decision was known from the histopathology report provided to the radiologist.

Patient ages ranged from 51 to 67 years (all post-menopausal women). Figure 23 shows the distribution of patients according to mass type. Note that 16 were malignant masses and 4 were benign masses (cysts or fibro-adenomas).

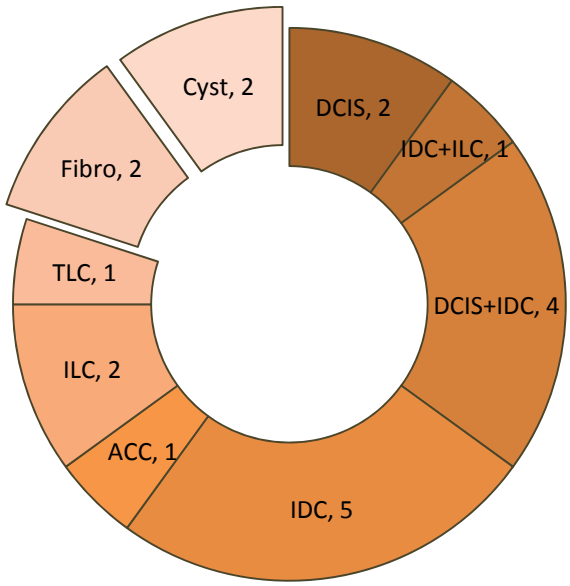

Figure 23 – Distribution of patients according to mass type – cf. appendix II for a full list of abbreviations.

3.5. Spectral Value Transformation Function

The observations in section 3.4 suggest the need for a spectral value transformation function to enhance contrast at low raw spectral peak values. One way to do this is to employ a quadratic transformation function of the form,

$$SPV = \begin{cases} \left(\frac{SPV_{raw} - min}{sp - min}\right)^2 & , SPV_{raw} \leq sp \\ 1 & , SPV_{raw} > sp \end{cases}$$

where *sp* is the saturation point and *min* is the minimum raw spectral peak value.

The key parameter is the saturation point, determining which pixels are saturated (i.e. clipped) or not. A high *sp* gives a low contrast enhancement. A low value can "hide" potentially useful clinical information.

3.5.1. Choice of the Saturation Point

As mentioned above, the main goal of the transformation function is to enhance the contrast of the spectral peak values in the lower part of the histogram. Thus, we want to map the low spectral peak values in such a way that the resulting histogram is as symmetrical and flat as possible. It translates into finding the saturation point *sp* that gives rise to a histogram with a smaller skewness (in absolute value) and a smaller kurtosis. Skewness *s* is a statistical descriptor that measures how asymmetrical a distribution is. In this case, how asymmetrical the histogram is.

$$s = \frac{1}{N}\sum_{j=1}^{N}\left(\frac{SPV_j - \mu}{\sigma}\right)^3$$

where N is the number of spectral peak values, μ is their mean value and σ is their standard deviation.

On the other hand, kurtosis k is a statistical descriptor that measures the peakedness of a distribution.

$$k = \frac{1}{N}\sum_{j=1}^{N}\left(\frac{SPV_j - \mu}{\sigma}\right)^4$$

The lower the kurtosis value, the more evenly distributed the spectral peak values would be on the histogram.

Five different saturation points were investigated as reported in table 2 and figure 24 (Q_1, Q_2, Q_3 denotes the first, second and third quartile of the raw spectral peak value histogram, respectively). The average of the first and second quartile – $sp = (Q_1 + Q_2)/2$ – was found to give the better results amongst the five investigated saturation points, i.e. this saturation point gave rise to a less asymmetrical (lower absolute skewness) and more evenly distributed (lower kurtosis) histogram.

For instance, let us consider the clinical case in figure 17. The final SPV parametric image, using $sp = (Q_1 + Q_2)/2$, is shown in figure 25. The same gray-scale colormap was employed to display both B-mode and SPV images in order to prevent any colormap-related visual enhancement.

Table 2 – Statistics for five saturation points (Q_1, Q_2, Q_3 denotes the first, second and third quartile of the raw spectral peak value histogram, respectively)

# patient	*|skewness|, |S|, when sp =*					*kurtosis, K, when sp =*				
	Q1	**(Q1+Q2)/2**	**Q2**	**(Q2+Q3)/2**	**Q3**	**Q1**	**(Q1+Q2)/2**	**Q2**	**(Q2+Q3)/2**	**Q3**
1	0.238	0.087	0.296	0.667	0.905	2.105	2.018	2.067	2.448	2.868
2	0.023	0.086	0.191	0.393	0.588	1.895	1.876	1.907	2.077	2.339
3	0.012	0.167	0.251	0.482	0.705	1.931	1.885	1.906	2.163	2.520
4	0.345	0.155	0.007	0.276	0.493	2.202	2.053	2.008	2.085	2.297
5	0.260	0.087	0.075	0.346	0.562	2.052	1.990	1.979	2.109	2.357
6	0.173	0.069	0.241	0.535	0.727	2.057	1.967	2.003	2.250	2.520
7	0.230	0.021	0.187	0.440	0.634	2.085	1.988	1.982	2.148	2.397
8	0.183	0.166	0.390	0.779	0.983	2.112	2.023	2.130	2.609	2.971
9	0.331	0.009	0.231	0.739	1.023	2.237	2.054	2.093	2.628	3.182
10	0.250	0.059	0.094	0.359	0.568	2.103	1.978	1.971	2.109	2.350
11	0.141	0.066	0.209	0.425	0.614	2.036	1.943	1.957	2.109	2.363
12	0.274	0.052	0.117	0.402	0.617	2.134	2.004	1.988	2.151	2.413
13	0.102	0.175	0.303	0.494	0.651	2.015	1.963	1.971	2.136	2.366
14	0.242	0.096	0.039	0.265	0.470	2.050	1.968	1.955	2.040	2.258
15	0.332	0.099	0.090	0.412	0.654	2.192	2.045	2.016	2.189	2.499
16	0.087	0.223	0.374	0.645	0.867	2.052	1.986	2.034	2.357	2.786
17	0.367	0.126	0.071	0.417	0.661	2.253	2.076	2.036	2.215	2.508
18	0.429	0.274	0.129	0.126	0.345	2.310	2.145	2.062	2.065	2.213
19	0.294	0.081	0.100	0.414	0.645	2.167	2.020	2.006	2.180	2.473
20	0.248	0.072	0.283	0.623	0.830	2.158	2.021	2.064	2.376	2.693
mean	**0.228**	**0.108**	**0.184**	**0.462**	**0.677**	**2.107**	**1.960**	**2.007**	**2.222**	**2.519**

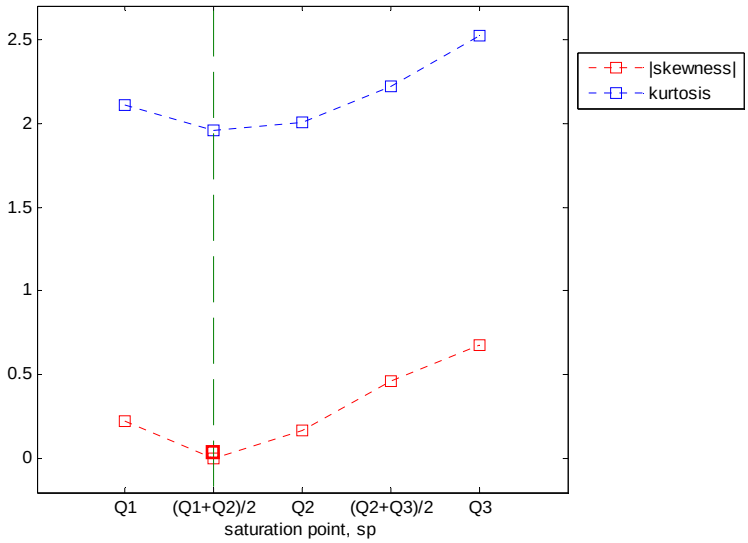

Figure 24 – Average skewness (in absolute value) and kurtosis for the five saturation points.

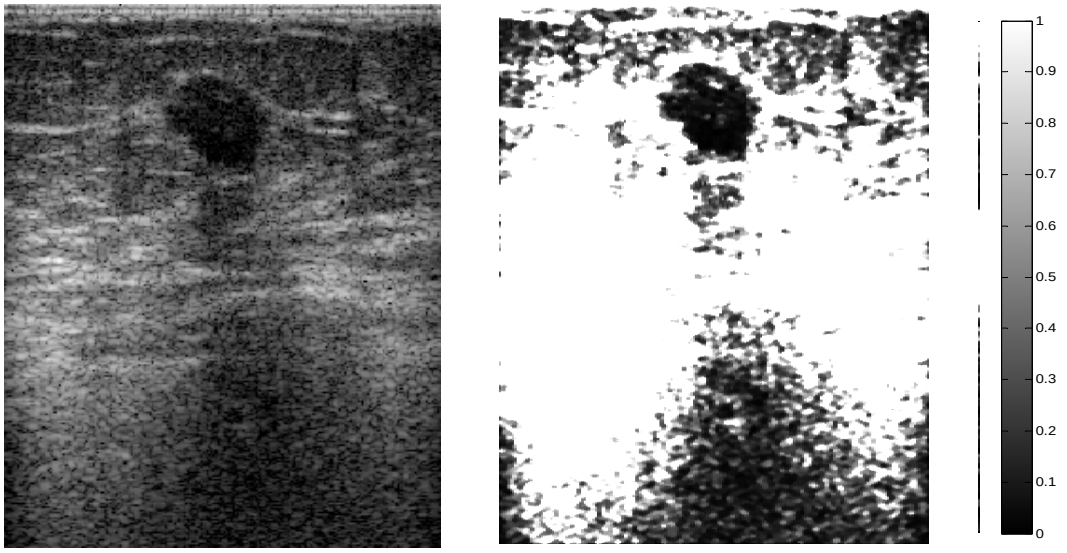

(a) (b) (c)

Figure 25 – Clinical case *#1* (DCIS, cf. annex II): (a) B-mode image; (b) SPV parametric image for *sp = (Q1+Q2)/2*; (c) the same gray-scale colormap was employed to display both images in order to prevent any colormap-related visual enhancement.

3.6. Quantitative and Comparative Analysis of SPV Images

In this section, a quantitative comparison is presented among ultrasound images generated by four different estimates of the degree of echogenicity: the log-compressed envelope of the RF data (B-mode imaging); the integrated backscatter coefficient (IBS imaging); the spectral intercept of the dB-linearized spectrum (SI imaging) and the spectral peak value (SPV imaging). Three metrics[§] were used to compare and contrast those types of image: two intensity-based metrics – variation of contrast and correlation coefficient – and one entropy-based metric – variation of information content.

[§] We used global metrics to encompass not only the tumour region but the whole scan plane, including anatomical structures such as the Cooper's ligaments, adipose tissue, etc.

3.6.1. Intensity-based Metrics: Definition

Let $\boldsymbol{X}$ and $\boldsymbol{Y}$ be two images with size *I-by-J*. Let X_{ij} and Y_{ij} be the intensity value at pixel *(i,j)* in image $\boldsymbol{X}$ and $\boldsymbol{Y}$, respectively. The following intensity-based statistical descriptors can be defined:

$$\bar{X} = \frac{1}{IJ}\sum_{i=1}^{I}\sum_{j=1}^{J} X_{ij} \; ; \qquad \bar{Y} = \frac{1}{IJ}\sum_{i=1}^{I}\sum_{j=1}^{J} Y_{ij}$$

$$\sigma_X = \sqrt{\frac{1}{IJ-1}\sum_{i=1}^{I}\sum_{j=1}^{J}\left(X_{ij}-\bar{X}\right)^2} \; ; \quad \sigma_Y = \sqrt{\frac{1}{IJ-1}\sum_{i=1}^{I}\sum_{j=1}^{J}\left(Y_{ij}-\bar{Y}\right)^2}$$

$$\sigma_{XY} = \frac{1}{IJ-1}\sum_{i=1}^{I}\sum_{j=1}^{J}\left(X_{ij}-\bar{X}\right)\left(Y_{ij}-\bar{Y}\right)$$

where $\bar{X}$ and $\bar{Y}$ is the average intensity values for image $\boldsymbol{X}$ and $\boldsymbol{Y}$, σ_X and σ_Y is the standard deviation of the intensity value distribution for image $\boldsymbol{X}$ an $\boldsymbol{Y}$ and σ_{XY} is the covariance between those intensity value distributions.

The standard deviation σ_X and σ_Y can be viewed as an estimate of contrast [101], [102]. Statistically, σ_X and σ_Y measures the dispersion of the intensity values in relation to the average intensity value.

$$C(X) = \sigma_X \; ; \quad C(Y) = \sigma_Y$$

The variation of contrast in image $\boldsymbol{X}$ compared to image $\boldsymbol{Y}$ as a percentage, $VC_Y(X)$, can be defined as follows,

$$VC_Y(X) = \frac{C(X) - C(Y)}{C(Y)} \cdot 100$$

It estimates the percentage of contrast change in image $\boldsymbol{X}$ compared to image $\boldsymbol{Y}$.

Another employed metric was the correlation coefficient between intensity values in image $\boldsymbol{X}$ and $\boldsymbol{Y}$:

$$Corr(X,Y) = \frac{\sigma_{XY}}{\sigma_X \sigma_Y}$$

It measures the degree of linear correlation between the intensity values in image $\boldsymbol{X}$ and $\boldsymbol{Y}$. It varies between -1 and 1, assuming the extreme values when there is a perfect linear relation in the opposite or same direction, respectively ([103]).

3.6.2. Entropy-based Metrics: Definition

Let us consider two datasets: $\boldsymbol{X} = \{x_k | k = 1, 2, \dots, n\}$ and $\boldsymbol{Y} = \{y_k | k = 1, 2, \dots, n\}$. Note that in terms of an image, x_k can be seen as a pixel intensity value (n is the number of different intensity values).

The information entropy (or Shannon entropy [104]) for dataset $\boldsymbol{X}$ is defined as

$$H(X) = -\sum_{k=1}^{n} p(x_k) \cdot log_2\big(p(x_k)\big)$$

where $p(x_k)$ is the probability that $X = x_k$. In terms of an image, $p(x_k)$ is the probability that a certain pixel has intensity value x_k. Entropy measures the uncertainty of information content and can be seen as an estimate of the diversity of information content (cf. [104] for details). One may also define the conditional entropy of $\boldsymbol{X}$ given $\boldsymbol{Y}$ as follows [105] [106],

$$H(X|Y) = -\sum_{z=1}^{n} p(y_z) \sum_{k=1}^{n} p(x_k|y_z) \cdot log_2\big(p(x_k|y_z)\big)$$

where $p(x_{k,}|y_{z,})$ is the probability that $X = x_k$ given that $Y = y_z$. The conditional entropy can be understood as the amount of uncertainty in dataset $\boldsymbol{X}$ given that we know the values of dataset $\boldsymbol{Y}$.

In order to measure the variation in information content between two images, we made use of the variation of information metric (VI metric) which is the sum of the conditional entropies [106], [107]:

$$VI(X,Y) = H(X|Y) + H(Y|X)$$

Note that:

$$0 \leq VI(X,Y) \leq H(X) + H(Y)$$

When the sets are identical or dependent, $VI(X,Y)$ equals zero. On the other hand, when the sets are independent, i.e.

$$\begin{cases} p(x|y) = p(x) \\ p(y|x) = p(y) \end{cases}$$

then,

$$\begin{cases} H(X|Y) = H(X) \\ H(Y|X) = H(Y) \end{cases}$$

and $VI(X,Y)$ assumes its maximum value ([105]), i.e.,

$$VI(X,Y) = H(X) + H(Y)$$

Lower $VI(X,Y)$ implies higher similarity in information content between the two images. When the information content is the same, $VI(X,Y)$ equals zero. When the information content is completely different, i.e. when knowing the information content of one image tells nothing about the information content of the other image,

$VI(X,Y)$ is maximum. In other words, $VI(X,Y)$ is minimized when there is a one-to-one mapping between the intensity values in image $\boldsymbol{X}$ and their counterparts in image $\boldsymbol{Y}$ and $VI(X,Y)$ increases as the statistical relationship between $\boldsymbol{X}$ and $\boldsymbol{Y}$ weakens ([108]). A detailed analysis of the VI metric properties is available in [106].

We can normalize VI(X, Y) onto the interval $[0, 1]$ as follows,

$$VI_{norm}(X,Y) = \frac{VI(X,Y)}{H(X) + H(Y)}$$

In this work, we used the normalized variation of information metric, $VI_{norm}(X,Y)$, to evaluate the similarity in terms of global information content between two images.

3.6.3. B-mode Image versus SPV Image

Let us begin by a quantitative comparison between the B-mode image and the SPV parametric image (using a Hamming window of length 16 pixels and padded with 48 zeros[**]). Table 8, in annex III, shows the figures for the variation in contrast, $VC_{Bmode}(SPV)$, correlation coefficient, *Corr(Bmode,SPV)*, and the variation in information content, $VI_{norm}(Bmode,SPV)$, between those images for each patient.

A contrast increase in the SPV images is reported for all patients: on average, the contrast increases by 60.71% in SPV images compared to B-mode images. From the scatter plot in figure 26, we can observe that the increase in global contrast is mainly due to a significant contrast increase in hypo-echoic regions.

[**] Cf. section 2.5.2 for details on zero-padding.

Although, both images are generated from the same I/Q raw data for each patient, a relatively low correlation coefficient indicates the presence of non-linear changes/differences in their structural information ([102]). In fact, hypo-echoic regions appear more enhanced in SPV images than in B-mode images, i.e. more detailed information can be seen in those regions – see an examples in figure 26 (the same gray-scale colormap was employed to display both images in order to prevent any colormap-related visual enhancement).

Moreover, the figures for the variation of information content support the idea that some information available in the SPV image is not available in the B-mode image. In fact, those figures are very high considering that we are talking about the same patient and both images are generated from the same raw data. It indicates that B-mode and SPV algorithms are extracting and providing to a radiologist some different information from the same raw data.

However, it is important to understand whether such different information would be clinically valuable or not. In order to investigate it, a clinical pilot study was conducted on 20 patients as reported and discussed in section 3.7.

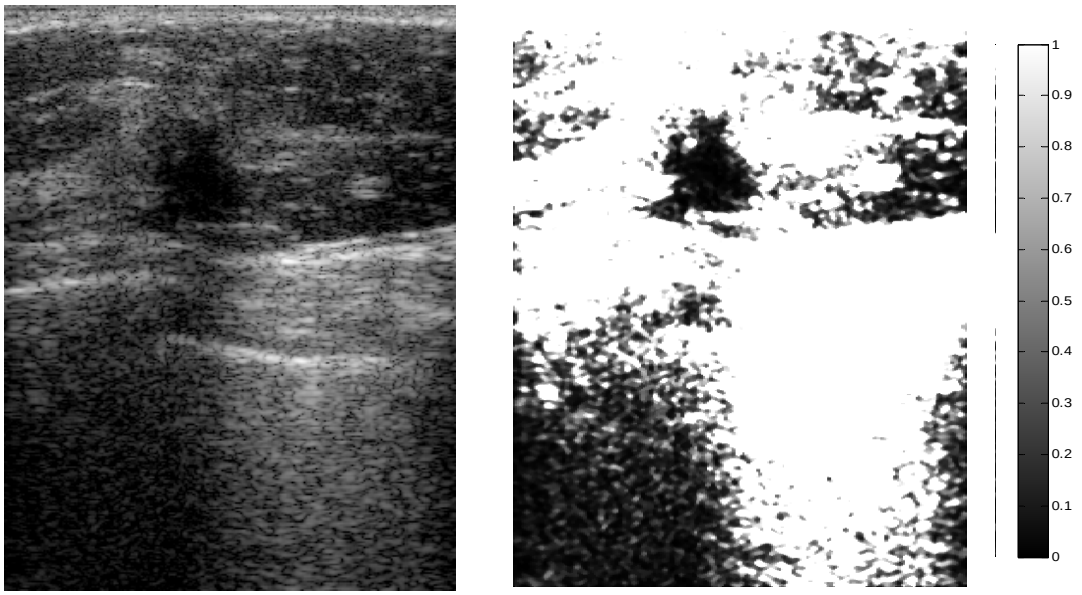

(a) (b) (c)

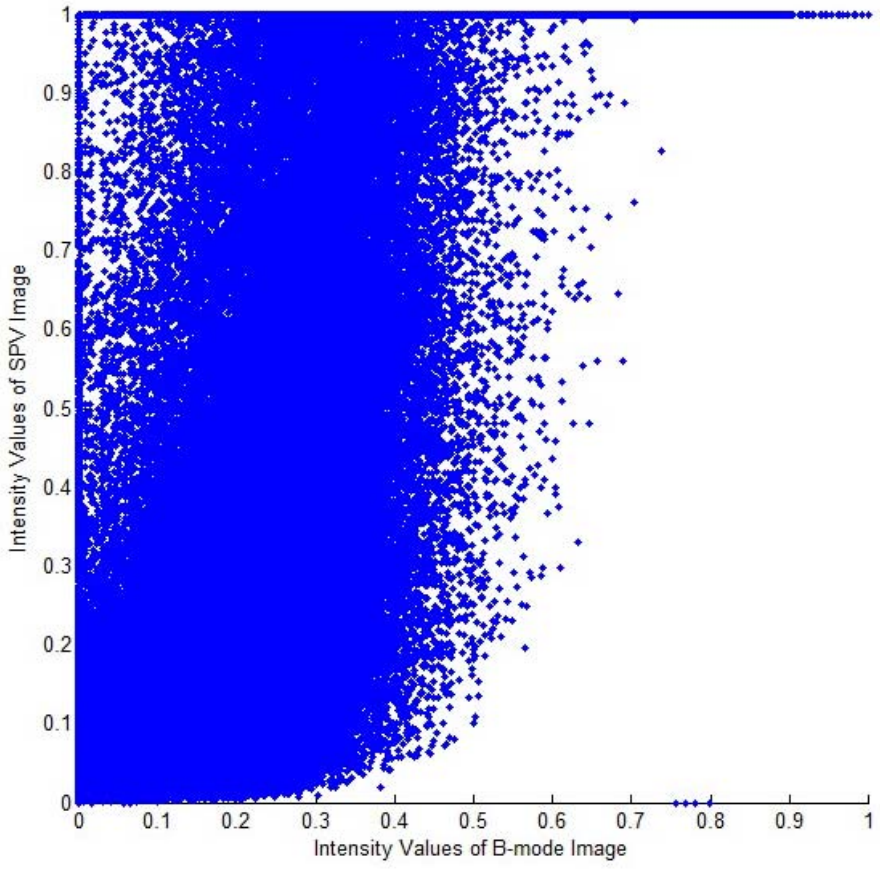

(d)

Figure 26 – Clinical case *#16* (ILC, cf. annex II): (a) B-mode image; (b) SPV parametric image; (c) the same gray-scale colormap was used to display both images; (d) scatter plot of B-mode intensity values versus SPV intensity values.

3.6.4. The Impact of Window Size on SPV Images

Let us now analyse how the window length affects the SPV parametric images. The classic *uncertainty principle of the Fourier Transform* (cf. chapter 2) tells that we can either have high resolution in time (equivalent to spatial resolution on the scan plane) or high resolution in frequency but not both at the same time. The window length allows us to trade between the two. A shorter window generates a coarser spectrum with a lower resolution but increases the spatial resolution on the scan plane, i.e. increases the capability of discriminating between smaller contiguous regions. The last point is of major importance to precisely resolve the mass boundaries.

Four different window lengths were investigated:

- ***W16***: Hamming window of length 16 pixels and padded with 48 zeros[††] ;
- ***W32***: Hamming window of length 32 pixels and padded with 32 zeros;
- ***W64***: Hamming window of length 64 pixels;
- ***W128***: Hamming window of length 128 pixels.

Figure 27 to figure 29 summarise the evolution of the three previously discussed metrics – variation of contrast, $VC_{Bmode}(SPV)$, correlation coefficient, *Corr(Bmode,SPV)*, and variation of information content, $VI_{norm}(Bmode,SPV)$ – with the size of the window. Statistics for all window sizes and for all patients are given in annex III.

[††] Cf. section 2.5.2 for details on zero-padding.

From figure 27 we observe that the variation of contrast metric keeps, on average, almost constant. However, the correlation coefficient decreases consistently as window length increases for all clinical cases (cf. figure 28). It can be explained by the fact that a larger number of contiguous regions with different types of tissue are entailed in the computation of the same spectrum, resulting in less correlated structural information between the SPV and B-mode images. It may also explain the observed increase in the variation of information metric, on average, as window length increases (cf. figure 29).

As window size increases, the capability of discriminating contiguous regions with different types of tissue decreases. Consequently, the capability of precisely resolving the mass boundaries decreases as shown in figure 30 where the mass boundary is less sharp for larger windows.

In conclusion, no significant advantage was found in employing windows larger than $L = 16$. On the contrary, when window length increases, the SPV parametric image becomes more blurred and the mass boundaries less sharp (see figure 30 for an example). Therefore, we conclude that a window size of $L = 16$ is sufficient and use this in subsequent work.

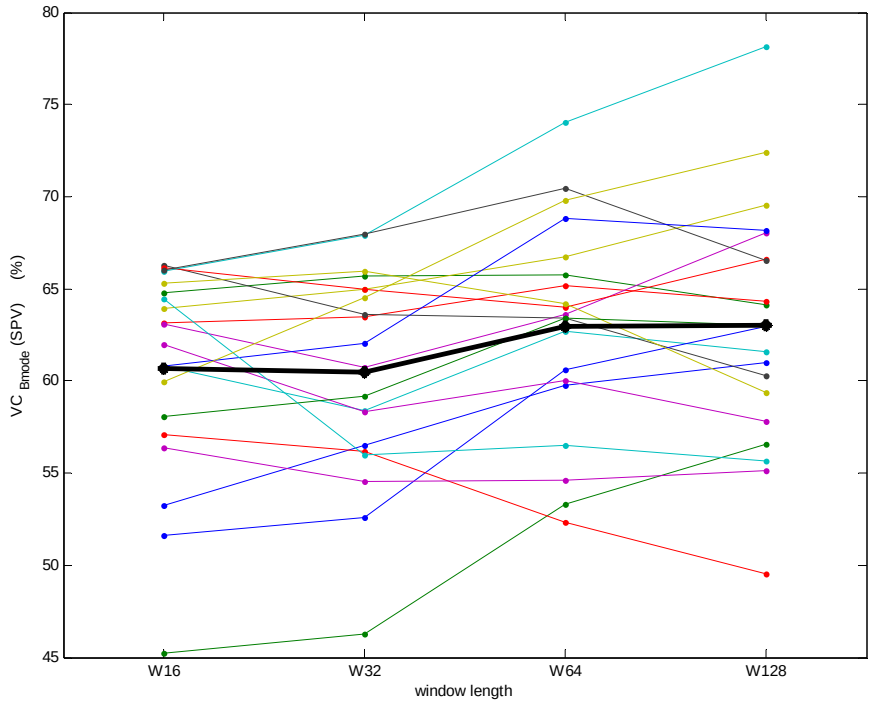

Figure 27 – Evolution of the variation of contrast, $VC_{Bmode}(SPV)$, with the size of the window. Each line represents a different patient. The bold line corresponds to the average.

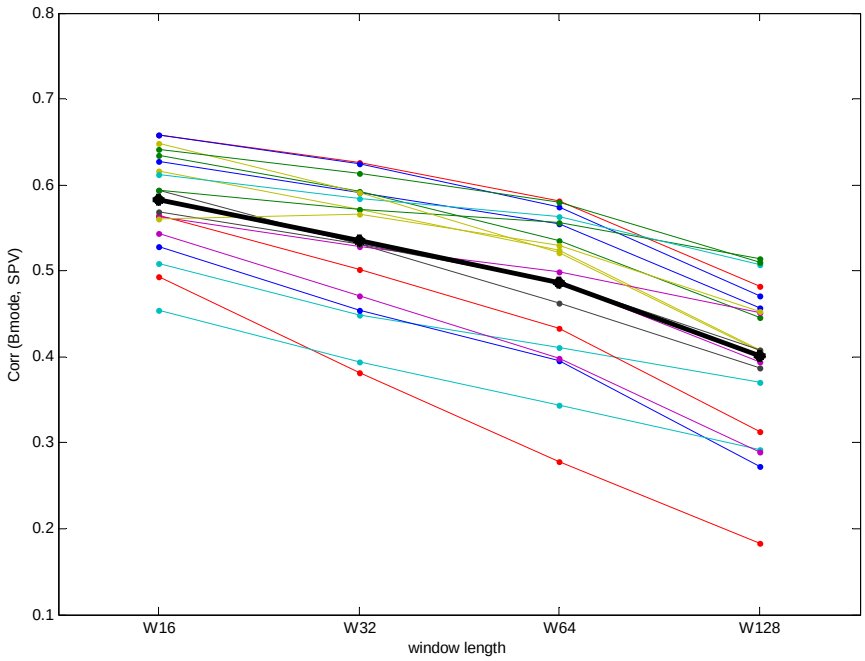

Figure 28 – Evolution of the correlation coefficient, *Corr(Bmode,SPV)*, with the size of the window. Each line represents a different patient. The bold line corresponds to the average.

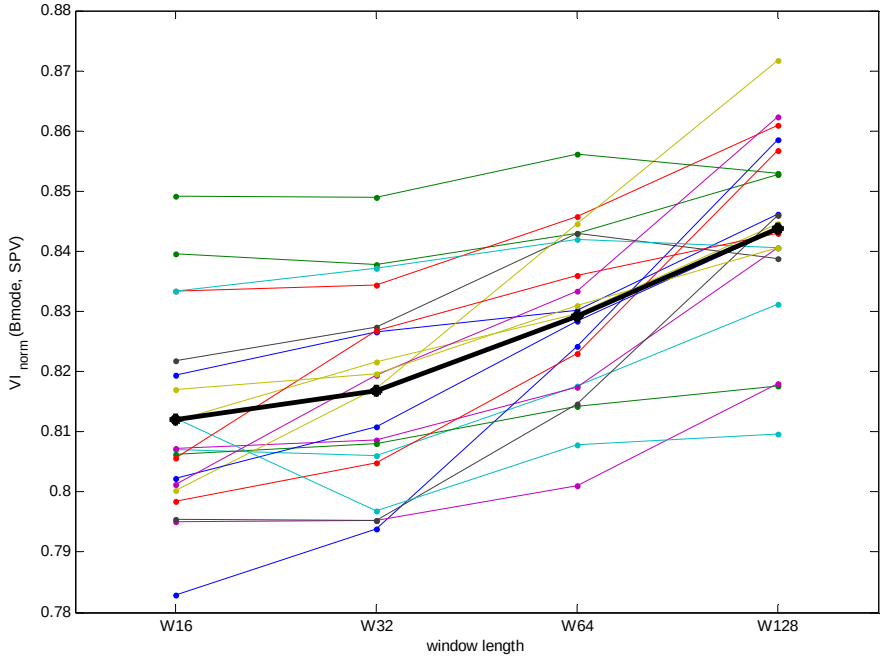

Figure 29 – Evolution of the variation of information content, $VI_{norm}(Bmode,SPV)$, with the size of the window. Each line represents a different patient. The bold line corresponds to the average.

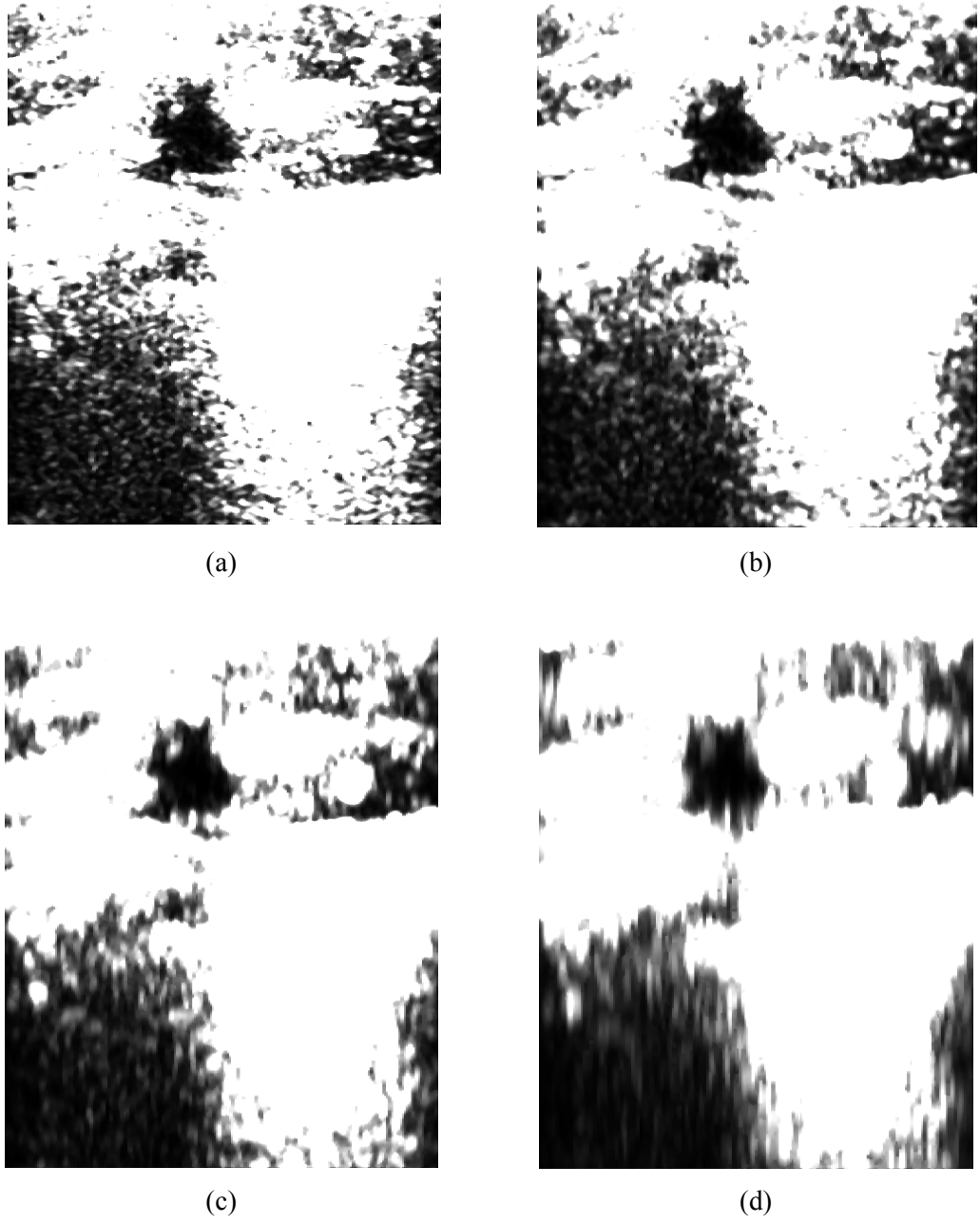

(a) (b)

(c) (d)

Figure 30 – Clinical case *#16* (ILC, cf. annex II): SPV parametric image using window ***W16*** (a), ***W32*** (b), ***W64*** (c), ***W128*** (d).

3.6.5. SPV Algorithm versus Band-pass Filtering

One of the key advantages of SPV images is the fact that, for each pixel, the SPV algorithm always retains the highest magnitude of the spectrum. As a higher magnitude contributes to a better signal-to-noise ratio ([35]), the spectral value with the best signal-to-noise ratio is selected.

Although we may be tempted to think that similar results would be obtained by simply employing a (narrow) band-pass filter centred around the centre-frequency *fc*, the fact of the matter is that the spectral peak location (i.e. the frequency at which the spectral peak occurs) varies very often. That information is summarised in the 3D-histogram in figure 31(a). For each patient, it shows the percentage of pixels where the spectral peak occurred at frequency *f*. In figure 31(b) a histogram summarises the overall information in our 20-case sample. Only in 16.8% of the pixels, did the spectral peak occur at the centre-frequency (*fc* = 8.3MHz). In 93.2% of the pixels, it occurred between 7.5MHz and 9.1MHz. The magnitude of the spectral peak shift was also investigated as a potential parameter to generate ultrasound parametric images – cf. annex IV for details.

Figure 32 illustrates why a band-pass filter centred around *fc* would not be a good substitute for the SPV algorithm. In this example case, the spectrum for three different locations along the scan line *100* (marked in red on the B-mode image) is shown. For spectrum *S2* and *S3*, because of the notch around *fc*, the band-pass filter would return a low magnitude value (with a poor signal-to noise ratio) instead of returning the maximum magnitude value.

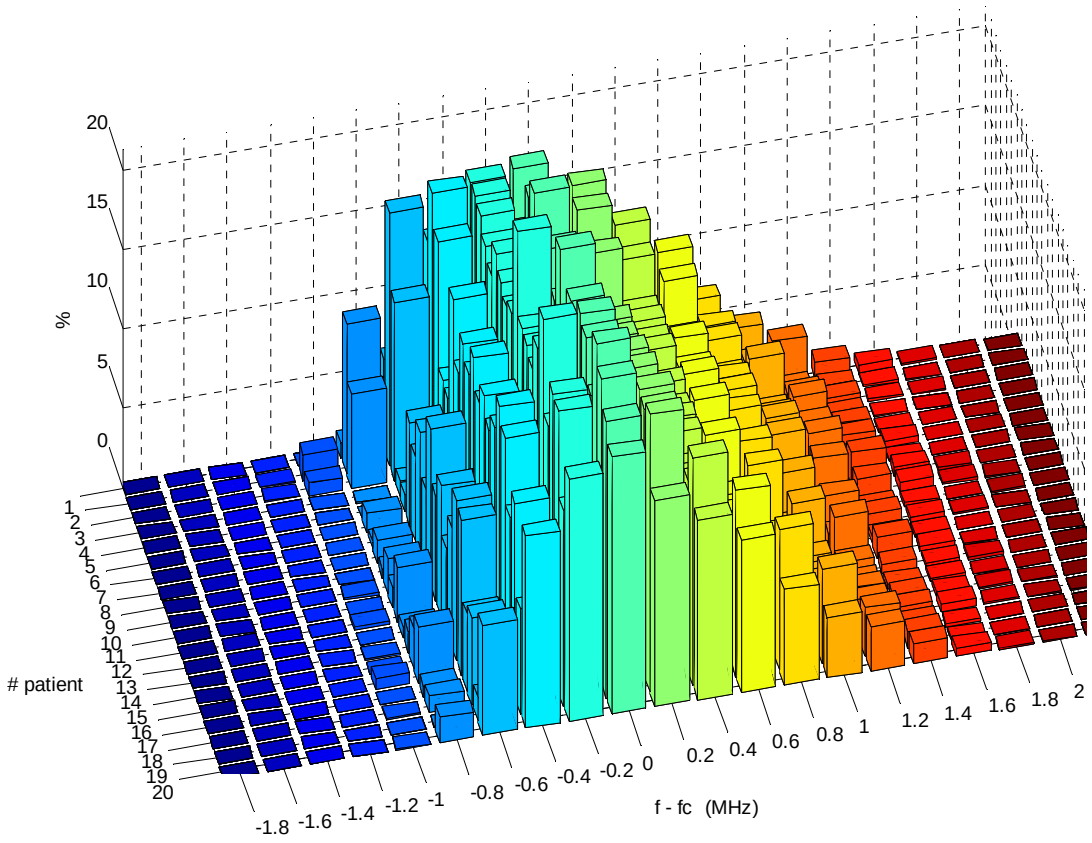

(a)

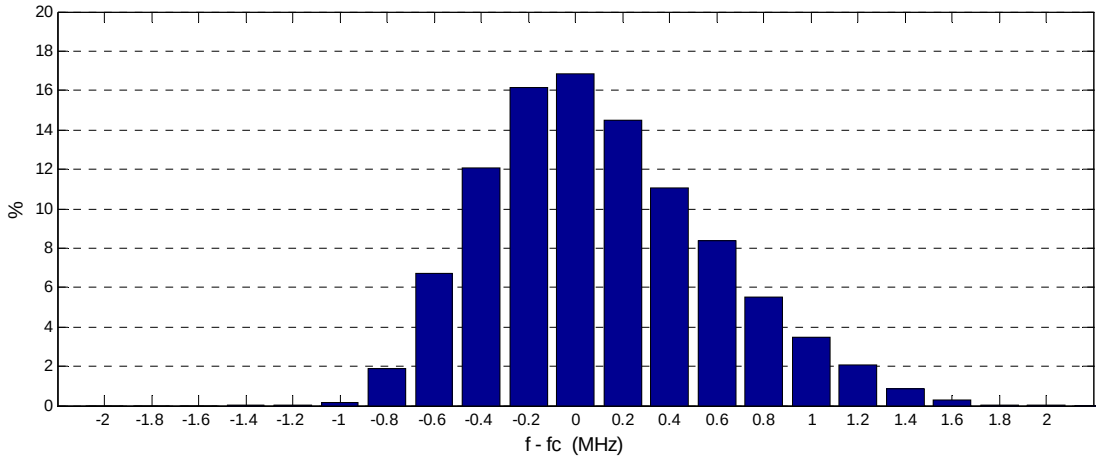

(b)

Figure 31 – (a) 3D-histogram showing the spectral peak occurrence at frequency *f* (centre-frequency *fc* = 8.3MHz) for each patient; (b) histogram summarising the spectral peak occurrence at frequency *f* for all 20 clinical cases.

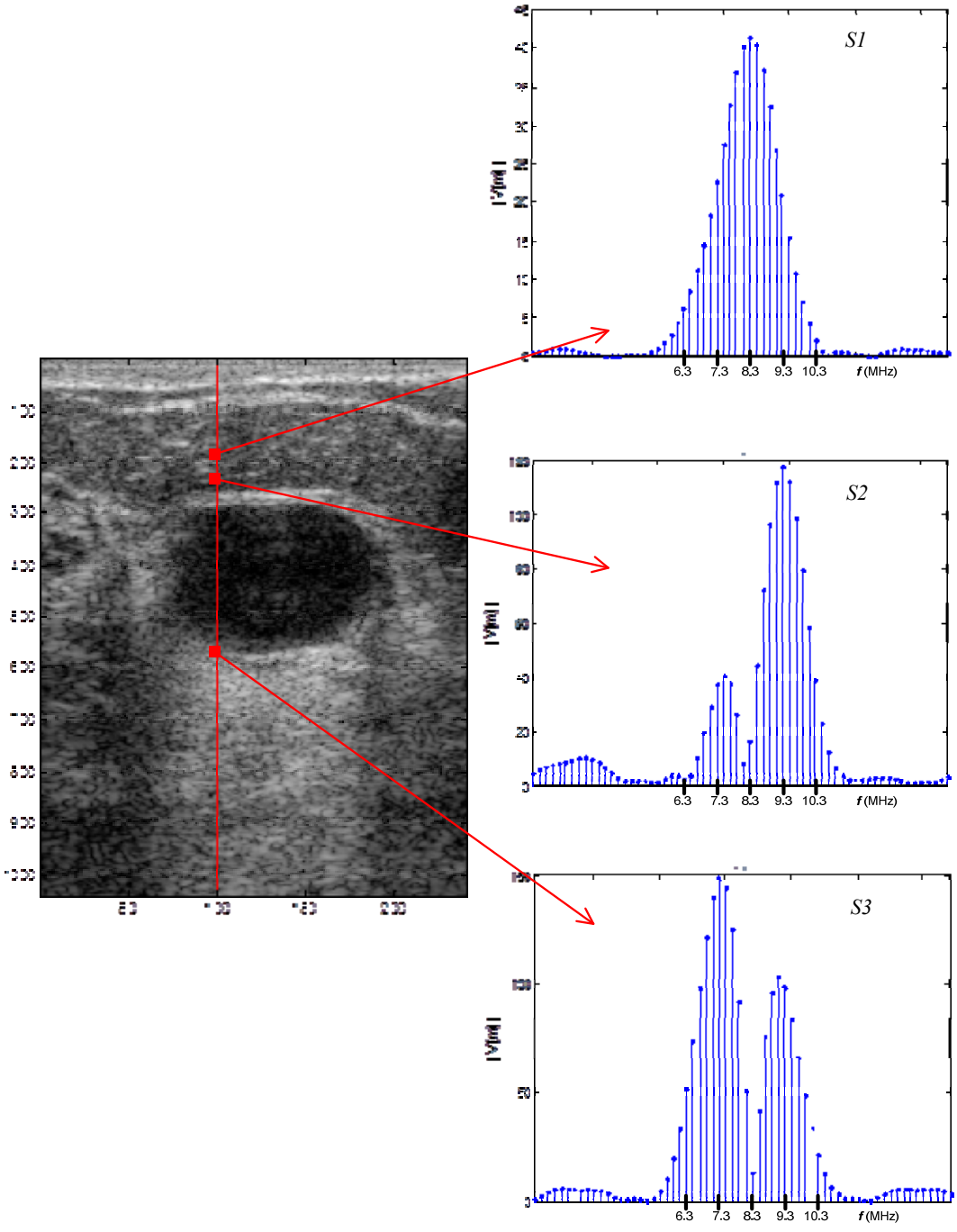

Figure 32 – B-mode ultrasound image (clinical case *#3* – cyst) and three spectra computed along scan line *100* (marked in red on the B-mode image). A centre-frequency of 8.3MHz and a window ***W16*** was used.

3.6.6. SPV image versus IBS image

Next we investigate the use of the sum of the squared spectral magnitudes, also known as the integrated backscatter (IBS). As discussed in section 2.7, some researchers ([68] [67]) have proposed the use of IBS as an estimate of the backscattered energy and, therefore, an estimate of the degree of echogenicity. However, the IBS estimate appeared poor when compared with SPV in generating parametric images with increased contrast along the mass boundaries. From visual inspection (see an example in figure 33), B-mode and IBS images appeared very similar in terms of the structural information they provide. It is corroborated by a low variation in information content $VI_{norm}(Bmode,IBS)$ = 0.57 (as opposed to $VI_{norm}(Bmode,SPV)$ = 0.81 for SPV images) and by a high correlation between their intensity values $Corr(Bmode,IBS)$ = 0.81 (as opposed to $Corr(Bmode,SPV)$ = 0.58 for SPV images) – see table 3. In terms of contrast, it remains practically the same between the B-mode and IBS parametric image (-6.06% denotes a slight decrease in contrast compared to B-mode). Detailed statistics for all patients are available in annex III.

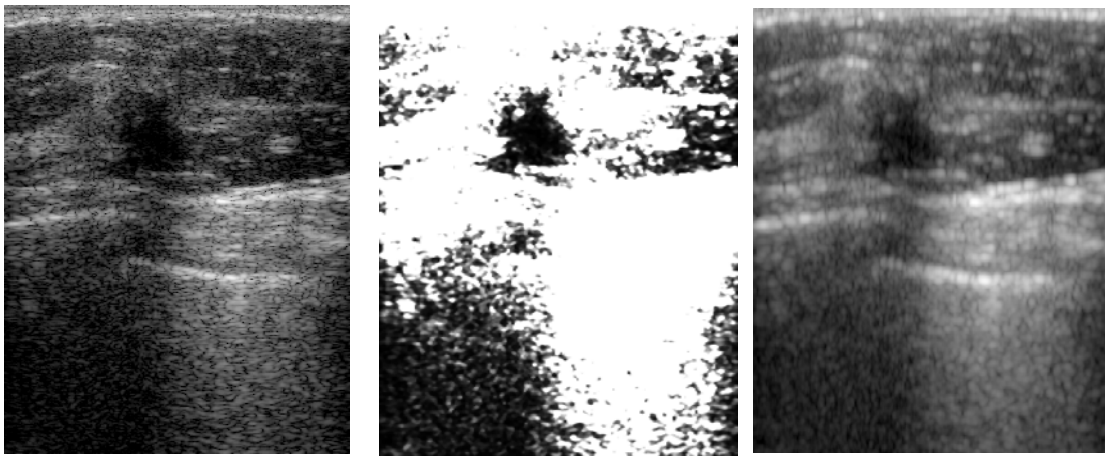

(a) (b) (c)

Figure 33 – Clinical case *#16* (ILC, cf. annex II): (a) B-mode image; (b) SPV parametric image (c) integrated backscatter (IBS) parametric image.

Table 3 – Average of metrics for the SPV and the IBS parametric images (detailed statistics for all patients are available in annex III). The ***W16*** window – a Hamming window of length 16 pixels and padded with 48 zeros – was used to compute both parametric images.

		$VC_{Bmode}(Y)$	**Corr (Bmode,Y)**	**$VI_{norm}(Bmode,Y)$**
Y = SPV	**mean**	**60.71**	**0.58**	**0.81**
	standard deviation	5.67	0.057	0.017
Y = IBS	**mean**	**-6.06**	**0.81**	**0.57**
	standard deviation	5.36	0.099	0.040

3.6.7. SPV Image versus SI Image

Some researchers have also proposed the use of the *spectral intercept* (SI) parameter from the dB-linearized spectrum as an estimate of the degree of echogenicity [58] [59]. The *spectral intercept* is the value of the regression line at zero frequency – cf. section 2.7 for details.

The *spectral intercept* estimate appeared poor when compared with SPV in generating parametric images with increased contrast along the mass boundaries. It is shown in the example in figure 34 that the mass boundary is less sharp for the SI parametric image. Table 4 also shows a decrease in contrast of SI image compared to the B-mode, $VC_{Bmode(SI)}$ = -12.7%. Moreover, B-mode and SI images appeared similar in terms of the structural information they provide – a lower variation in information content $VI_{norm(Bmode,SI)}$ = 0.71 and a higher correlation coefficient *Corr(Bmode,SI)* = 0.75 was observed when compared to the SPV image – see table 4. Detailed statistics for all patients are available in annex III.

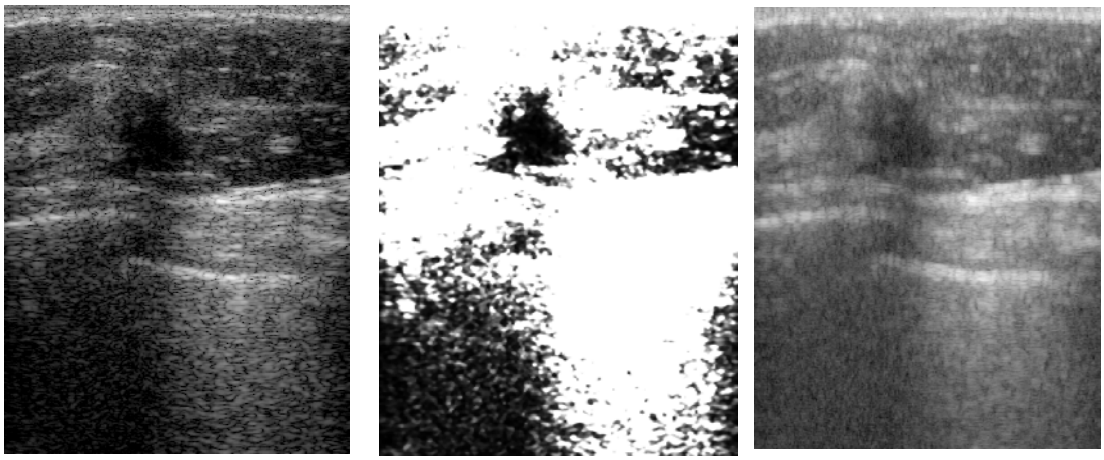

(a) (b) (c)

Figure 34 – Clinical case *#16* (ILC, cf. annex II): (a) B-mode image; (b) SPV parametric image (c) *spectral intercept* (SI) parametric image.

Table 4 – Average of metrics for the SPV and the SI parametric images (detailed statistics for all patients are available in annex III). The ***W16*** window – a Hamming window of length 16 pixels and padded with 48 zeros – was used to compute both parametric images.

		$VC_{Bmode}(Y)$	**Corr (Bmode,Y)**	**VI_{norm}(Bmode,Y)**
Y = SPV	**mean**	**60.71**	**0.58**	**0.81**
	standard deviation	5.67	0.057	0.017
Y = SI	**mean**	**-12.72**	**0.75**	**0.71**
	standard deviation	5.66	0.051	0.052

3.6.8. SPV Image versus B-mode-QTF

In order to investigate how the quadratic transformation function (QTF) – described in section 3.5 – in itself contributes to the contrast enhancement of the SPV images, the same transformation function was used to generate contrast-enhanced B-mode images (B-mode-QTF images).

The intensity values of the B-mode-QTF image were then computed by applying the following quadratic transformation function to the *envelope* of the raw I/Q data.

$$\text{B-mode-QTF} = \begin{cases} \left(\dfrac{envelope - min}{sp - min}\right)^2 & , envelope \leq sp \\ 1 & , envelope > sp \end{cases}$$

where *min* is the minimum value of the *envelope*; $sp = (Q_1 + Q_2)/2$ and Q_1, Q_2 is the first and second quartile of the histogram of the *envelope* values.

Figure 35 shows the B-mode, B-mode-QTF and SPV images for two clinical cases. Table 5 summarises the metrics for the SPV and B-mode-QTF images. Detailed statistics for all patients are available in annex III.

Similar levels of contrast enhancement were observed between the SPV and the B-mode-QTF images (cf. table 5 and figure 35). We can then conclude that the improvement in global contrast observed in the SPV images is mainly due to the quadratic transformation function (QTF) component of the SPV algorithm.

However, the SPV technique gives rise to less noisy images with sharper mass boundaries (see figure 35), which is mainly due to the fact that a better signal-to-noise ratio information is extracted from the spectrum to compute the SPV parameter (cf. annex V).

Moreover, between the B-mode-QTF and the B-mode images it was observed a higher correlation coefficient – *Corr(Bmode, BmodeQTF)* = 0.81 – and a lower variation in information content – VI_{norm}*(Bmode, BmodeQTF)* = 0.67, which indicates a higher similarity in terms of the structural information they provide (as opposed to the SPV and the B-mode images: *Corr(Bmode, SPV)* = 0.58 and VI_{norm}*(Bmode, SPV)* = 0.81).

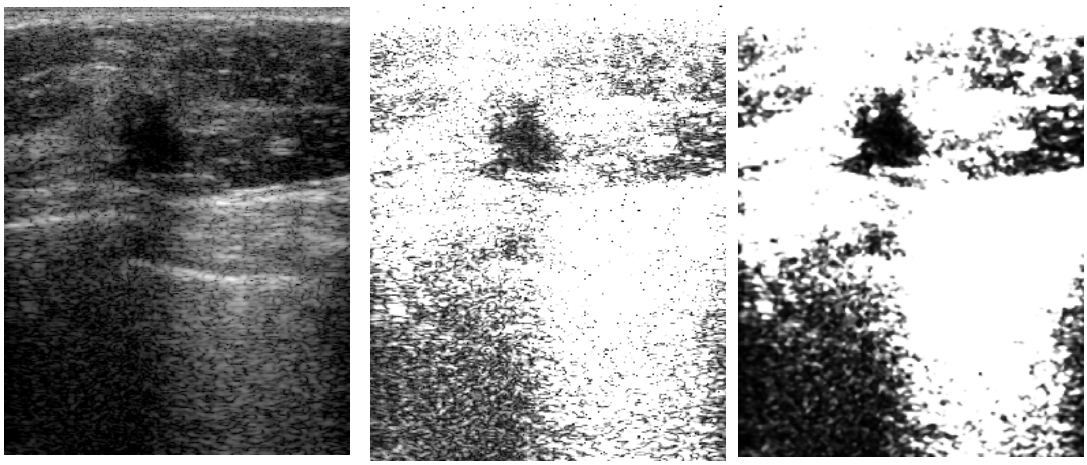

(a) (b) (c)

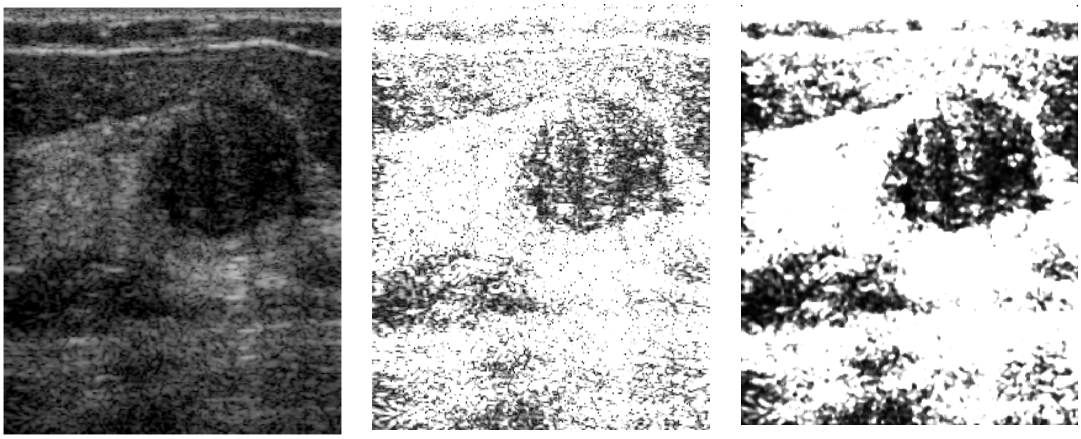

(d) (e) (f)

Figure 35 – B-mode image (left), B-mode-QTF image (centre) and SPV image (right) for clinical case *#16* (ILC, cf. annex II) – at the top – and for clinical case *#10* (ACC, cf. annex II) – at the bottom.

Table 5 – Average of metrics for the SPV and the B-mode-QTF images (detailed statistics for all patients are available in annex III). The ***W16*** window – a Hamming window of length 16 pixels and padded with 48 zeros – was used to compute the SPV images.

		$VC_{Bmode}(Y)$	Corr (Bmode,Y)	$VI_{norm}(Bmode,Y)$
Y = SPV	**mean**	**60.71**	**0.58**	**0.81**
	standard deviation	5.67	0.057	0.017
Y = B-mode-QTF	**mean**	**53.73**	**0.81**	**0.67**
	standard deviation	4.60	0.013	0.038

3.7. Clinical Pilot Study Results and Discussion

A 20-case pilot study was conducted to investigate if SPV images provide useful supplementary clinical information to B-mode images (cf. section 3.4.1 for patient and scanning details). A scale of five grades was used to classify the usefulness of the SPV parametric image in clinical practice. The grading system employed is shown in Table 6 together with some observations made by the radiologist (Dr. R. English, *MBChB, MRCP, FRCR, MA*) who conducted the assessment.

Note that the same raw I/Q data from the ultrasound machine was used to generate both the B-mode and the SPV parametric images. The findings from visual grading using this approach are summarised in figure 36.

According to figure 36, in 65% of the cases, the SPV image provided useful information not present in the B-mode image (increase in diagnostic confidence in at least one boundary). Furthermore, in 10% of the cases, the SPV image provided a better definition of the entire boundary (cf. figure 38(b) for an example).

The B-mode images and respective SPV parametric images for four clinical cases are shown in figure 38. A polychromatic colormap was used to display the SPV images as shown in figure 37 ‡‡. The blue pixels correspond to hyper-echoic regions, whereas the yellowish and reddish pixels correspond to pixels in a hypo-echoic region or a shadowed region (for instance, large reddish areas at the bottom of the image).

‡‡ **Displaying the spectral peak values in colour, makes it more convenient for the superposition of the LWSPV images onto the SPV images (as seen in the next chapter).**

Grade	Observations
0	Misleading information in comparison with B-mode.
1	No additional information in comparison with B-mode. No increase in diagnostic confidence.
2	Increase in diagnostic confidence in one or two boundaries.
3	Increase in diagnostic confidence in 3 boundaries.
4	Notable increase in confidence – better definition of the entire boundary.

Table 6 – Grading system used by the radiologist in the pilot study.

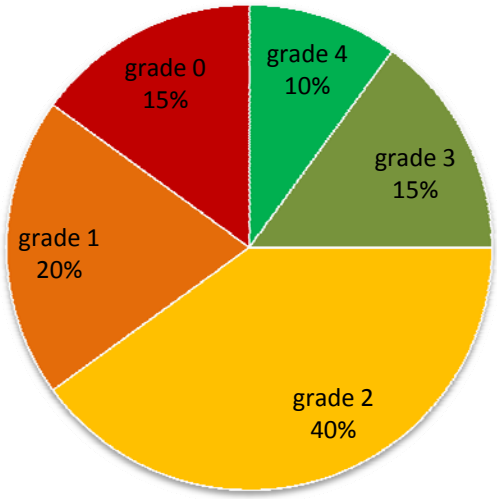

Figure 36 – Pilot study findings on 20 masses: visual grading using the approach described herein.

Shadowing affects SPV parametric images. Shadowed areas have low SPVs that are not related to hypo-echoic regions but are simply due to a lack of received information. If one or more structures between the target region and the transducer reflect or backscatter the majority of the emitted energy, preventing an insonification of that region, no significant echo will be received. For instance, in the clinical case in figure 38(f), although the top and lateral boundaries are well-defined, the bottom one is ambiguous and misleading due to shadowing (this case received grade 0). A change of the insonification angle can sometimes help to minimize this problem.

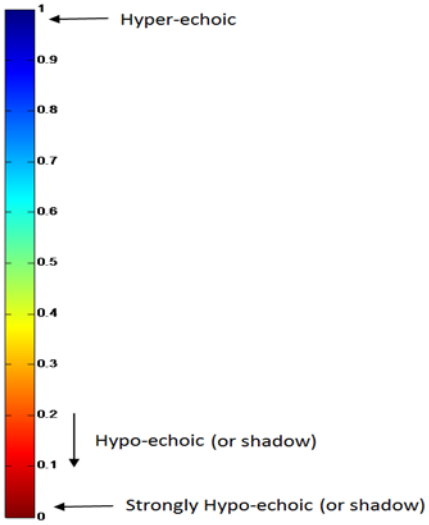

Figure 37 – Polychromatic colormap used to display the SPV images (blue pixels correspond to hyper-echoic regions; yellowish and reddish pixels represent hypo-echoic regions or shadowed regions).

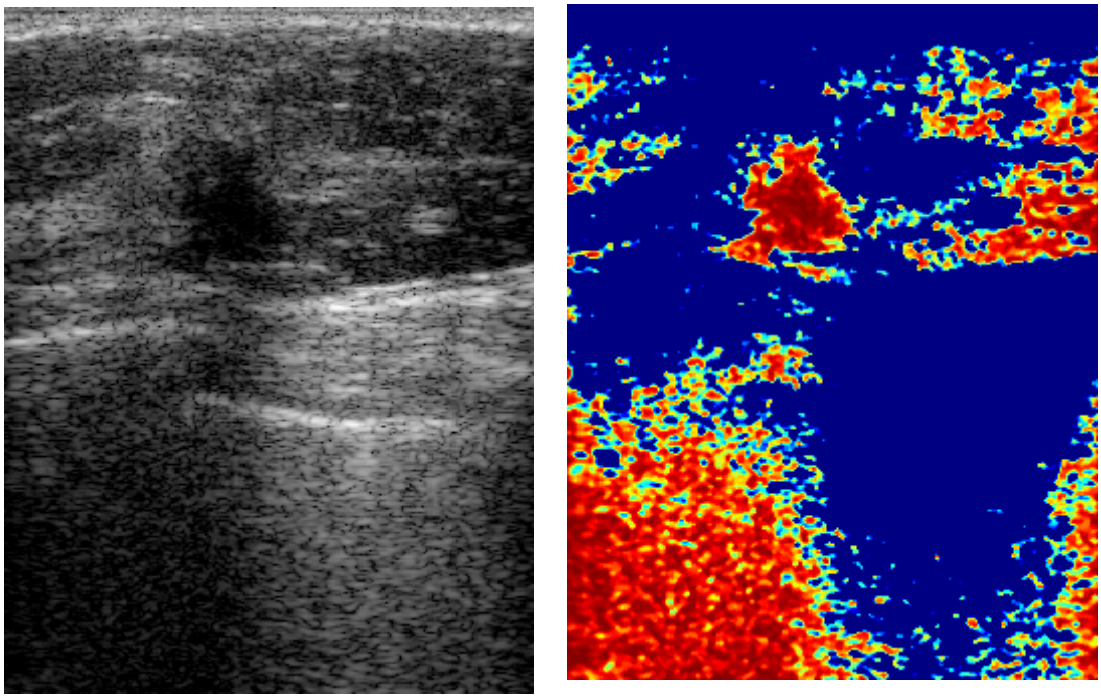

(a) (b)

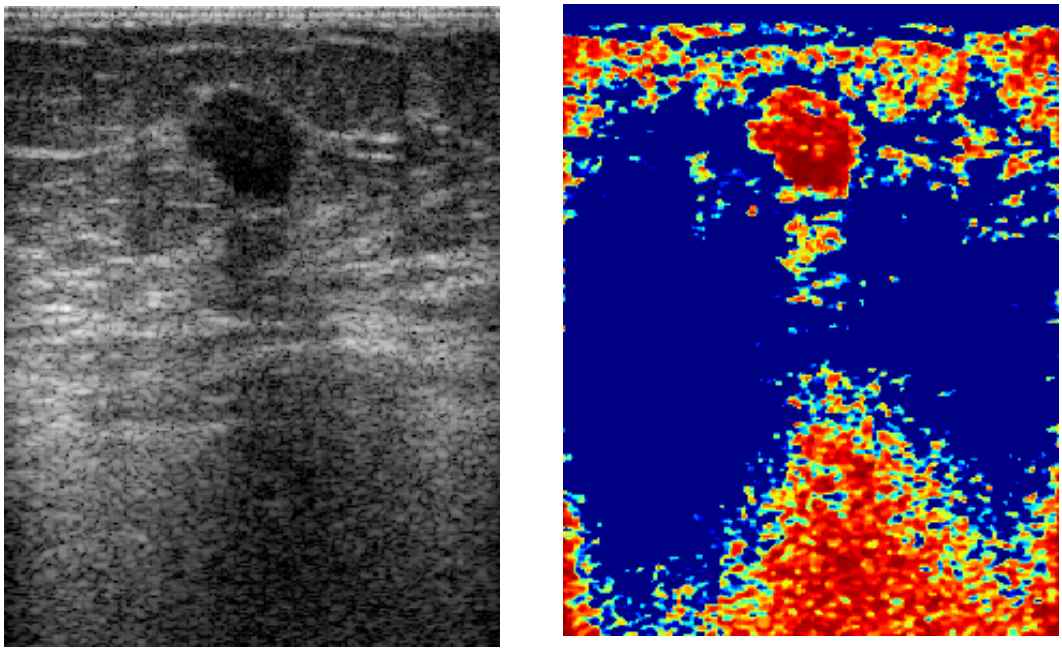

(c) (d)

Figure 38 – For four clinical cases: B-mode image (on the left-hand side) and respective SPV parametric image (on the right-hand side). (a), (b): clinical case *#16* (ILC, cf. annex II). (c), (d): clinical case *#1* (DCIS).

(e)

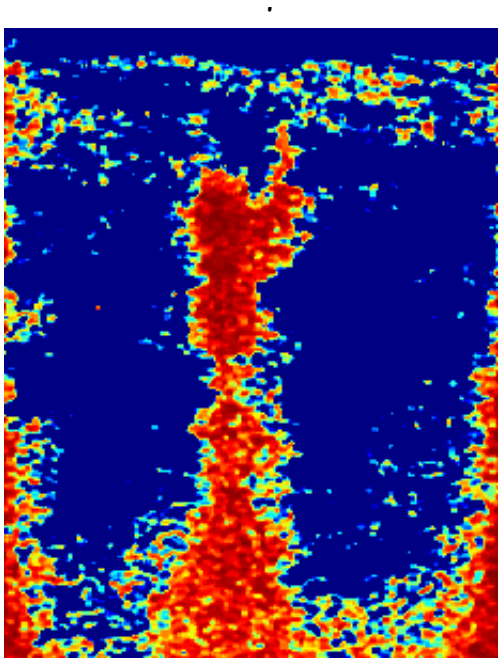

(f)

(g)

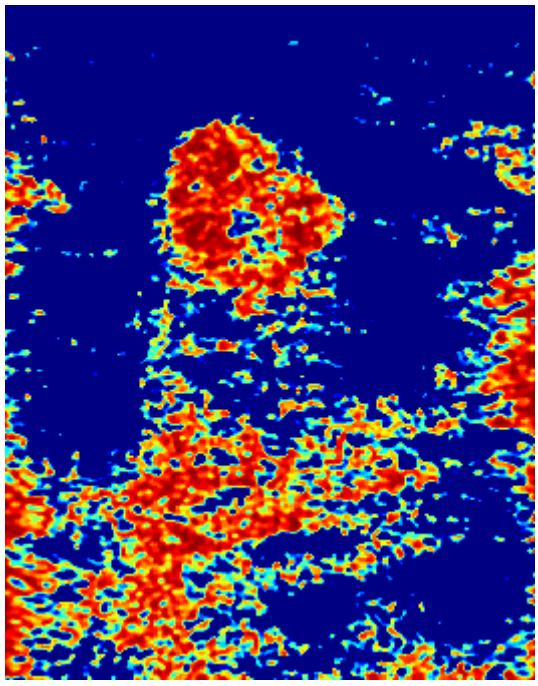

(h)

Figure 38 (*cont.*) – (e), (f): clinical case *#11* (DCIS+IDC). (g), (h): clinical case *#12* (IDC).

3.8. Conclusion

In this chapter, we have proposed a new method of processing the backscattered breast ultrasound signals in the frequency domain (Fourier spectral analysis) to generate parametric images where the visibility of breast mass boundaries is improved. This method is based on an adaptive narrow-band filtering about the frequency at which the intensity received is maximum (spectral peak). An improvement in boundary conspicuity and contrast was observed in clinical data. The key steps of the SPV algorithm are summarised in figure 12.

The ultrasound images generated by four different estimates of the degree of echogenicity were quantitatively compared: the log-compressed envelope of the RF data (B-mode imaging); the integrated backscatter coefficient (IBS imaging); the spectral intercept of the dB-linearized spectrum (SI imaging) and the spectral peak value (SPV imaging). Three metrics were used to compare and contrast those types of image: two intensity-based metrics – variation of contrast and correlation coefficient – and one entropy-based metric – variation of information content. The SPV image was observed to be the most appropriate to improve the visibility of breast mass boundaries.

Different settings for the SPV parametric image in terms of saturation point, *sp*, and window size, *L*, were also investigated. A $sp = (Q_1+Q_2)/2$ was found to be the best option among five investigated options (cf. section 3.5). $L = 16$ was found to be the best option in comparison to 32, 64 and 128 (cf. section 3.6). We observed that a larger window size gave rise to more blurred SPV parametric images because the

same window might comprise different types of tissue, leading to a superposition of dissimilar properties in the same spectrum.

Furthermore, a 20-case clinical pilot study showed that the SPV parametric image added useful information to the B-mode image for clinical assessment in 65% of the cases.

Nonetheless, it was observed that the SPV algorithm was sensitive to shadowing, which particularly affected the correct detection of the bottom boundary of the mass (for an example, cf. figure 38(e)-(f)). In fact, in the clinical cases where the bottom boundary was challenging to detect on the B-mode image, it remained challenging to detect on the SPV image. In the next chapter we develop an algorithm to tackle the shadowing problem.

4. LWSPV Parametric Images

In this chapter, we explore the use of the spectral information in a local context in order to tackle the shadowing problem present in the SPV parametric images.

4.1. LWSPV Computation and Meaning

In areas affected by acoustic shadowing, a low SPV does not necessarily mean an area with a low degree of echogenicity. As discussed in chapter 4, if one or more structures between the target region and the transducer reflect or backscatter the majority of the emitted energy, preventing an insonification of that region, a much attenuated echo will be received. However, the region just above will also suffer a similar attenuation. Thus, although the area under analysis may exhibit a low SPV in a global context (i.e. compared to all SPVs across the scan plane), it may exhibit a high SPV when compared only with the neighbourhood above, where the ultrasound echoes were obtained under similar conditions. We then propose the computation of a parameter for each pixel across the scan plane which reflects the local weight of its spectral peak value within a specified neighbourhood. This parameter we call the Local Weight of the Spectral Peak Value (LWSPV).

For a given pixel ***P*** located at *(p, sl)* – see figure 39 – its neighbourhood is defined herein as the *R* pixels on the same scan line *sl* between the positions *p-8-R* and *p-8*. Note that the neighbourhood does not encompass the seven pixels before pixel ***P*** because their spectral peak values are strongly correlated due to the window length used during the computation of the spectrum (cf. chapter 3).

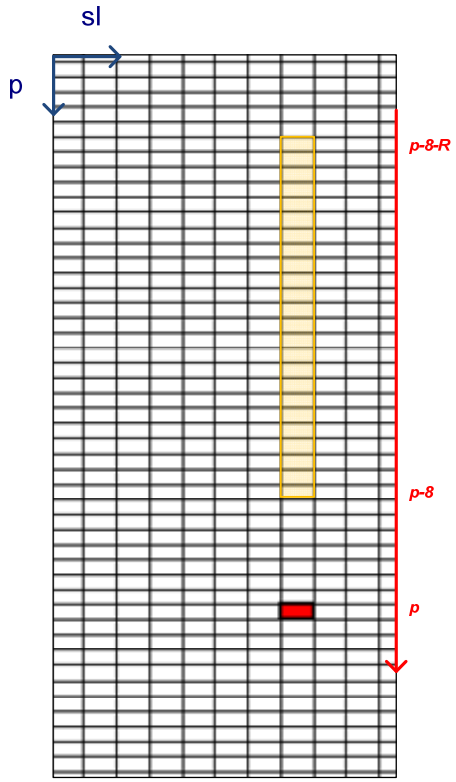

Figure 39 – Considering that we are calculating the LWSPV for pixel ***P*** in red, the respective neighbourhood is highlighted in yellow.

The Local Weight of the Spectral Peak Value (LWSPV) for a given pixel located at *(p, sl)* is then calculated as follows,

$$LWSPV(p, sl) = \frac{SPV_{(p,sl)}}{max_{i=p-8-R}^{p-8} \{SPV_{(i,sl)}\}}$$

In words, the LWSPV of a certain pixel is the ratio of its SPV to the maximum SPV within its neighbourhood.

However, in practice, to reduce the effect of potential outliers, a weighted average of the three largest spectral peak values within the neighbourhood was used instead of only the maximum value, as described next.

Consider that SPV_{m1} is the largest spectral peak value within the neighbourhood, SPV_{m2} is the second largest value and SPV_{m3} is the third largest value (see an example in figure 40). Then, the LWSPV is given by

$$LWSPV(p, sl) = \frac{SPV_{(p,sl)}}{\left(\frac{2 * SPV_{m1} + SPV_{m2} + SPV_{m3}}{4}\right)}$$

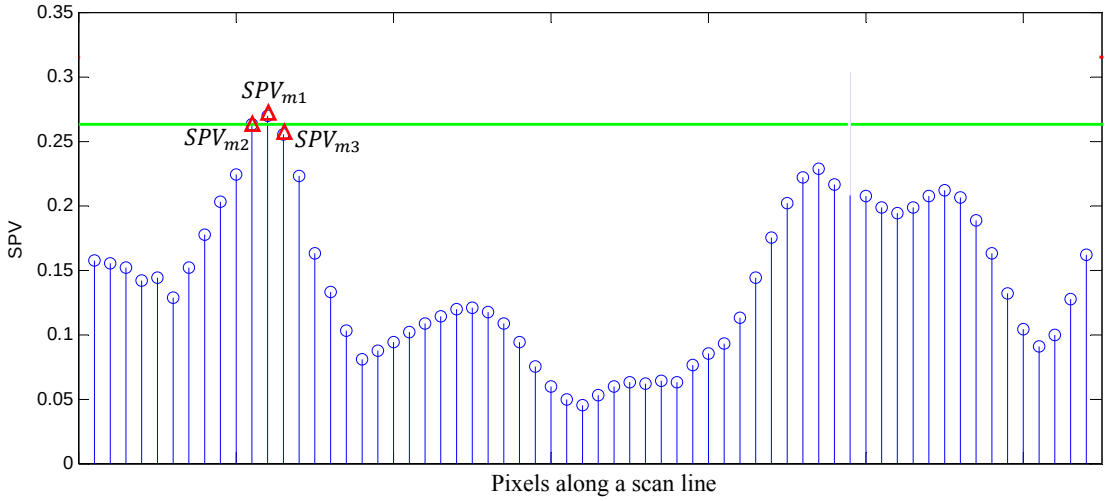

Figure 40 – Example neighbourhood with 64 pixels (R = 64). The green line indicates the weighted average of the three largest spectral peak values (red triangles).

The parameter R defines the size of the neighbourhood. The value of R used in our experiments is 64, which was found to give good results during the pilot study discussed later. In conversations with the radiologist, it became clear the importance of detecting Cooper's ligaments (particularly the shadowed and porterior-to-mass Cooper's ligaments) for the correct assessment of breast masses. In [12] it is reported that Cooper's ligament thickness usually varies between 1 and 3 millimetres.

Knowing that the pixel size along the axial direction is 0.048 millimetres for our images[§§], a value of $R = 64$ pixels corresponds to a size of $64 \times 0.048 = 3.072$ millimetres, which is long enough (in cross-section) to resolve Cooper's ligaments.

Lastly, in order to enhance contrast and normalize the LWSPVs onto the interval 0 to 1, the following linear transformation function was used.

$$LWSPV_{out} = \begin{cases} 0 & , 0 \leq LWSPV_{in} < th1 \\ \left(\frac{1}{th2 - th1}\right) LWSPV_{in} - \left(\frac{th1}{th2 - th1}\right) & , th1 \leq LWSPV_{in} \leq th2 \\ 1 & , LWSPV_{in} > th2 \end{cases}$$

We wanted to select all the pixels whose SPV is greater than the maximum SPV within its neighbourhood (in other words, we wanted to select all pixels more echoic than its neighbourhood). Then, threshold *th2* was set to 1.

On the other hand, threshold *th1* was set to 0.5 to discard all the pixels whose SPV is less than half the maximum SPV within its neighbourhood (cf. figure 41 for a practical note).

Substituting for *th1* and *th2* led to the following piecewise linear transformation function,

$$LWSPV_{out} = \begin{cases} 0 & , 0 \leq LWSPV_{in} < 0.5 \\ 2 \cdot LWSPV_{in} - 1 & , 0.5 \leq LWSPV_{in} \leq 1 \\ 1 & , LWSPV_{in} > 1 \end{cases}$$

[§§] $Pixel\ size\ along\ the\ axial\ direction = \frac{depth}{number\ of\ pixels} = \frac{50mm}{1040} \approx 0.048mm$

The final LWSPV parametric image is then obtained after employing a *7-by-7* median filter. This step has the purpose of reducing outliers and making the white regions more continuous, removing small discontinuities and holes within it.

A high-level block diagram of the LWSPV algorithm is depicted in figure 42.

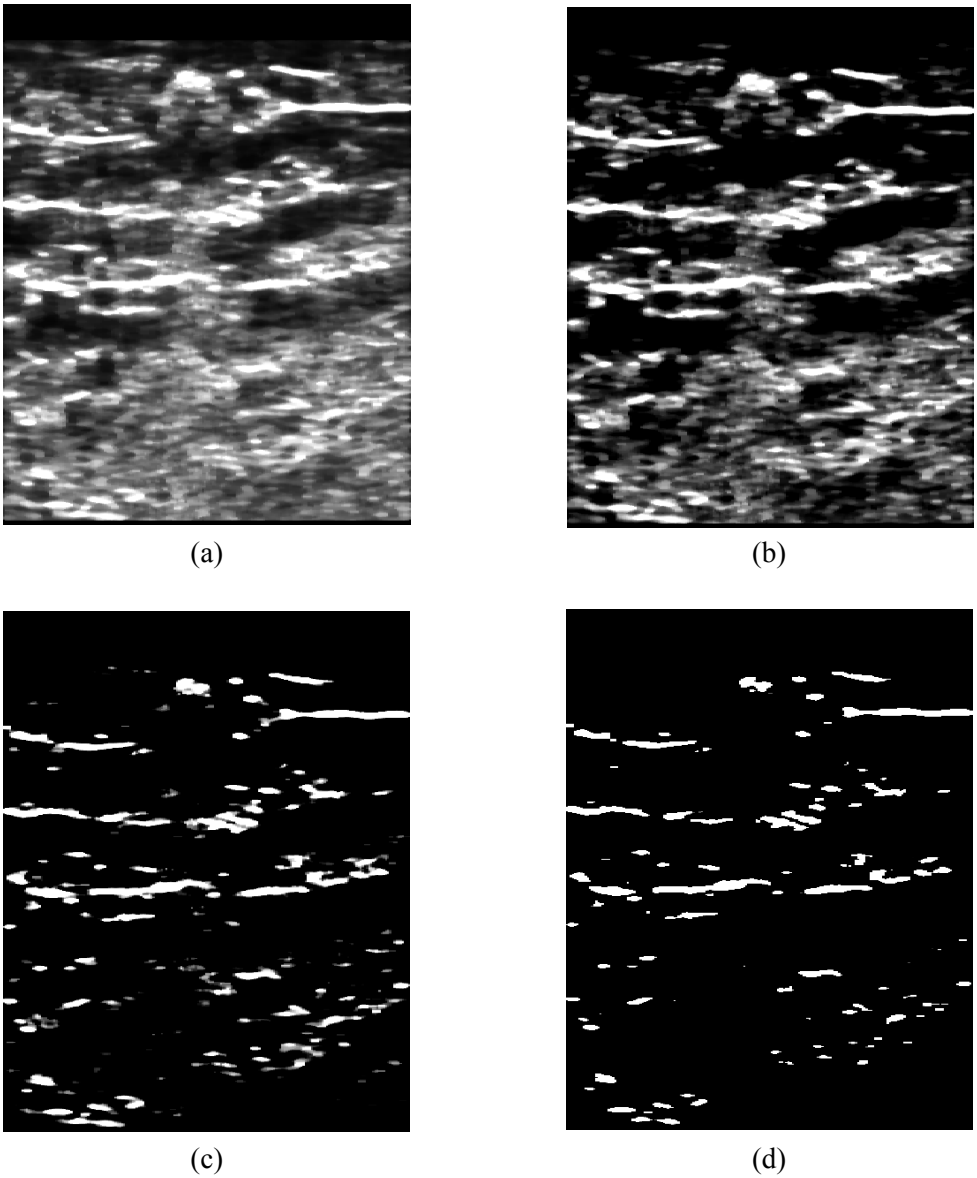

(a) (b)

(c) (d)

Figure 41 – LWSPV images for the clinical case *#11* at *th2* = 1 and *th1* = 0 (a) ; 0.25 (b) ; 0.5 (c) and 0.75 (d). Note that, in practice, the smaller the value of *th1*, the greater the amount of minor anatomical structures and acoustic artefacts appearing on the LWSPV image.

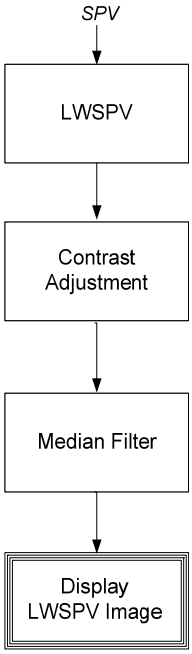

Figure 42 – High-level block diagram of the LWSPV algorithm.

4.2. Clinical Case Examples and Discussion

To better understand the practical meaning of the LWSPV, let us take the clinical cases in figure 43 as an example. It is a typical case where the mass and posterior shadow constitute a continuous darkish region on the B-mode image (reddish region on the SPV image), making the bottom boundary imperceptible. From histopathology, we know that the mass nestles on the Cooper's ligament ***a***. The schematic in figure 43 (e) depicts the location of the malignant mass and the Cooper's ligament ***a*** and ***b***.

Comparing the SPV intensity profile (figure 43 (c)) with the LWSPV intensity profile (figure 43 (d)) along the scan line *sl = 88*, although the SPV intensity profile exhibits low values after pixel *p = 400* (caused mainly by the shadowing phenomenon described in the previous chapter), the LWSPV intensity profile increases just after *p = 400*. The LWSPV behaviour indicates that locally there is a significant increase in the SPV values, suggesting the existence of a coarse discontinuity in this region. In fact, it corresponds to the location of the Cooper's ligament ***a*** (cf. figure 43 (e))[***]. The following strong spike on the LWSPV intensity profile occurs around *p = 530*, where the top of the Cooper's ligament ***b*** is located (cf. figure 43 (e)).

Figure 44 (a) and (b) shows the LWSPV image before and after median filter, respectively.

Finally, in figure 44 (d), the information from the LWSPV and SPV algorithm is combined, i.e. the LWSPV parametric image is superimposed (by addition) onto the SPV parametric image, to generate a final SPV+LWSPV parametric image.

[***] Please note that we do not know the exact location of the Cooper's ligaments (because the histology images were not available). However, the histopathology report, which was analysed by the radiologist, mentions that the malignant mass sits on a Cooper's ligament.

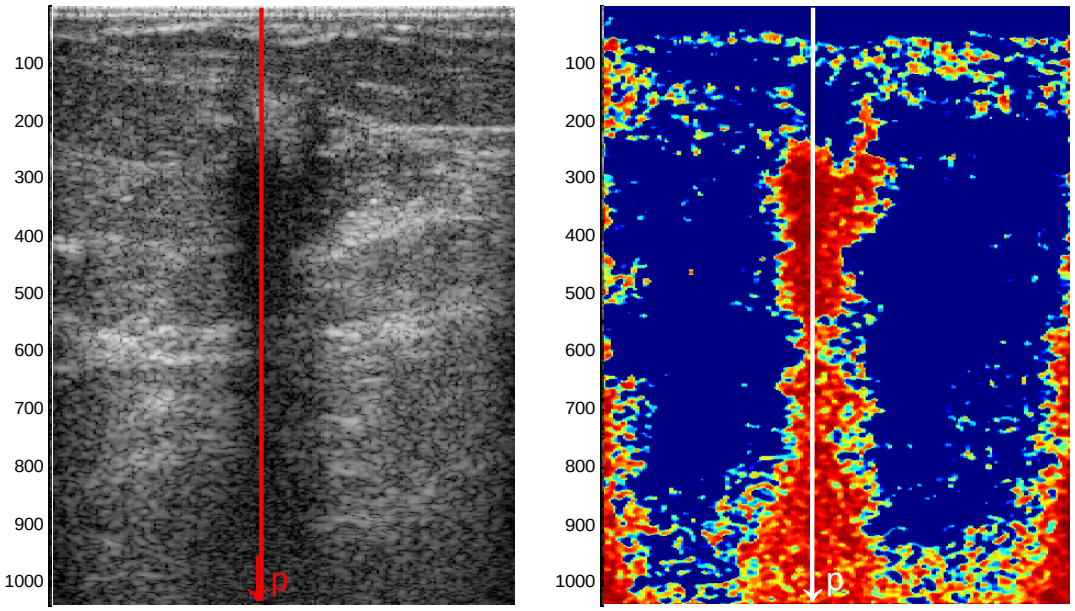

(a) (b)

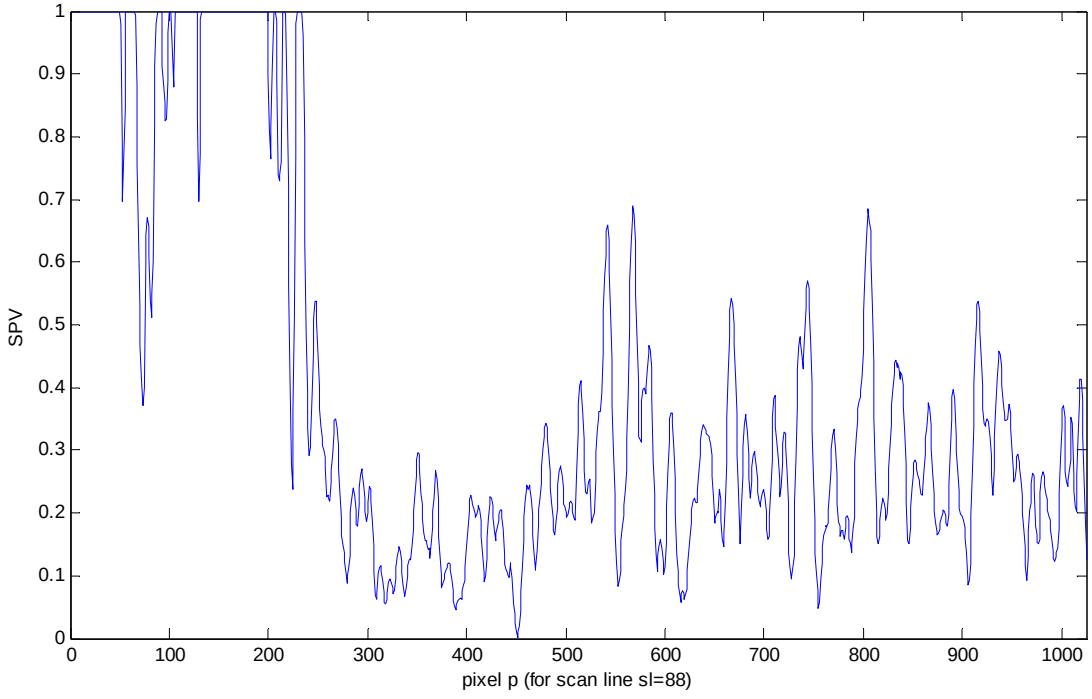

(c)

Figure 43 – Clinical case *#11* (DCIS+IDC, cf. annex II): (a), (b) B-mode and SPV image, respectively (the scan line 88 is marked in red and white); (c) SPV intensity profile for the pixels along scan line 88.

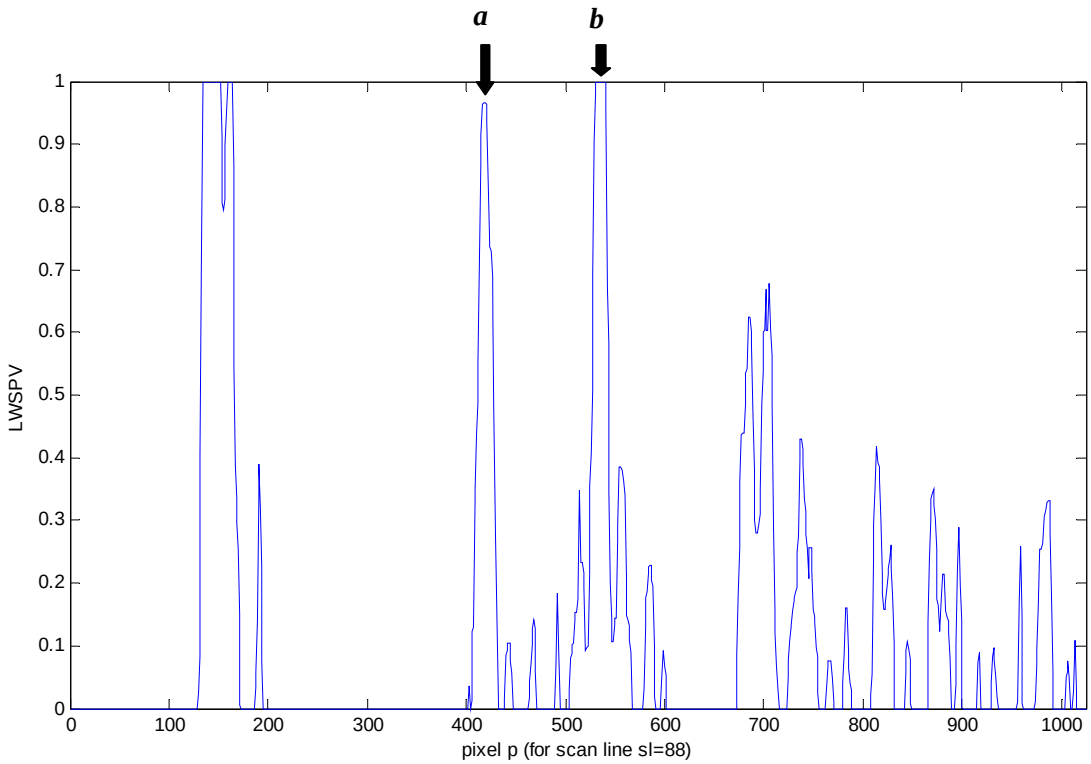

(d)

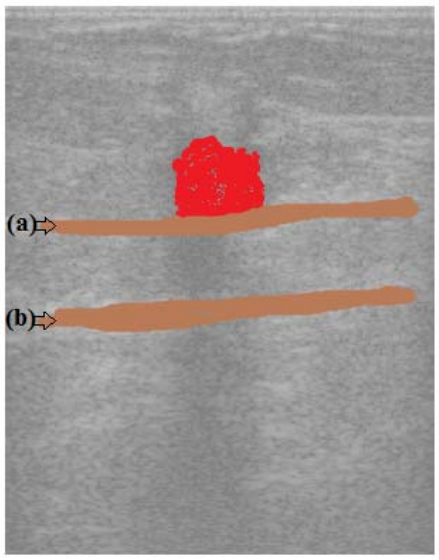

(e)

Figure 43 (*cont.*) – (d) LWSPV intensity profile for the pixels along scan line 88; (e) schematic depicting the location of the mass and the Cooper's ligament ***a*** and ***b***. (This information was provided by a radiologist after analysing the histopathology report).

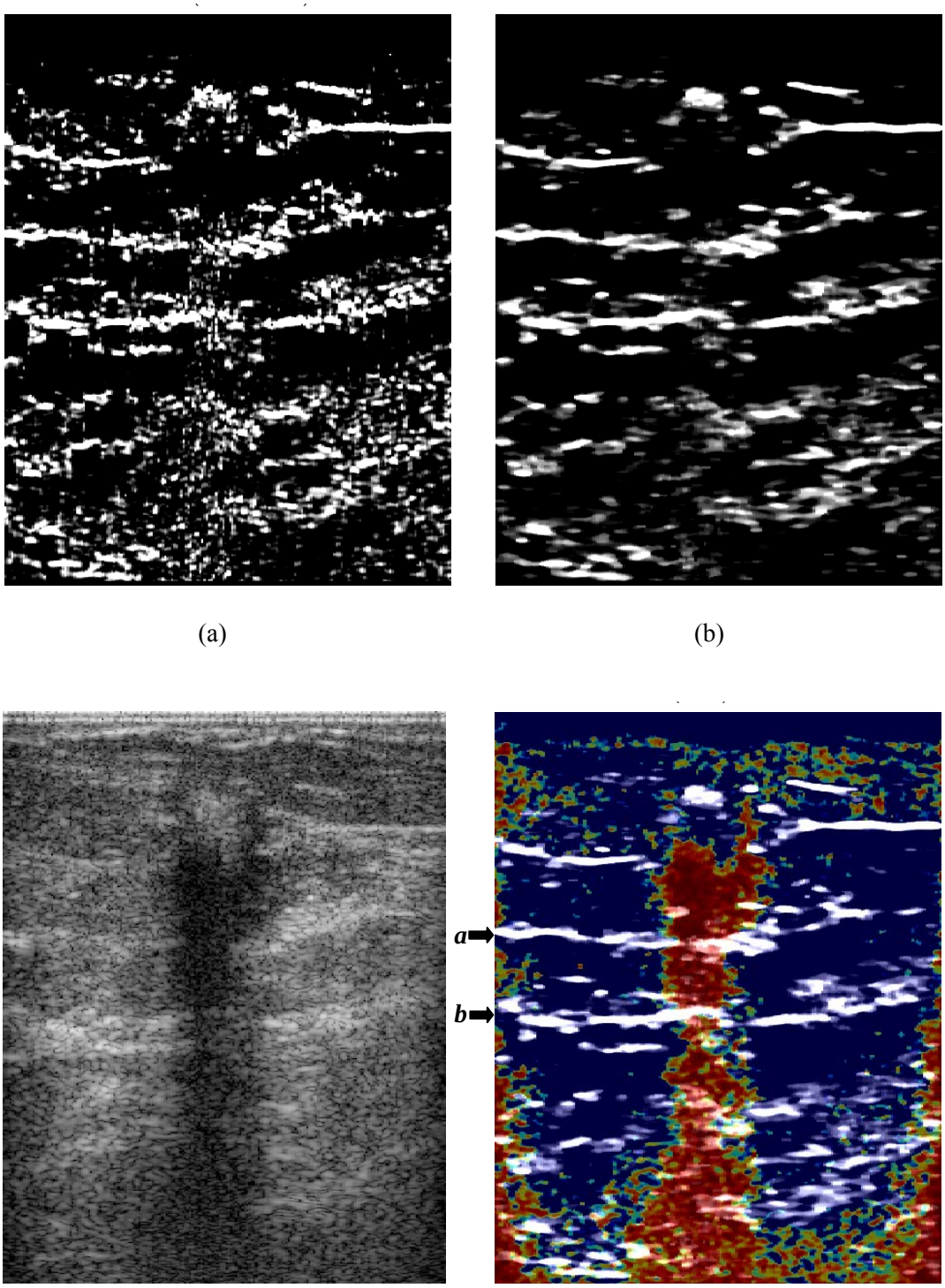

Figure 44 – Clinical case *#11* (DCIS+IDC, cf. annex II): (a), (b) LWSPV images before and after the median filter, respectively; (c) B-mode image; (d) superposition of the LWSPV image onto the SPV image. Note the detection of the Cooper's ligaments ***a*** and ***b***.

Let us know analyse a second case (see figure 45). Once again, the bottom boundary is imperceptible on both the B-mode and SPV images.

Looking at figure 45 (c), between $p \approx 230$ and $p \approx 600$, the SPV intensity profile fluctuates at low values (always lower than 0.3). However, from the LWSPV intensity profile (cf. figure 45 (d)), it is clear a spike appears just before $p = 400$. It indicates a significant local increase in the SPVs in this region. In fact, we know from histopathology that the bottom boundary (***bb***) of the mass is located in this region (cf. figure 45 (e)).

Figure 46 (a) and (b) shows the LWSPV image before and after applying a median filter, respectively.

Lastly, in figure 46 (d), the LWSPV image is superimposed onto the SPV image. From this image, we can see a relatively well-defined white strip along the bottom boundary (pointed out by the yellow arrows).

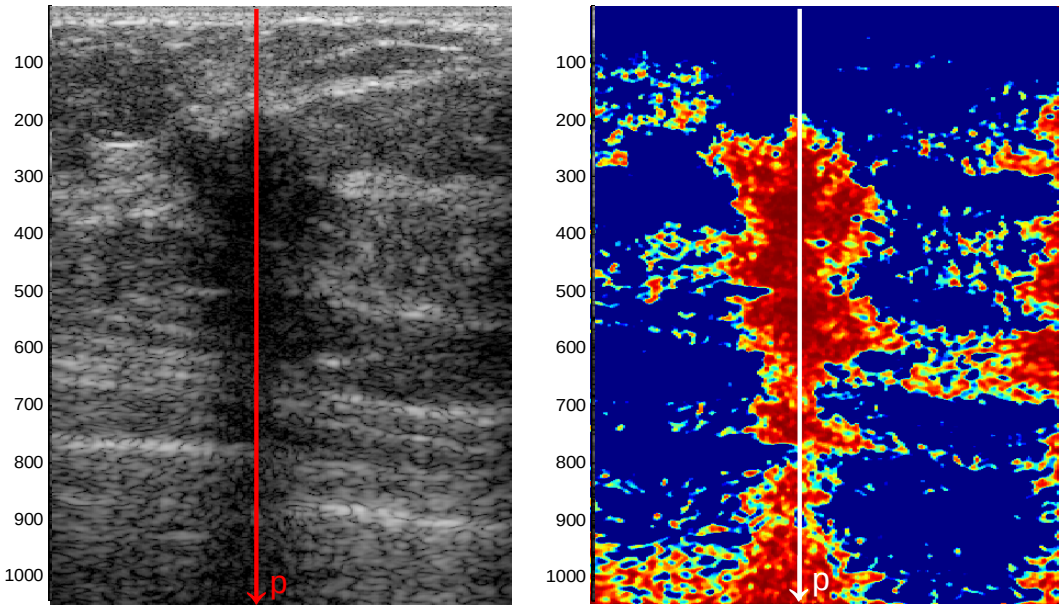

(a) (b)

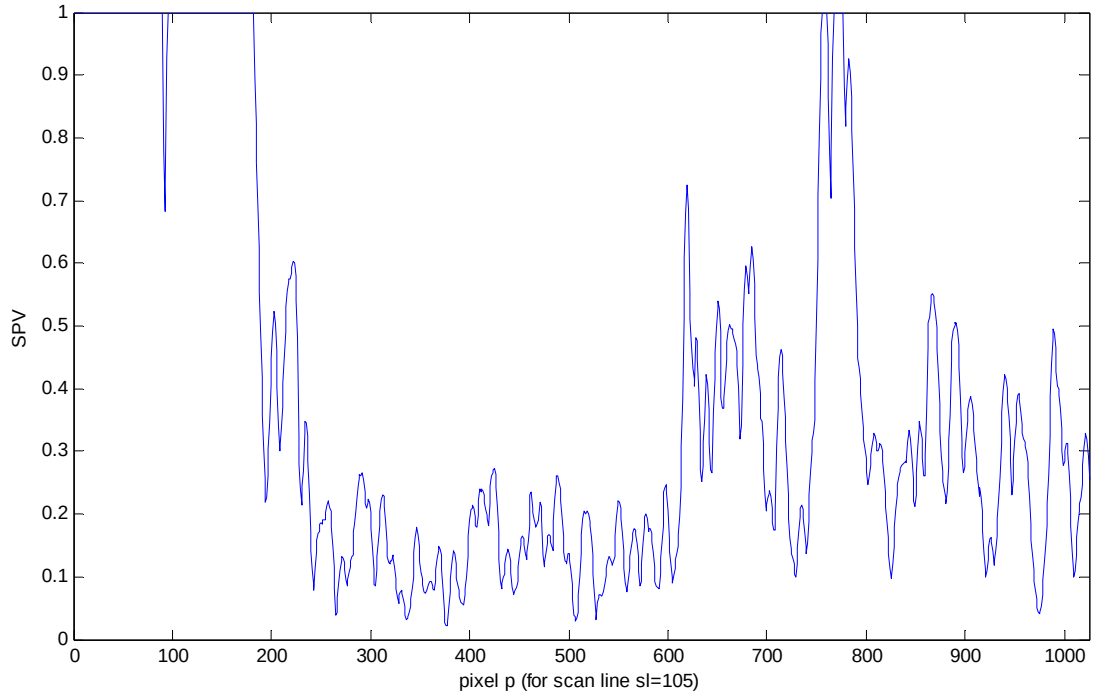

(c)

Figure 45 – Clinical case *#2* (IDC+ILC, cf. annex II): (a), (b) B-mode and SPV image, respectively (the scan line 105 is marked in red and white); (c) SPV intensity profile for the pixels along scan line 105.

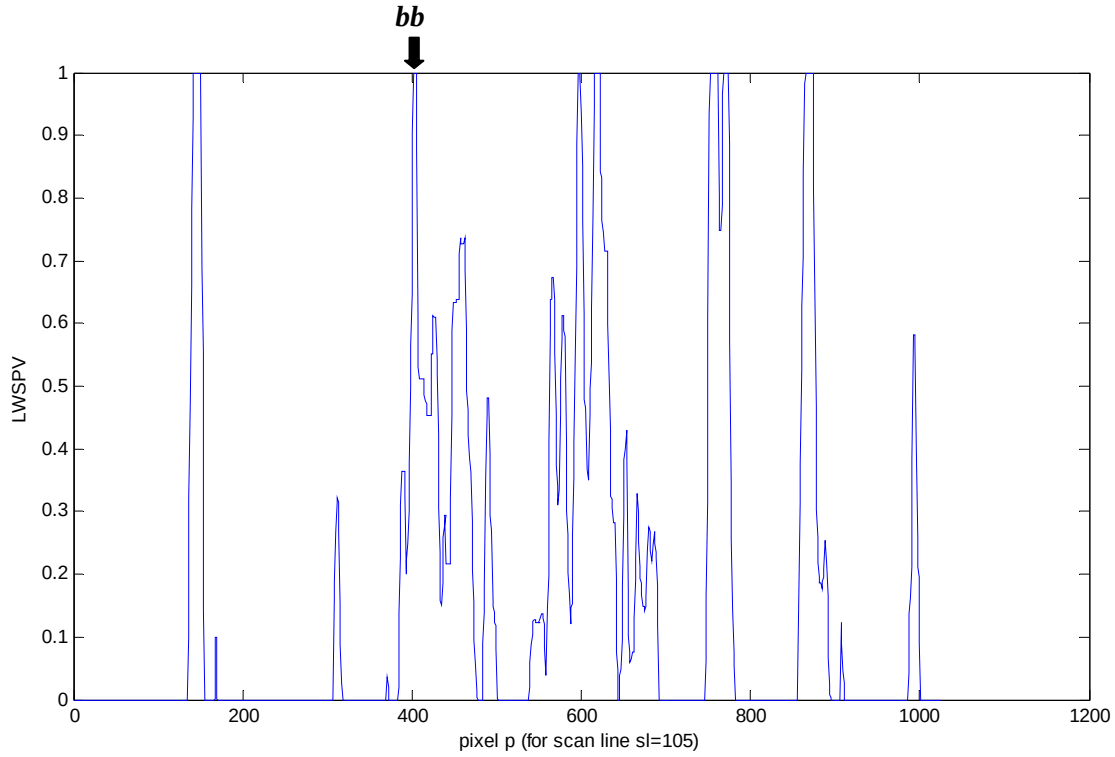

(d)

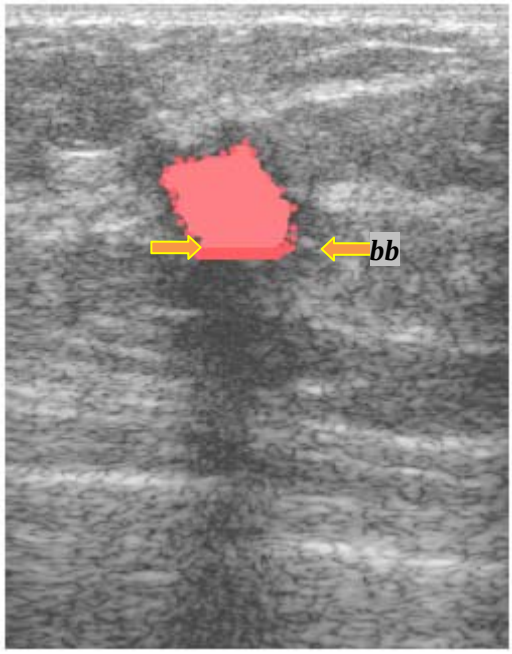

(e)

Figure 45 (*cont.*) – (d) LWSPV intensity profile for the pixels along scan line 105; (e) schematic depicting the location of the mass The core of the malignant mass is painted in pale red. The yellow arrows point to the bottom boundary (***bb***). (This information was provided by a radiologist after analysing the histopathology report).

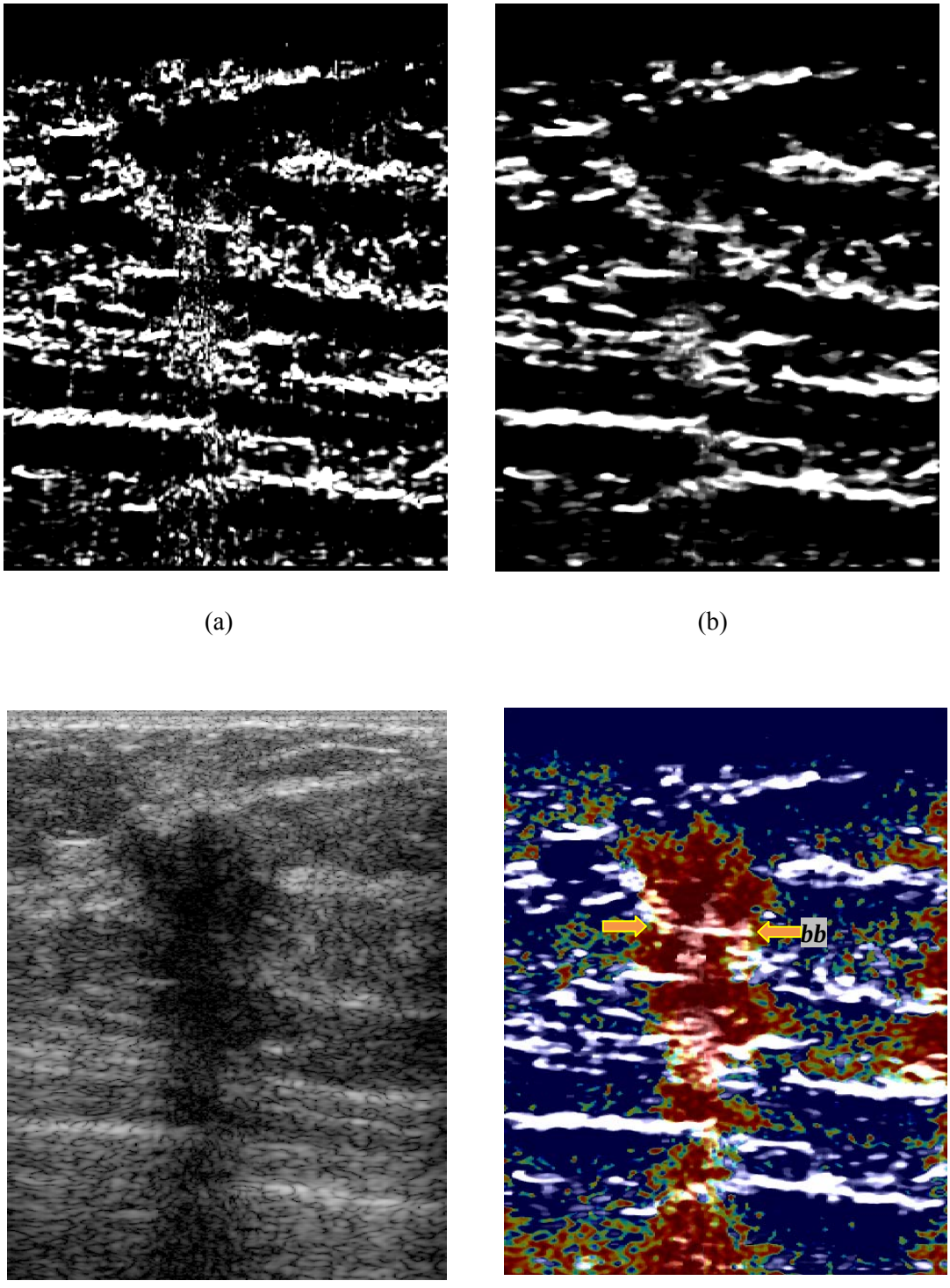

(a) (b)

(c) (d)

Figure 46 – Clinical case *#2* (IDC+ILC, cf. annex II): (a), (b) LWSPV images before and after the median filter, respectively; (c) B-mode image; (d) superposition of the LWSPV image onto the SPV image. Note the detection of the bottom boundary (***bb***) of the mass.

The clinical case in figure 47 is another situation where the mass nestles on a Cooper's ligament and the bottom boundary is not detected during SPV-image-generation stage. Nevertheless, it is correctly detected by the LWSPV algorithm.

A further example to show how conventional B-mode imaging can miss important boundaries and structures is presented in annex VI – LWSPV image of a cherry phantom.

In figure 48, we present a clinical case where the mass was correctly detected during the SPV-image-generation stage. The white area along the bottom of the mass on the LWSPV image reinforces the location of the boundary.

To summarise, in the LWSPV image, the white regions correspond to hyper-echoic structures (for example, fibrous tissue such as Cooper's ligaments), some of which were shadowed during the ultrasound image acquisition process.

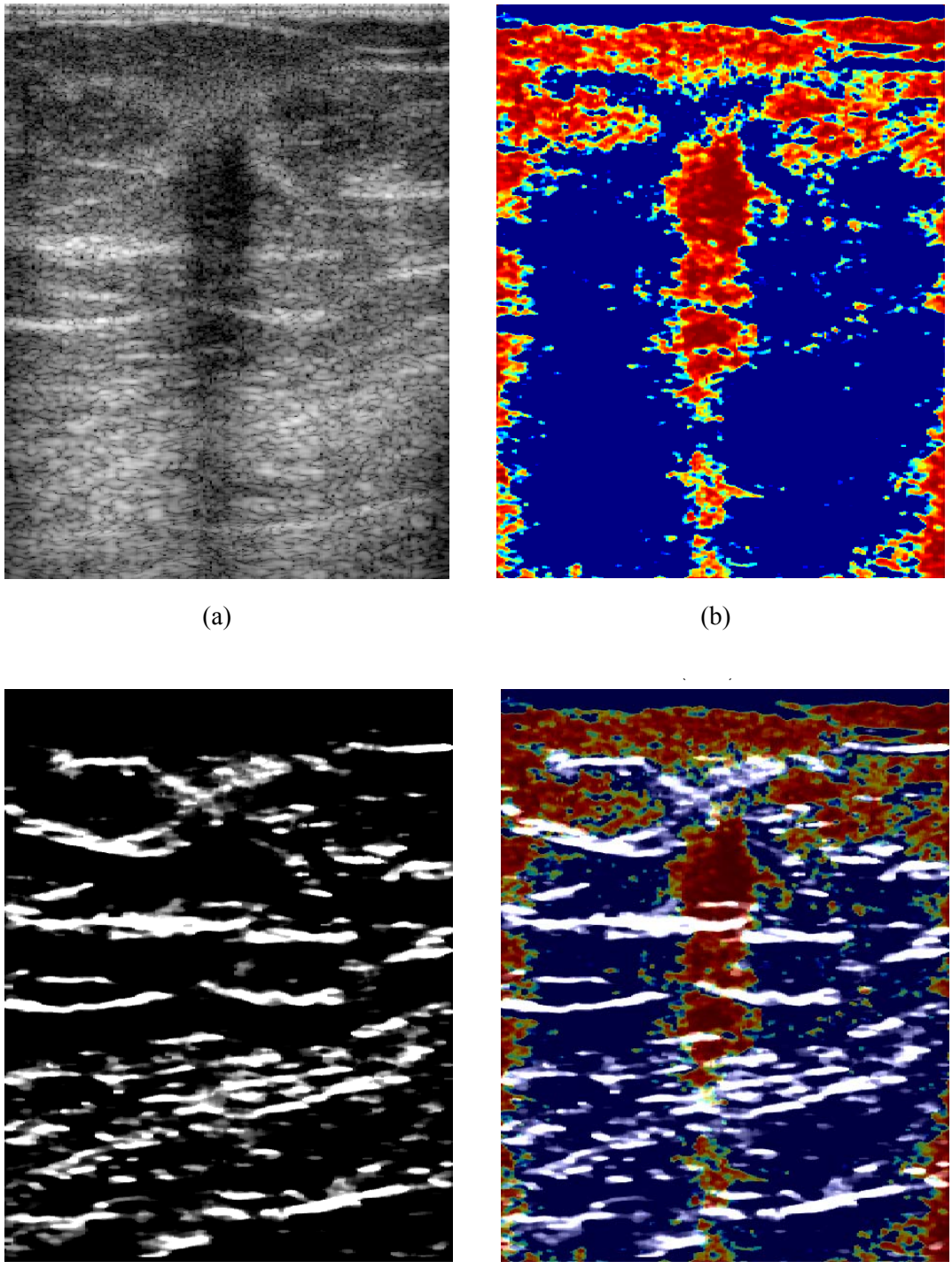

Figure 47 – Clinical case *#13* (ILC, cf. annex II): (a) B-mode, (b) SPV, (c) LWSPV, (d) SPV+LWSPV images.

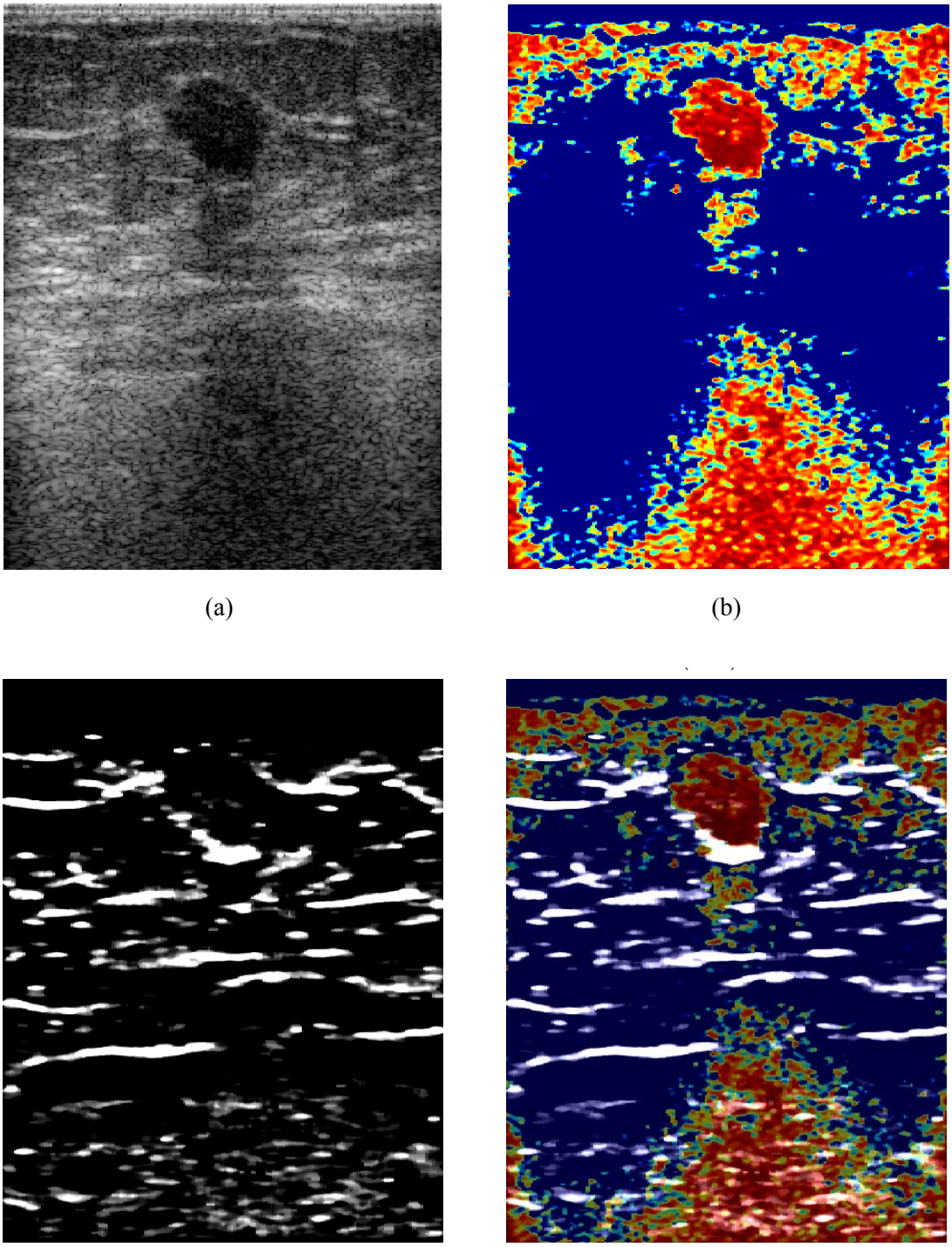

Figure 48 – Clinical case *#1* (DCIS, cf. annex II): (a) B-mode, (b) SPV, (c) LWSPV, (d) SPV+LWSPV images.

4.2.1. B-mode-QTF intensity values as the input of the LWSPV Algorithm

In section 3.6.8, the SPV and B-mode-QTF images were compared. Next, we investigate the use of the B-mode-QTF intensity values as the input of the LWSPV algorithm instead of the SPV intensity values.

We reported in section 3.6.8 a higher correlation coefficient, *Corr(Bmode, BmodeQTF)* = 0.81, and a lower variation in information content, VI_{norm}*(Bmode, BmodeQTF)* = 0.67, between B-mode-QTF and B-mode images, which indicates a higher similarity in terms of the structural information they provide (as opposed to SPV and B-mode images: *Corr(Bmode, SPV)* = 0.58 and VI_{norm}*(Bmode, SPV)* = 0.81). Those facts may also explain why the shadowed Cooper's ligaments just under the mass were not recovered when we used the B-mode-QTF intensity values as the input of the LWSPV algorithm instead of the SPV intensity values. See two clinical cases in figure 49 (note that the same polychromatic colormap was used to generate all parametric images displayed in this and previous chapter).

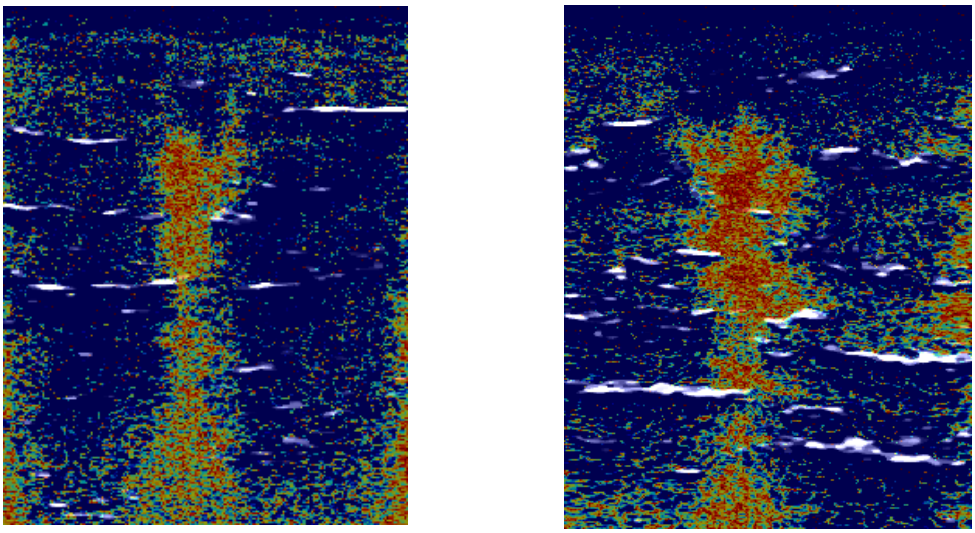

(a) (b)

Figure 49 – B-mode-QTF+LWSPV parametric images using the B-mode-QTF intensity values as the input of the LWSPV algorithm instead of the SPV intensity values: (a) clinical case #11 – cf. figure 43 for details. The corresponding SPV+LWSPV parametric image is shown in figure 44(d); (b) clinical case #2 – cf. figure 45 for details. The corresponding SPV+LWSPV parametric image is shown in figure 46(d).

4.3. Pilot Study Results and Discussion

In this section we present results from a 20-case pilot study conducted to assess if the combined SPV+LWSPV parametric images added useful information to the B-mode images in terms of increasing the diagnostic confidence in identifying the mass boundaries. We also compared these results with those of chapter 4 to see how better the results would be by adding the LWSPV algorithm. Note that for both pilot studies the same clinical cases were used.

The grading system employed is the same as used in chapter 4 (shown again in Table 7 for convenience). The findings from visual grading using this approach are summarised in figure 50.

For each clinical case, the final diagnostic decision was known from histopathology. Moreover, the same raw data from the ultrasound machine was used to generate all images (B-mode, SPV and LWSPV).

According to figure 50, the SPV+LWSPV parametric image added useful information to the B-mode image for clinical assessment in 85% of the cases (increase in diagnostic confidence in at least one boundary). Furthermore, in 35% of the cases, the SPV+LWSPV parametric image provided a notable increase in diagnostic confidence (better definition of the entire boundary).

It is also clear that the LWSPV parametric image added value relative to the SPV parametric image. Specifically, comparing this second pilot study with the one presented in chapter 4, the percentage of clinical cases with an increase in diagnostic confidence in at least one boundary rose by 20% from 65% to 85%. Furthermore, the percentage of clinical cases with a better definition of the entire boundary was observed to increase from 10% to 35%.

Grade	Observations
0	Misleading information in comparison with B-mode.
1	No additional information in comparison with B-mode. No increase in diagnostic confidence.
2	Increase in diagnostic confidence in one or two boundaries.
3	Increase in diagnostic confidence in 3 boundaries.
4	Notable increase in confidence – better definition of the entire boundary.

Table 7 – Grading system used by the radiologist in the pilot studies.

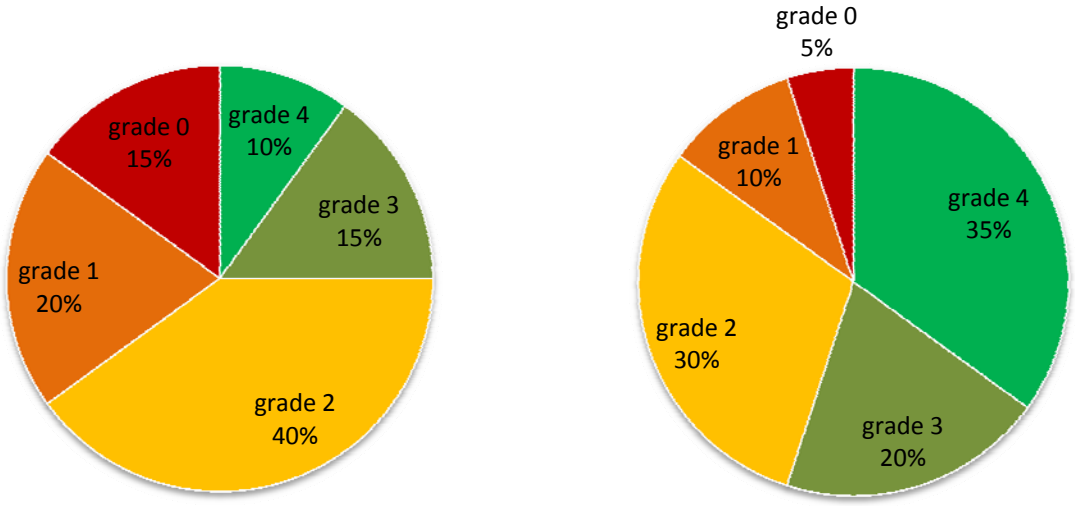

Figure 50 – SPV (a) and SPV+LWSPV (b) pilot study findings on 20 masses: visual grading using the approach described herein.

The LWSPV algorithm proved particularly useful in dealing with clinical cases were the bottom boundary in both B-mode and SPV images was imperceptible. Typical examples are the first two clinical cases discussed in section 5.2 (see figure 43 and figure 45). In fact, the clinical case in figure 45 received grade 1 during the first pilot study and grade 2 during the second pilot study (correct detection of the bottom boundary). The clinical case in figure 43 received grade 0 during the first pilot study, because although the top and lateral boundaries were better defined on the SPV image in comparison with the B-mode image, the inexistence of any clue between the mass and the posterior shadow could mislead the radiologist. Since that problem with the bottom boundary was fixed by the LWSPV algorithm, this case received grade 4 in the second pilot study.

Lastly, let us analyse the case that received grade 0 in both pilot studies (see figure 51). In this very complex case there was the unfortunate combination of two misleading factors. First, there were very hypo-echoic blobs of fat within the parenchyma. As Dr Kopans mentions in his book [12]:

> *"fat in the breast is less echogenic than the mammary parenchyma. Because echogenicity is a relative phenomenon, fat appears hypoechoic relative to the fibroglandular elements that present numerous acoustic mismatches and reflecting surfaces. In the subcutaneous tissues this presents little problem, but fat within the breast parenchyma itself can mimic hypoechoic masses, and care must be taken to avoid mistaking normal fat for a lesion."*

Second, to make things worse, the actual mass was just above a fatty blob, shadowing it and making the respective SPVs even lower. The actual location of the mass is shown in figure 51 (b).

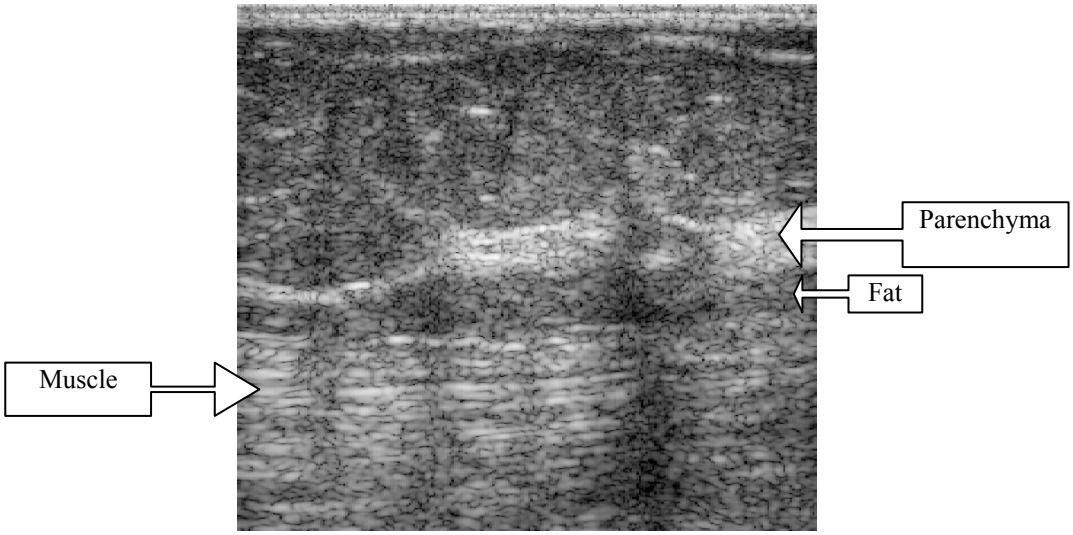

(a)

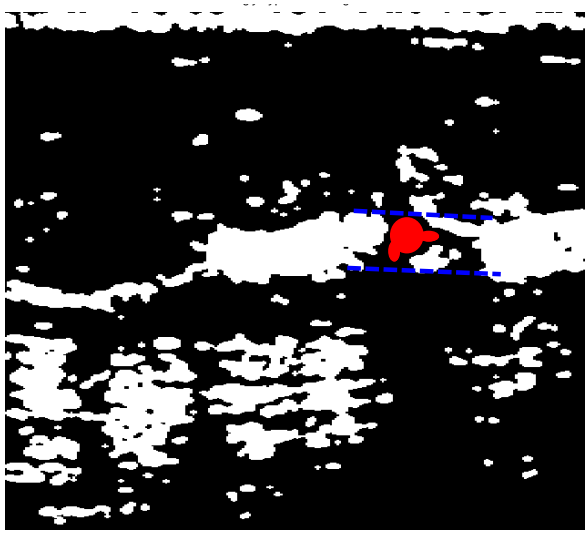

(b)

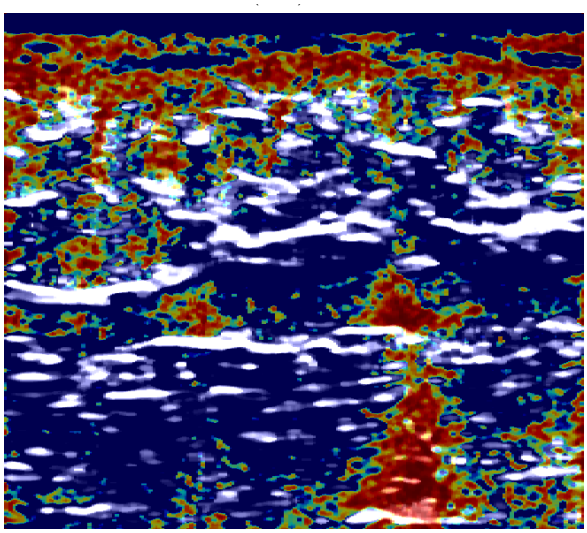

(c)

Figure 51 – Clinical case *#19* (IDC, cf. annex II): This case received grade 0 in both pilot studies: (a) B-mode image; (b) location of the malignant mass (in red) – some anatomic structures identified on the B-mode image were highlighted in white; (c) SPV+LWSPV parametric image.

4.4. Conclusion

In this chapter, the LWSPV algorithm was proposed to recover some anatomical structures (particularly, Cooper's ligaments) which are shadowed during the image acquisition process and, therefore, to improve the conspicuity of mass boundaries (in particular, bottom boundaries). The key idea was to analyse the spectral information in a local context to calculate the local weight of the spectral peak value within a specified neighbourhood (cf. section 4.1).

As mentioned before, it became clear, in conversations with the radiologist, the importance of detecting Cooper's ligaments (particularly the shadowed and porterior-to-mass Cooper's ligaments) as an important tool for aiding radiologists in assessing breast masses. In our 20-case clinical sample there were three cases (patient #2 ,#11 and #13 – cf. section 4.2 for a detailed discussion) where the bottom boundary was strongly affected by the shadowing phenomenon and, therefore, very difficult to detect on the B-mode image (and SPV image). For all three cases, the LWSPV algorithm correctly detected the existence of a shadowed structure[†††].

The information from the LWSPV and SPV algorithms was then combined (i.e. the LWSPV parametric image was superimposed onto the SPV parametric image) to generate a final SPV+LWSPV parametric image – cf. section 4.2 for example images.

[†††] Please note that we do not know the exact location of the Cooper's ligaments (because the histology images were not available). However, the histopathology report, which was analysed by the radiologist, mentions that the malignant mass sits on a Cooper's ligament.

The 20-case pilot study showed that the SPV+LWSPV parametric image added useful information to the B-mode image for clinical assessment in 85% of the cases (increase in diagnostic confidence in at least one boundary). Moreover, in 35% of the cases, the SPV+LWSPV parametric image provided a better definition of the entire boundary. In addition, the SPV+LWSPV methodology has the advantage that it uses the I/Q data from standard ultrasound equipment without the need for additional hardware.

The high-level block diagram of the SPV+LWSPV imaging system is depicted in figure 52. A *Matlab*-based software was developed to straightforwardly generate the *SPV*, *LWSPV* and *SPV+LWSPV* parametric images from the I/Q raw data – see annex VII for further details.

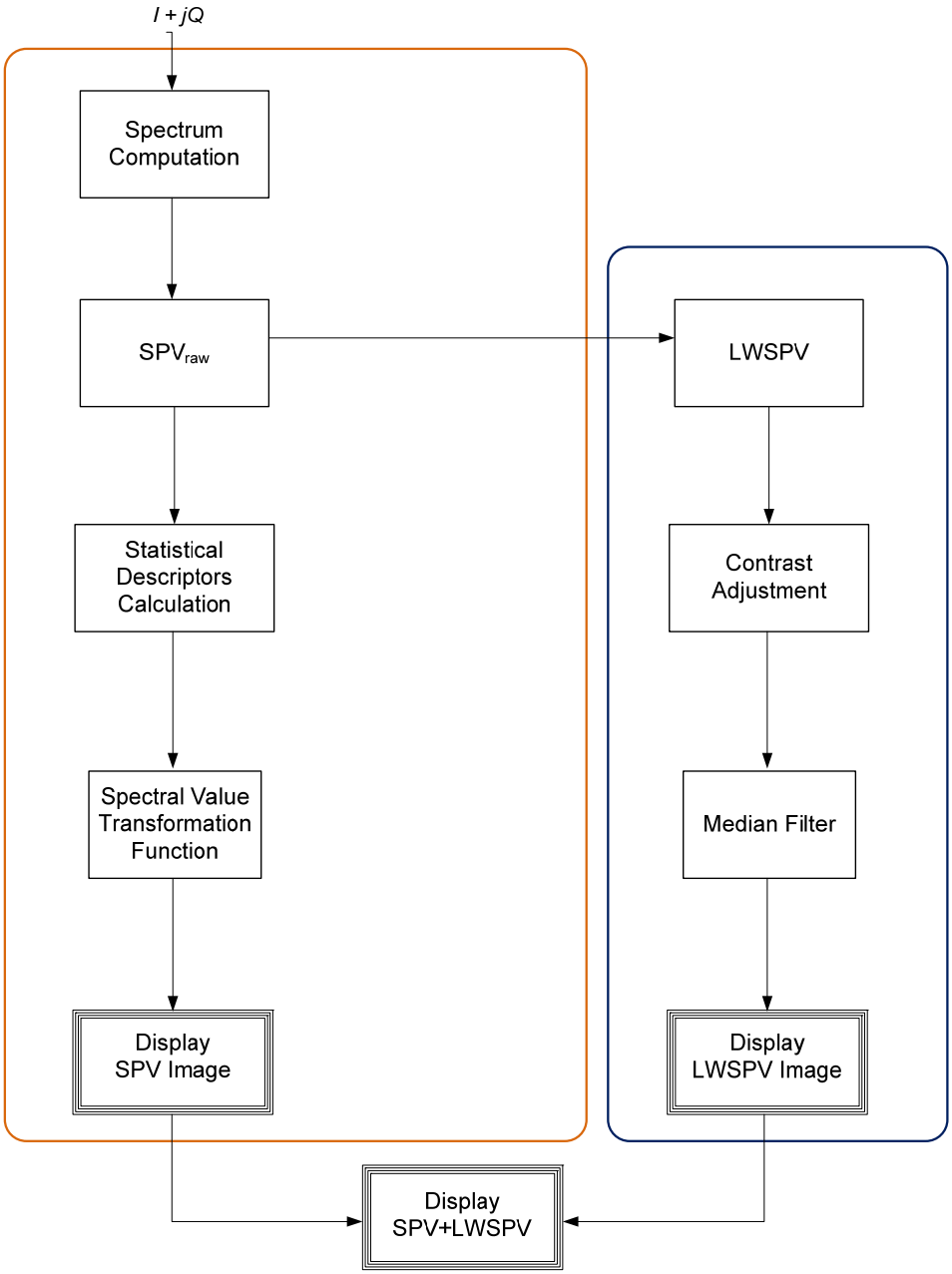

Figure 52 – High-level block diagram of the SPV+LWSPV imaging system.

5. Final Considerations

In this thesis we have investigated a new method of processing the backscattered ultrasound signals from breast tissue (based on the Fourier spectral analysis) to generate parametric images where the visibility of breast mass boundaries is improved.

An improvement in boundary conspicuity was reported using the SPV algorithm (cf. chapter 3). Moreover, less noisy images were generated with this method because better signal-to-noise ratio information was extracted from the spectrum to compute the SPV parameter. However, the SPV imaging was affected by the shadowing phenomenon (similar to B-mode imaging).

Note also that the use of the Fast Fourier Transform algorithm for spectrum estimation together with small windows (to obtain good spatial resolution) gave rise to coarse spectra which, however, worked satisfactorily at the level of detail we were looking for.

The LWSPV algorithm has been proposed to recover some anatomical structures (particularly, Cooper's ligaments) which were shadowed during the image acquisition process. It allowed an improvement in conspicuity of the breast mass bottom boundaries in cases where those boundaries were strongly affected by the shadowing phenomenon and, therefore, very difficult to detect on the B-mode and SPV images (cf. chapter 4). We should notice that, at different ultrasound machine settings, the value of parameter R (which defines the size of the neighbourhood in terms of pixels) should be such that it encompasses a number of pixels approximately

equivalent to 3 millimetres in the axial direction (cf. section 4.1). For our settings, a value of $R = 64$ pixels corresponded to a neighbourhood size of $64 \times 0.048 \approx 3$ millimetres in the axial direction (each pixel corresponded to 0.048 millimetres in the axial direction).

The 20-case pilot study reported in chapter 4 showed that the new methodology – SPV+LWSPV imaging – added useful information to the B-mode image for clinical assessment in 85% of the cases (increase in diagnostic confidence in at least one boundary). Moreover, in 35% of the cases, the SPV+LWSPV parametric image provided a better definition of the entire boundary. Furthermore, the SPV+LWSPV method has the advantage that it uses the I/Q data from standard ultrasound equipment without the need for additional hardware.

Lastly, as far as the pilot study is concerned, two practical limitations should be mentioned. First, histology slides were not available (as initially desired), only the histopathology reports which were used by the radiologist for validation purpose. Second, the test group were post-menopausal women which is not representative of all female age groups because breast tissue becomes fattier and less dense with age [12].

5.1. Future Work

1) Although the goal of the SPV+LWSPV methodology was to improve the visibility of the breast mass boundaries (including cases where the boundary is shadowed), the incorporation of other spectral parameters could add other capabilities to this technique, such as the differentiation among healthy, benign and

malignant tissue. For instance, taking figure 32 into account, it would be interesting to study the incorporation of other spectral features, such as the second highest peak value and the locations of the spectral peaks, to understand if they could be useful to characterize different types of breast tissue.

2) In our methodology we used the Fast Fourier Transform (FFT) algorithm to compute the spectrum. Another option would be the investigation and use of autoregressive modelling for spectral estimation instead of using the FFT algorithm (as discussed in section 2.7).

3) In this work we investigated if the SPV+LWSPV imaging would be a useful tool in the pre-operative assessment of breast mass boundaries. However, this methodology could potentially be useful for breast cancer therapy monitoring too (i.e., it could potentially aid radiologists in better visualizing the breast mass boundaries and, consequently, better monitoring how the mass size evolves with therapy). It would be interesting to conduct a clinical pilot study to evaluate the usefulness of the SPV+LWSPV imaging as a technique to assess treatment response in order to adapt cancer therapy to treatment response. Note that, as discussed in chapter 1, using ultrasound-based methods, patients could be imaged as often as desired by a radiologist without concerns in terms of side effects.

4) Based on the brief preliminary observations presented next, it would also be interesting to conduct a clinical pilot study to understand the potential of the SPV+LWSPV imaging as a complementary tool to elastography.

Elastography (ultrasound elasticity imaging) has been developed and investigated as an additional tool to supplement the diagnostic information obtained during conventional B-mode scanning over the past two decades [109], [110], [111]. This technique is used to evaluate mechanical properties of soft tissue, particularly to estimate tissue stiffness at each subregion on the scan plane. Its importance in clinical practice is based on the observations that the presence of malignant cells in breast parenchyma changes the elastic properties of that tissue, increasing the stiffness in that region [112], [113].

Although elastography has proved useful in detecting difficult malignant masses, some limitations have been reported in the literature, for example [112], [114], [115]. In some clinical cases, elasticity images are affected by posterior shadowing that obscures the bottom boundary of the mass [112]. An example is shown in figure 53, where the boundary in the elasticity image is not clear at all (cf. figure 53(b)). Nevertheless, notice the strong response from the LWSPV algorithm along the bottom boundary of the mass, giving the radiologist an indication that, for instance, the red regions on the elasticity image pointed out by white arrows are shadowing artefacts and not part of the mass. Figure 54 presents another case where the bottom boundary is not clearly detected in the elasticity image. The malignant mass sits on top of a fibrous structure that runs along the green line in figure 54(c). Again, the bottom boundary was correctly detected by the LWSPV algorithm (cf. figure 54(b)).

Figure 55 shows a clinical case where elastography fails to show the red colouration on the malignant areas, i.e. fails to detect the malignant mass [112], [114]. The reason is the fact that the key assumption in elastography that all tumours exhibit greater stiffness than the surrounding tissues does not hold for all patients [114]. Please note that it was not our aim here to conduct a pilot study to compare elastography with SPV+LWSPV imaging. We chose clinical examples were elastography failed to see whether there was a case for further investigation of the SPV+LWSPV method as a complementary diagnostic tool to elastography.

5) Lastly, the SPV+LWSPV methodology could be tested on other organs where ultrasound imaging is commonly employed, such as prostate [116] [117], liver [118] and thyroid [119] [120], to see if it adds diagnostic information to conventional imaging methods for cancer diagnosis.

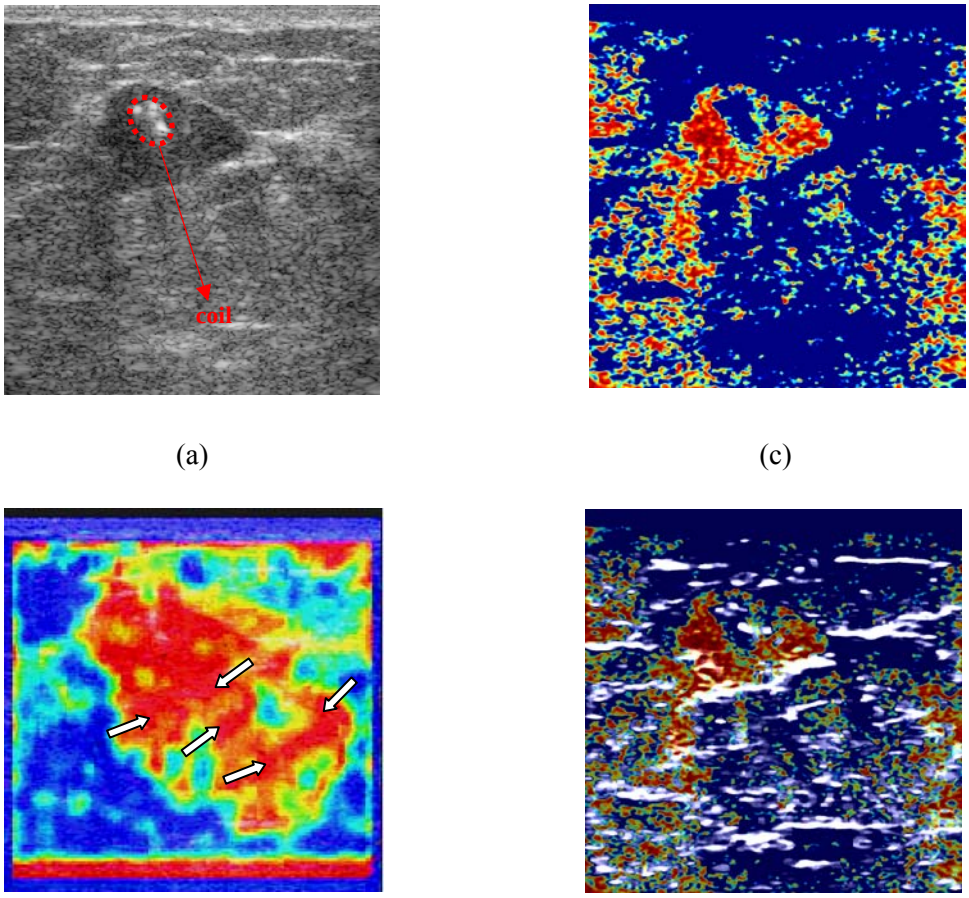

Figure 53 – Clinical case *#18* (IDC, cf. annex II): (a) B-mode image. Note that in the centre of the mass there is a white roundish area which corresponds to a metal coil used as a landmark in another study carried out in our lab. (b) Elasticity image (taken from [114]). The white arrows point to shadowing artefacts. (c) SPV parametric image. (d) SPV+LWSPV parametric image, where the bottom boundary was correctly detected by the algorithm.

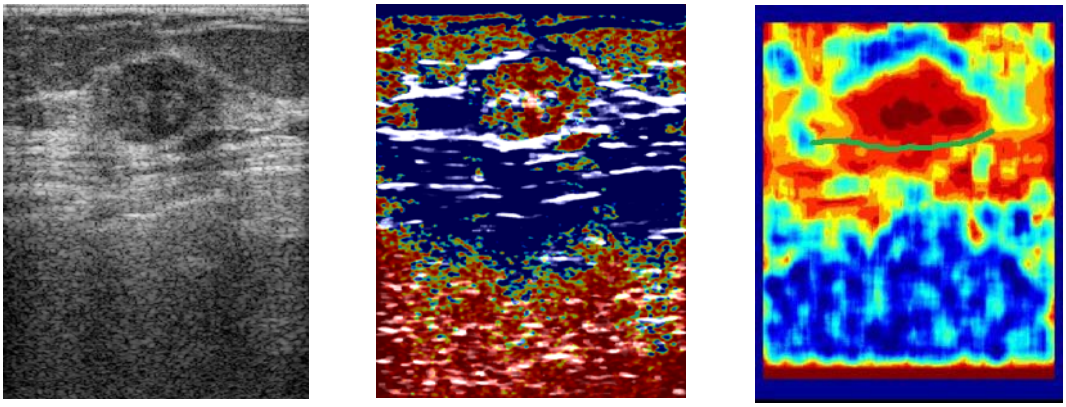

(a) (b) (c)

Figure 54 – Clinical case *#9* (DCIS+IDC, cf. annex II): (a) B-mode image. (b) SPV+LWSPV parametric image, where the bottom boundary was correctly detected by the algorithm. (c) Elasticity image (taken from [114]). The green line indicates where the top of the fibrous structure is.

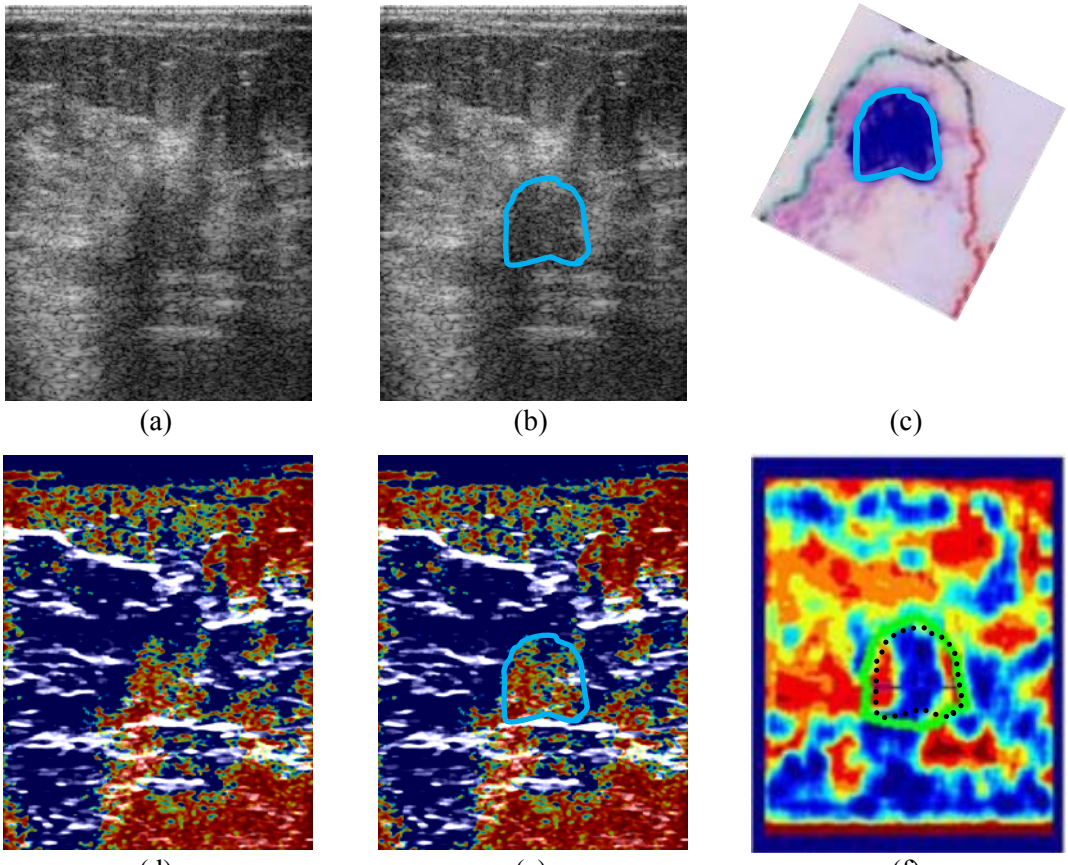

(a) (b) (c)

(d) (e) (f)

Figure 55 – Clinical case *#20* (DCIS+IDC, cf. annex II): (a) B-mode image. (b) B-mode image with the malignant area delineated. (c) Histopathology slide with the malignant area delineated. (d) SPV+LWSPV parametric image. (e) SPV+LWSPV parametric image with the malignant area delineated. (f) Elasticity image (taken from [114]) with the malignant area delineated.

Annex I: Guide to Making Phantoms

Here, a procedure used in this research for creating tissue-mimicking phantoms is summarized. For further details, see [121], [122]. The basic ingredients are: purified gelatine powder, deionised water (H_2O) and, optionally, graphite flakes.

Procedure:

1st: Mix gelatine with water;

2nd: Heat solution to 85ºC for around 1.5 hours to disperse the colloid and clarify the solution;

3rd: Optionally, add graphite flakes to increase scattering and absorption;

4th: Cool it down and pour it into a phantom container;

Annex II: Acronyms for Some Types of Mass

DCIS – Ductal Carcinoma In Situ;

IDC – Invasive Ductal Carcinoma;

ILC – Invasive Lobular Carcinoma;

TC – Tubular Carcinoma (a rare type of invasive ductal carcinoma);

TLC – Tubular plus Lobular Carcinoma.

ACC – Adenoid Cystic Carcinoma

Fibro – Fibroadenoma (benign mass)

Annex III: Tables of Metrics for All Patient

Table 8: Statistics for the **SPV** parametric images using window **W16**.

# patient	VC_{Bmode}(SPV)	Corr (Bmode,SPV)	VI_{norm}(Bmode,SPV)
1	53.25	0.6269	0.8195
2	64.77	0.6348	0.8397
3	63.15	0.6586	0.8334
4	60.78	0.5088	0.8069
5	63.11	0.5837	0.8072
6	63.95	0.6157	0.8117
7	66.31	0.5937	0.8217
8	51.61	0.6586	0.7829
9	45.21	0.5935	0.8062
10	66.16	0.5652	0.7985
11	65.96	0.6114	0.8334
12	61.95	0.5626	0.7951
13	65.29	0.6484	0.8003
14	66.03	0.5682	0.7954
15	60.77	0.5281	0.8023
16	58.04	0.6408	0.8492
17	57.07	0.4930	0.8056
18	64.42	0.4536	0.8123
19	56.37	0.5432	0.8012
20	59.95	0.5599	0.8171
Mean	**60.71**	**0.5824**	**0.8120**
Standard Deviation	**5.67**	**0.0572**	**0.0167**

Table 9: Statistics for the **SPV** parametric images using window **W32**.

# patient	VC_{Bmode}(SPV)	Corr (Bmode,SPV)	VI_{norm}(Bmode,SPV)
1	56.50	0.5911	0.8265
2	65.66	0.5923	0.8379
3	63.47	0.6255	0.8344
4	58.42	0.4485	0.8060
5	60.74	0.5330	0.8087
6	64.98	0.5718	0.8215
7	63.60	0.5309	0.8273
8	52.60	0.6253	0.7940
9	46.26	0.5719	0.8080
10	64.95	0.5011	0.8048
11	67.90	0.5841	0.8372
12	58.34	0.5276	0.7953
13	65.96	0.5918	0.8173
14	67.95	0.5307	0.7953
15	62.05	0.4544	0.8108
16	59.17	0.6142	0.8489
17	56.17	0.3810	0.8267
18	56.01	0.3942	0.7969
19	54.53	0.4710	0.8193
20	64.52	0.5664	0.8197
Mean	**60.49**	**0.5353**	**0.8168**
Standard Deviation	**5.67**	**0.0730**	**0.0159**

Table 10: Statistics for the **SPV** parametric images using window **W64**.

# patient	VC_{Bmode}(SPV)	Corr (Bmode,SPV)	VI_{norm}(Bmode,SPV)
1	59.75	0.5547	0.8302
2	65.74	0.5346	0.8430
3	65.17	0.5807	0.8457
4	62.68	0.4112	0.8176
5	63.62	0.4866	0.8173
6	66.76	0.5236	0.8295
7	63.42	0.4624	0.8430
8	60.63	0.5747	0.8243
9	53.29	0.5563	0.8142
10	63.98	0.4328	0.8231
11	74.02	0.5638	0.8420
12	60.00	0.4990	0.8011
13	64.21	0.5211	0.8446
14	70.45	0.4868	0.8147
15	68.80	0.3958	0.8284
16	63.42	0.5793	0.8561
17	52.31	0.2787	0.8360
18	56.52	0.3433	0.8078
19	54.60	0.3987	0.8333
20	69.82	0.5298	0.8310
Mean	**62.96**	**0.4857**	**0.8291**
Standard Deviation	**5.77**	**0.0847**	**0.0143**

Table 11: Statistics for the **SPV** parametric images using window **W128**.

# patient	VC_{Bmode}(SPV)	Corr (Bmode,SPV)	VI_{norm}(Bmode,SPV)
1	61.00	0.4564	0.8462
2	64.16	0.4462	0.8527
3	64.30	0.4822	0.8609
4	61.60	0.3699	0.8313
5	68.06	0.3944	0.8406
6	69.56	0.4084	0.8446
7	60.26	0.3875	0.8387
8	62.95	0.4705	0.8585
9	56.58	0.5141	0.8177
10	66.59	0.3125	0.8567
11	78.17	0.5075	0.8407
12	57.84	0.4519	0.8180
13	59.40	0.4068	0.8717
14	66.51	0.4085	0.8460
15	68.15	0.2725	0.8437
16	63.05	0.5105	0.8529
17	49.52	0.1825	0.8429
18	55.63	0.2923	0.8096
19	55.11	0.2898	0.8624
20	72.40	0.4525	0.8405
Mean	**63.04**	**0.4008**	**0.8438**
Standard Deviation	**6.63**	**0.0905**	**0.0157**

Table 12: Statistics for the **IBS** parametric images using window **W16**.

# patient	VC_{Bmode}(IBS)	Corr (Bmode,IBS)	VI_{norm}(Bmode,IBS)
1	-13.14	0.8937	0.5486
2	-12.36	0.8776	0.5660
3	-9.93	0.9212	0.5346
4	-8.67	0.7411	0.5993
5	-9.01	0.8115	0.5802
6	-4.17	0.8389	0.5481
7	-17.07	0.7986	0.5877
8	-4.39	0.9396	0.4834
9	-3.88	0.9112	0.5059
10	-1.87	0.7176	0.6004
11	-5.46	0.8665	0.5746
12	3.87	0.8116	0.5618
13	-12.64	0.8421	0.5658
14	1.07	0.8010	0.5842
15	-1.86	0.6470	0.6312
16	-9.07	0.9424	0.5104
17	-2.92	0.6026	0.6323
18	-2.43	0.6638	0.6073
19	-6.90	0.7491	0.5929
20	-0.35	0.8736	0.5409
Mean	**-6.06**	**0.8125**	**0.5678**
Standard Deviation	**5.36**	**0.0989**	**0.0398**

Table 13: Statistics for the spectral intercept (**SI**) parametric images using window **W16**.

# patient	**VC_{Bmode}(SI)**	**Corr (Bmode,SI)**	**VI_{norm}(Bmode,SI)**
1	-15.84	0.8025	0.6746
2	-21.44	0.7936	0.6852
3	-14.59	0.8063	0.6750
4	-13.98	0.7209	0.7328
5	-13.54	0.7692	0.7112
6	-10.37	0.7644	0.6724
7	-26.94	0.7571	0.7001
8	-12.11	0.8150	0.6011
9	-12.38	0.8032	0.6208
10	-6.69	0.7147	0.7570
11	-14.35	0.7727	0.6973
12	-3.96	0.7427	0.7130
13	-16.99	0.7813	0.7098
14	-10.04	0.7307	0.7757
15	-5.03	0.6971	0.7438
16	-17.84	0.8262	0.6798
17	-9.00	0.6708	0.7880
18	-5.07	0.6699	0.7596
19	-9.91	0.7426	0.7142
20	-14.37	0.6563	0.8062
Mean	**-12.72**	**0.7519**	**0.7109**
Standard Deviation	**5.66**	**0.0511**	**0.0521**

Table 14 : Statistics for the B-mode-QTF images.

# patient	VC_{Bmode}(BmodeQTF)	Corr (Bmode,BmodeQTF)	VI_{norm}(Bmode,BmodeQTF)
1	48.93	0.8076	0.7096
2	52.23	0.8127	0.7248
3	50.20	0.8240	0.6936
4	59.40	0.8034	0.6614
5	54.51	0.8130	0.6501
6	53.42	0.8224	0.6709
7	55.86	0.8264	0.6978
8	46.51	0.8202	0.6308
9	44.76	0.7839	0.6958
10	56.99	0.8194	0.6256
11	54.49	0.8145	0.7099
12	55.27	0.8085	0.6472
13	52.89	0.8441	0.6260
14	59.11	0.8202	0.6011
15	56.49	0.8098	0.6679
16	47.64	0.7891	0.7310
17	54.74	0.8082	0.6203
18	64.03	0.8027	0.6832
19	53.79	0.8089	0.6322
20	53.29	0.8157	0.6954
Mean	**53.73**	**0.8127**	**0.6687**
Standard Deviation	**4.60**	**0.0130**	**0.0382**

Annex IV: Magnitude of the Spectral Peak Shift

The magnitude of the spectral peak shift was also investigated as a potential parameter to generate ultrasound parametric images.

In figure 56, the spectral peak locations are plotted across the ultrasound scan plane for two clinical examples. After generating this type of parametric images for the 20 clinical cases using the spectral peak location as the parameter, no direct relation between those images and the tumour/anatomical structures was observed. Thus, the magnitude of the shift was not used.

Note that the simplified theoretical model based on equation 3 (section 2.4) has proved not a good model of the backscattered spectrum *in vivo* soft tissue, due to several factors such as: the intervening tissue between the transducer and the region under analysis encompasses several unknown inhomogeneous regions with different properties; there exists attenuation during the propagation in the intervening tissue; acoustic properties change across the tissue (e.g. a constant speed of sound across the medium is assumed in equation 3); some *in vivo* tissue constituents are not static (e.g. blood flowing in vessels).

In sum, the results on clinical data showed that the relationship between the frequency shift and tissue type was not clear (cf. figure 56) and differed greatly from the idealised model introduced in chapter 2. Therefore, the relationship between the frequency shift and tissue type was not pursued in the main body of this thesis.

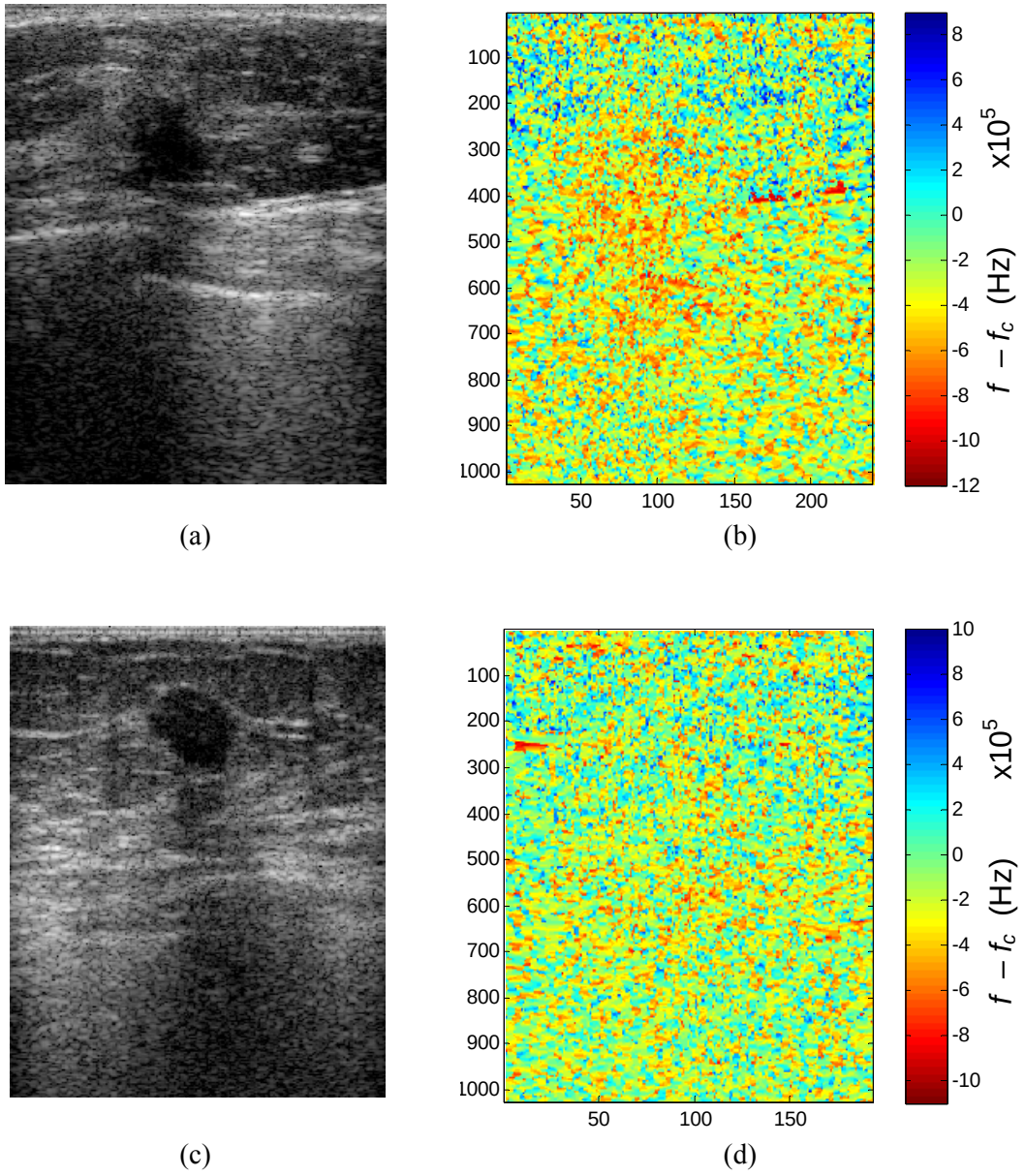

Figure 56 – B-mode image (left) and magnitudes of the spectral peak shift across the ultrasound scan plane (right) for clinical case #16 (ILC, cf. annex II) at the top and for clinical case #1 (DCIS, cf. annex II) at the bottom (centre-frequency *fc* = 8.3MHz).

Annex V: Signal-to-Noise Ratio Analysis

In this annex, we investigate the evolution of the signal-to-noise ratio (SNR)[‡‡‡] with the number of discrete frequencies encompassed in the calculation of the spectral peak. The raw ultrasound data in the time-domain, $signal[n]$, was corrupted by additive Gaussian noise with zero mean and variance σ^2, yielding $signal'[n]$. The $signal[n]$ amplitude was normalized to 1 and the Gaussian noise variance σ^2 was set to $\left(\frac{1}{3}\right)^2$ in order for the *noise* amplitude to be within the *signal* amplitude in 99.7% of the samples[§§§].

$$signal[n] \xrightarrow{windowing\ and\ FFT} SIGNAL[m]$$

$$signal[n] + noise[n]_{(0,\sigma^2)} = signal'[n] \xrightarrow{windowing\ and\ FFT} SIGNAL'[m]$$

In the frequency domain we have:

$$NOISE[m] = SIGNAL'[m] - SIGNAL[m]$$

Then, the SNR was computed as follows,

$$SNR_{nfreq} = \frac{\sum_{nfreq}|SIGNAL[m]|^2}{\sum_{nfreq}|NOISE[m]|^2}$$

[‡‡‡] The signal-to-noise ratio (SNR) is a quantitative parameter to account for the effect of noise and is defined as the ratio of the signal power to the noise power [42].

[§§§] $3\sigma = 1 \Rightarrow \sigma = \frac{1}{3}$

where *nfreq* is the number of discrete frequencies encompassed in the calculation. The SNR was calculated considering the 3, 5, 7, 9, 11, 13, 15, 17 and 19 discrete frequencies around the spectral maximum value of $SIGNAL[m]$, as illustrated in figure 57.

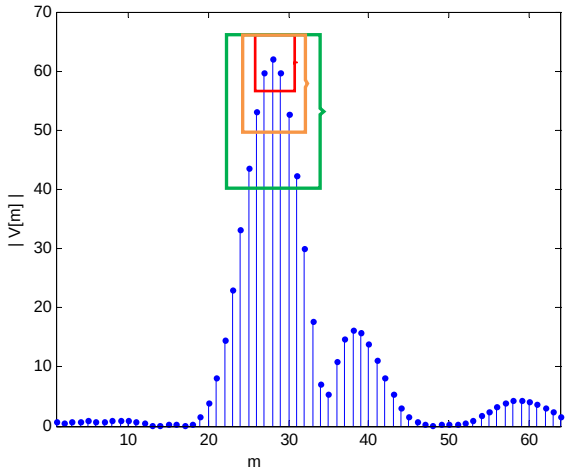

Figure 57 – Let us consider the example spectrum above (vertical axis: magnitude of the spectrum; horizontal axis: *m*th discrete frequency). For *nfreq* = 3, the magnitudes of the three discrete frequencies encompassed by the red rectangle were used; for *nfreq* = 5, the magnitudes of the five discrete frequencies encompassed by the orange rectangle were used; for *nfreq* = 7, the magnitudes of the seven discrete frequencies encompassed by the green rectangle were used; and so forth.

For $nfreq = 1$, the maximum value was not used alone[****]. Instead, a weighted amplitude from its two neighbours was used as follows,

$$SNR|_{nfreq=1} = \frac{|SIGNAL[M-1]|^2 + \mathbf{2} \cdot |SIGNAL[M]|^2 + |SIGNAL[M+1]|^2}{|NOISE[M-1]|^2 + \mathbf{2} \cdot |NOISE[M]|^2 + |NOISE[M+1]|^2}$$

where *M* is the discrete frequency *m* at which $SIGNAL[m]$ is maximum.

[****] The reason for it is that, in practice, if we used the spectral maximum value alone in the SPV algorithm, it would make the algorithm very vulnerable to outliers (i.e., the entire SPV parameter calculation would be dependent on only one spectral value).

The evolution of the SNR with the number of discrete frequencies used is plotted in figure 58 – the larger the number of discrete frequencies considered, the lower the signal-to-noise ratio.

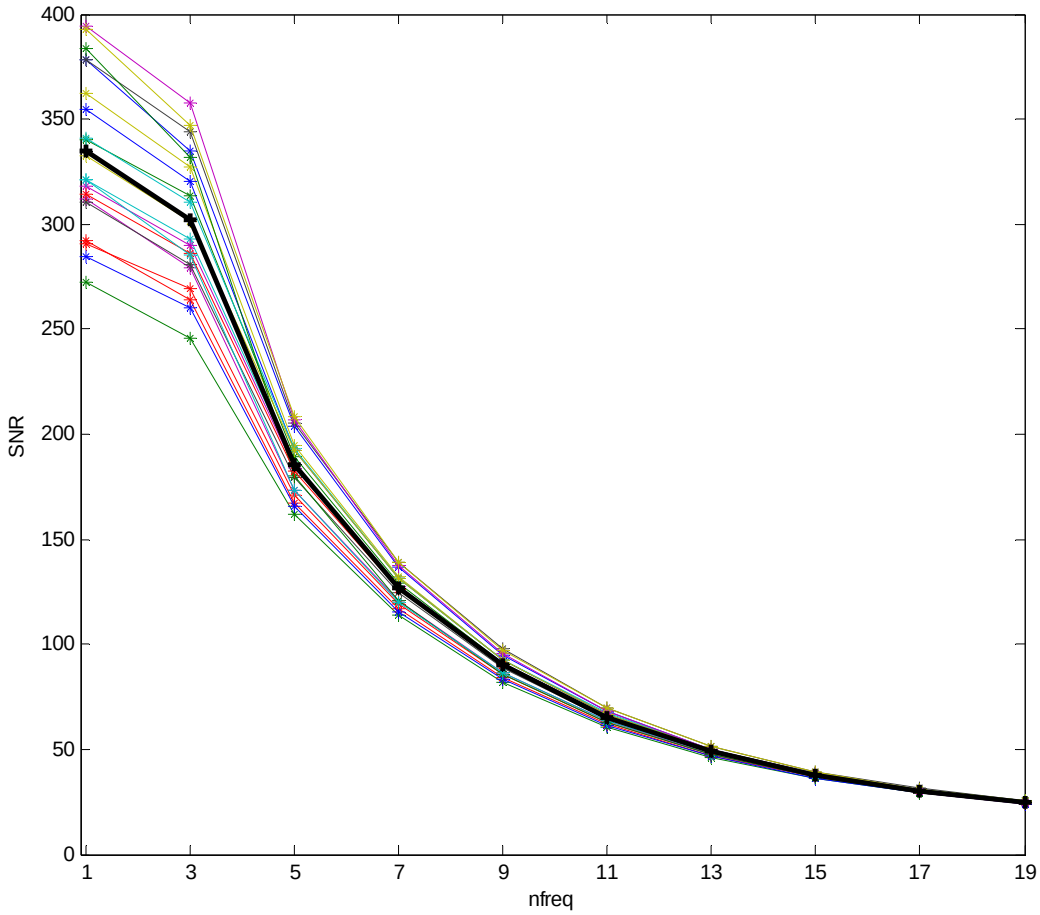

Figure 58 – Evolution of the signal-to-noise ratio (SNR) with the number of discrete frequencies used (*nfreq*) [††††]. Each line represents a different patient. The black line corresponds to the average.

[††††] Note that for *nfreq* = 1, a weighted amplitude from its two neighbours was used.

Annex VI: LWSPV Image of a Cherry Phantom

A gelatine phantom was made following the procedure described in annex I. Graphite flakes were added to the gelatine to create a "forest" of scatterers and a cherry (with its stem) was placed at the bottom as illustrated in figure 59(a).

On the B-mode image (cf. figure 59(b)), the cherry stem is observed to be almost imperceptible, as does the stone. It does not mean in itself that the stem and the stone are hypo-echoic. Simply, in a global context, the forest of scatterers are hyper-echoic and divert away a large percentage of the ultrasound emitted energy to create an apparent acoustic shadow below.

As observed in figure 59 (c), the LWSPV algorithm proved useful to detect structures that are "drowned out" by other structures during the ultrasound image acquisition process.

Figure 59 (d) shows the LWSPV values along scan line 20. Notice that the thin spikes are caused by the forest of scatterers (graphite flakes) and the thick spike is caused by the cherry stem.

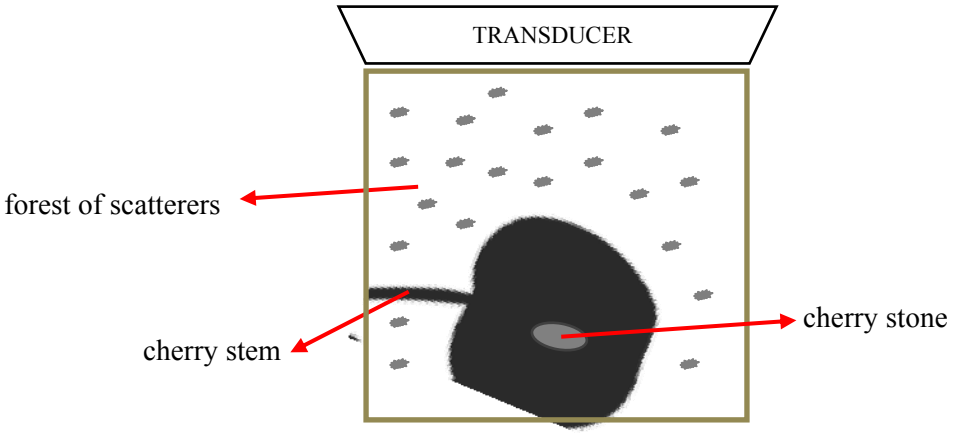

(a)

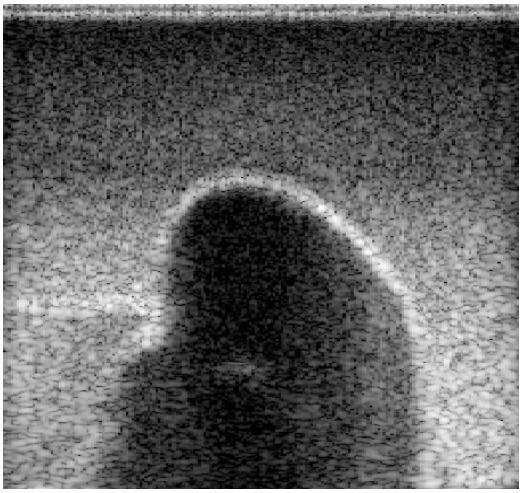

(b)

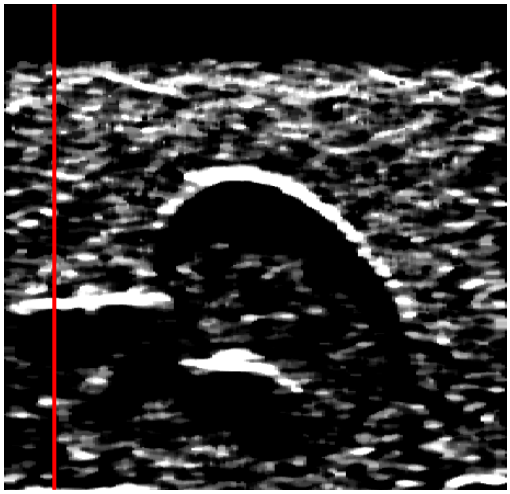

(c)

Figure 59 – (a) Diagram of the cheery phantom, (b) B-mode image, (c) LWSPV image (the scan line 20 is marked in red).

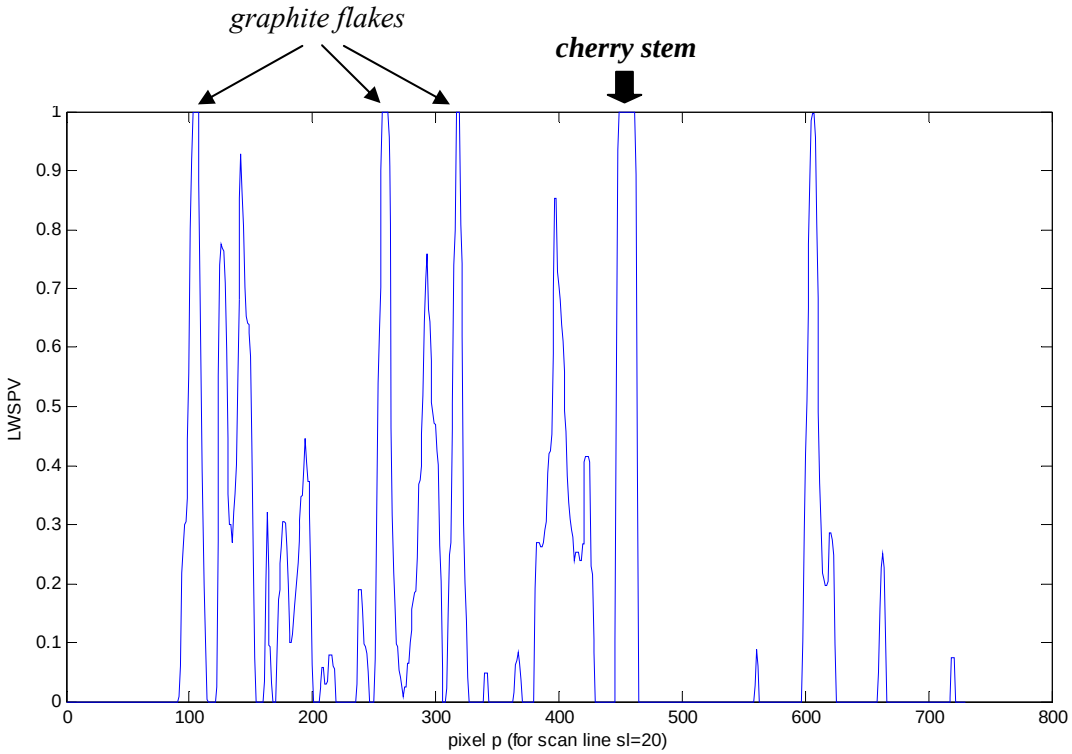

(d)

Figure 54 (*cont.*) – (d) LWSPV values along scan line 20. Notice that the thin spikes are caused by the forest of scatterers (graphite flakes) and the thick spike is caused by the cherry stem.

Annex VII: How to use the SPV+LWSPV Software

Here we explain how to use the *Matlab*-based software we developed to generate the *SPV*, *LWSPV* and *SPV+LWSPV* parametric images – see software workflow in figure 60.

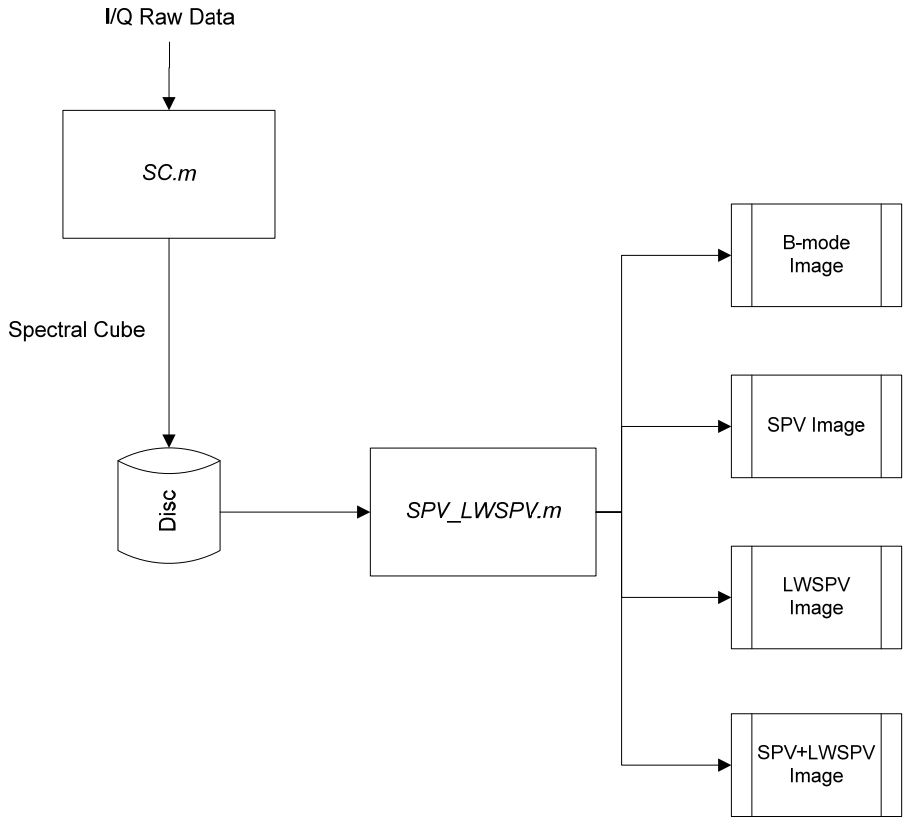

Figure 60 – Software workflow to generate the *B-mode*, *SPV*, *LWSPV* and *SPV+LWSPV* images using the *Matlab* functions developed during this project.

Firstly, use the following command to generate the spectral cube (i.e. spectral 3-D matrix) from the I/Q raw data: *spectral_cube = SC (raw_data)*.

The spectral cube for a certain patient can then be saved on disc for later use. To generate and show on screen the *B-mode*, *SPV*, *LWSPV* and *SPV+LWSPV* images, run the *SPV_LWSPV.m* function.

Annex VIII: H-shadow Detector

We developed an algorithm that incorporated spatial information to identify potential shadowed pixel rows in order to re-calculate the saturation point *sp* (cf. chapter 3) excluding those rows from the calculation. The idea would be the incorporation of this routine into the SPV-image-generation algorithm.

Let *nl* be the number of scan lines (columns in the image) and let Q_1 and Q_2 be the first and second quartile of the *SPV* histogram for the full image. Potential shadowed pixel rows are found as follows.

FOR each row:

C1 = number of pixels with a $SPV \leq Q_1$;

C2 = number of pixels with a $SPV \geq Q_2$;

IF $C1 \geq \frac{1}{2} \cdot nl$ *AND* $C2 \leq \frac{1}{4} \cdot nl$

THEN label this row as corrupted

END IF

END FOR

Notice that if the *SPV* histogram for a certain row and for the full image is identical, then $C1 = \frac{1}{4} \cdot nl$ ***AND*** $C2 = \frac{1}{2} \cdot nl$.

A given row is then labelled as corrupted if there is an abnormal concentration of both low and high *SPV* values along that row. The statistical descriptors – Q_1 and Q_2 – are next re-calculated without using the corrupted rows and a new *sp* is obtained.

However, the only clinical case where it had a significant impact on the final image is shown in figure 61. And even for this case, the radiologist gave *grade 1* (cf. chapter 3) for both SPV images in figure 61(b) and figure 61(d). The h-shadow detector routine was therefore discarded.

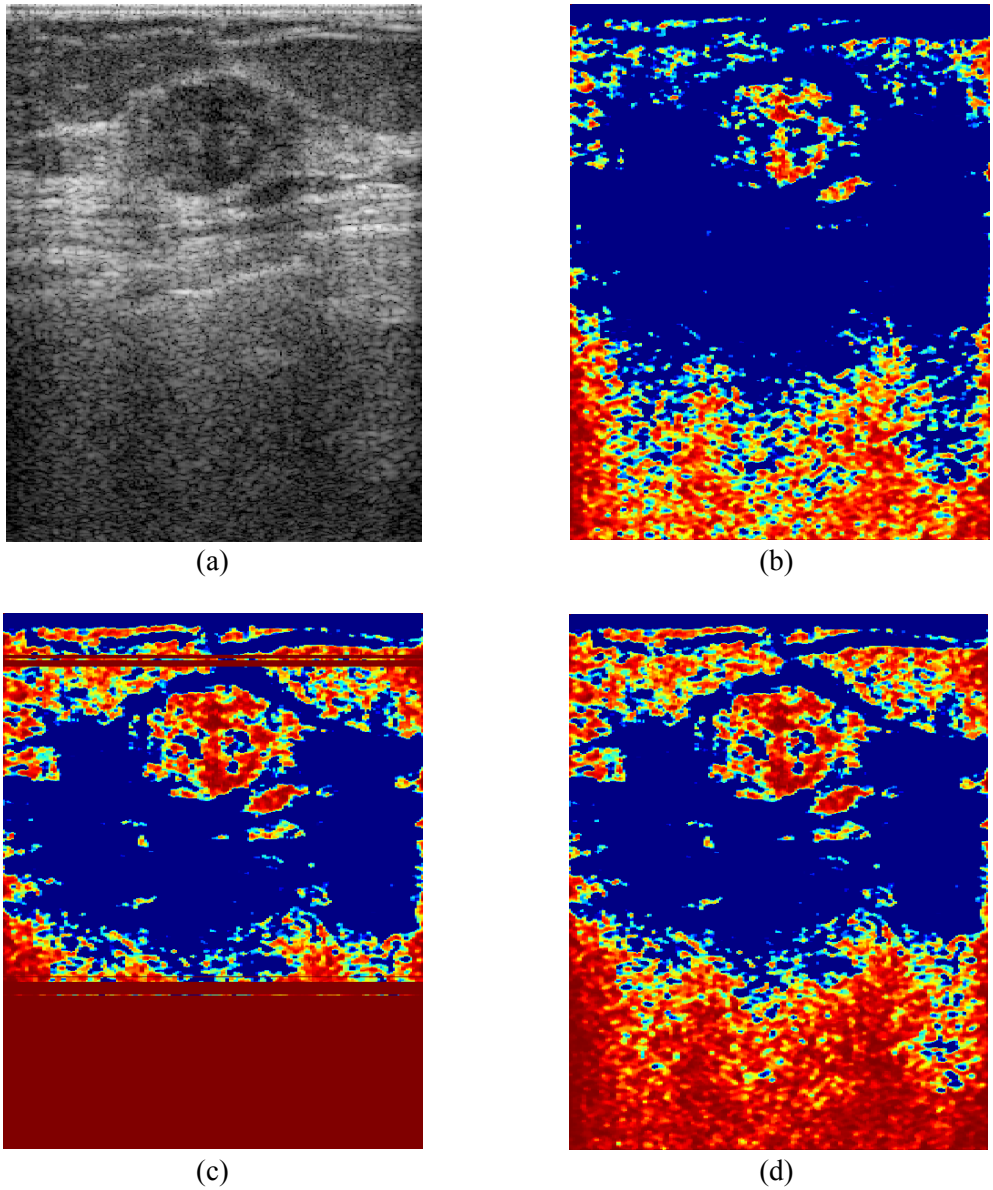

Figure 61 – Clinical case *#9* (DCIS+IDC, cf. annex II): (a) B-mode ultrasound image; (b) *SPV* parametric image using initial *sp* value; (c) rows automatically detected as shadowed regions are crossed out in dark red; (d) *SPV* parametric image using the new *sp* value after employing the *H-shadow Detector*.

Annex IX: Strongly-hyperechoic-region Selector

As discussed in chapter 3, breast masses are typically characterized by hypo-echoic regions surrounded by less hypo-echoic tissues. It is an important characteristic but during the process of identifying masses, radiologists also look for (normally hyper-echoic) anatomic structures locally disrupted. In order to identify regions where medium- and large-size hyper-echoic areas are disrupted, pixels with a SPV equal or greater than Q_3 were mapped to white (1) over a black background (0).

To refine the image, an opening morphological operation (erosion operation followed by dilation operation) was employed [123], using a 7-by-3 rectangular structuring element. The pseudocode of the algorithm is as follows.

HyperR // binary image

FOR each pixel:

IF $SPV \geq Q_3$

THEN *HyperR* = 1

ELSE *HyperR* = 0

END FOR

SE = ones(7,3) // 7-by-3 rectangle

HyperR = (HyperR $\ominus$ *SE)* $\oplus$ *SE // opening morphological operation*

However, during the first pilot study (described in chapter 4), this algorithm was found not as useful as initially thought, mainly because it didn't increase the

diagnostic confidence in comparison with B-mode images. An exception was the clinical case in figure 62.

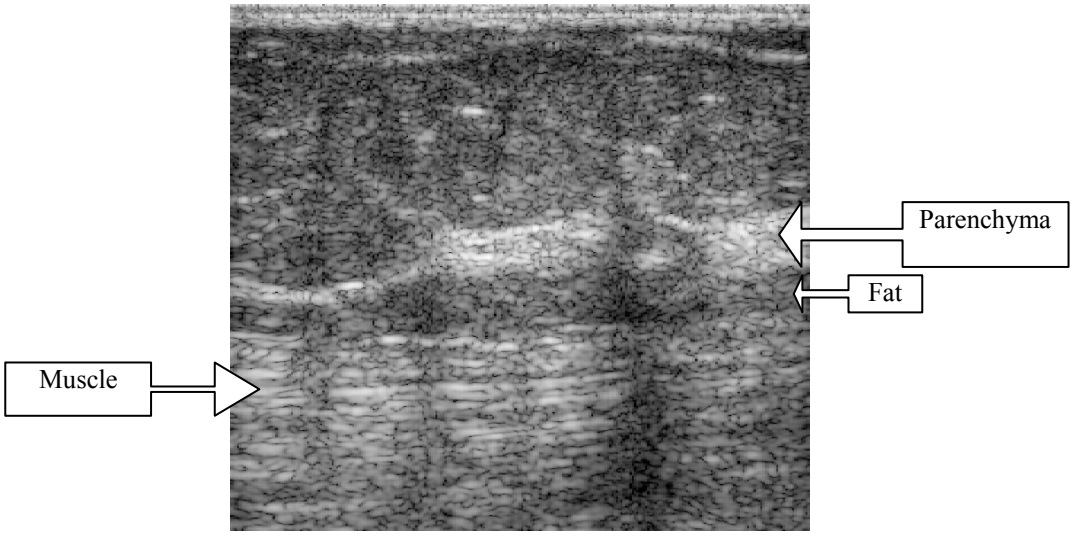

(a)

(b)

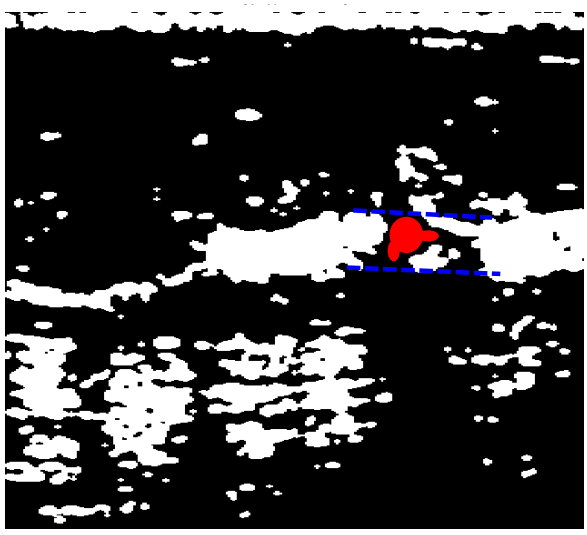

(c)

Figure 62 – Clinical case *#19* (IDC, cf. annex II): (a) B-mode ultrasound image; (b) strongly-hyper-echoic regions (in white) detected using the algorithm described in this chapter; (c) the region in red corresponds to the malignant mass location.

List of Tables

List of Figures

References

[1] Cancer Research UK, "Cancer Stats: Breast Cancer," November 2012.

[2] P. J. Dempsey, "The history of breast ultrasound," *Journal of Ultrasound in Medicine,* vol. 23, pp. 887-894, Jul 2004.

[3] H. D. Liang*, et al.*, "Recent advances in biomedical ultrasonic imaging techniques," *Interface Focus,* vol. 1, pp. 475-476, 2011.

[4] C. W. Piccoli and F. Forsberg, "Advanced ultrasound techniques for breast imaging," *Seminars in Roentgenology,* vol. 46, pp. 60-67, 2011.

[5] J. Powers and F. Kremkau, "Medical ultrasound systems," *Interface Focus,* vol. 1, pp. 477-489, 2011.

[6] B. Mesurolle*, et al.*, "Tissue harmonic imaging, frequency compound imaging, and conventional imaging - Use and benefit in breast sonography," *Journal of Ultrasound in Medicine,* vol. 26, pp. 1041-1051, Aug 2007.

[7] R. G. Barr*, et al.*, "Comparison of Conventional, Compounding, Computer Enhancement, and Compounding With Computer Enhancement in Ultrasound Imaging of the Breast," *Ultrasound Quarterly,* vol. 25, pp. 129-134, Sep 2009.

[8] E. D. Light*, et al.*, "Progress in two-dimensional arrays for real-time volumetric imaging," *Ultrasonic Imaging,* vol. 20, pp. 1-15, Jan 1998.

[9] I. S. Salgo, "Three-dimensional echocardiographic technology," *Cardiology Clinics,* vol. 25, p. 231, May 2007.

[10] D. DeBusschere and L. Mo, "Zonare z.one Research Package User's Guide," Zonare Medical Systems, 2009.

[11] "NHS Cancer Screening Programmes, Breast screening resource pack for training primary care nurses," 2003.

[12] D. B. Kopans, *Breast imaging*, 3rd ed. Philadelphia ; London: Lippincott Williams & Wilkins, 2007.

[13] A. Kornecki, "Current status of breast ultrasound," *Canadian Association of Radiologists Journal,* vol. 62, pp. 31-40, 2011.

[14] W. A. Berg*, et al.*, "Diagnostic accuracy of mammography, clinical examination, US, and MR imaging in preoperative assessment of breast cancer," *Radiology,* vol. 233, pp. 830-849, Dec 2004.

[15] J. Mamou and M. L. Oelze, *Quantitative ultrasound in soft tissues*, N.Y.: Springer, 2013.

[16] M. D. Pickles*, et al.*, "Role of dynamic contrast enhanced MRI in monitoring early response of locally advanced breast cancer to neoadjuvant chemotherapy," *Breast Cancer Research and Treatment,* vol. 91, pp. 1-10, May 2005.

[17] L. Martincich*, et al.*, "Monitoring response to primary chemotherapy in breast cancer using dynamic contrast-enhanced magnetic resonance imaging," *Breast Cancer Research and Treatment,* vol. 83, pp. 67-76, Jan 2004.

[18] A. Berriolo-Riedinger*, et al.*, "[F-18]FDG-PET predicts complete pathological response of breast cancer to neoadjuvant chemotherapy," *European Journal of Nuclear Medicine and Molecular Imaging,* vol. 34, pp. 1915-1924, Dec 2007.

[19] J. D. Schwarz*, et al.*, "Early prediction of response to chemotherapy in metastatic breast cancer using sequential F-18-FDG PET," *Journal of Nuclear Medicine,* vol. 46, pp. 1144-1150, Jul 2005.

[20] D. E. Ray*, et al.*, "Neurotoxic effects of gadopentetate dimeglumine: Behavioral disturbance and morphology after intracerebroventricular injection in rats," *American Journal of Neuroradiology,* vol. 17, pp. 365-373, Feb 1996.

[21] B. B. Goldberg*, et al.*, *Ultrasound contrast agents : basic principles and clinical applications*, 2nd ed. London: Martin Dunitz, 2001.

[22] E. Cassano*, et al.*, "Contrast enhanced ultrasound of breast cancer," *Cancer Imaging,* vol. 6, pp. 4-6, 2006.

[23] M. J. Blomley*, et al.*, "Microbubble contrast agents: a new era in ultrasound," *BMJ,* vol. 322, pp. 1222-5, May 2001.

[24] G. Gasparini and A. L. Harris, "Clinical importance of the determination of tumor angiogenesis in breast carcinoma: much more than a new prognostic tool," *Journal of Clinical Oncology,* vol. 13, pp. 765-82, Mar 1995.

[25] M. H. Chaudhari*, et al.*, "Breast tumor vascularity identified by contrast enhanced ultrasound and pathology: initial results," *Ultrasonics,* vol. 38, pp. 105-109, Mar 2000.

[26] C. R. Hill*, et al.*, *Physical principles of medical ultrasonics*, 2nd ed. Chichester ; Hoboken, N.J.: John Wiley & Sons, 2004.

[27] M. De Podesta, *Understanding the properties of matter*, 2nd ed. London: Taylor & Francis, 2002.

[28] T. L. Szabo, *Diagnostic ultrasound imaging : inside out*, Burlington, MA. ; London: Elsevier Academic, 2004.

[29] M. Ali*, et al.*, "Signal Processing Overview of Ultrasound Systems for Medical Imaging," Texas Instruments, 2008.

[30] F. S. Foster and J. W. Hunt, "Transmission of ultrasound beams through human tissue - focusing and attenuation studies," *Ultrasound in Medicine and Biology,* vol. 5, pp. 257-268, 1979.

[31] M. F. Insana*, et al.*, "Describing Small-Scale Structure in Random-Media Using Pulse-Echo Ultrasound," *Journal of the Acoustical Society of America,* vol. 87, pp. 179-192, Jan 1990.

[32] K. K. Shung and G. A. Thieme, *Ultrasonic scattering in biological tissues*. Boca Raton: CRC Press, 1993.

[33] D. K. Nassiri and C. R. Hill, "The Use of Angular Acoustic Scattering Measurements to Estimate Structural Parameters of Human and Animal-Tissues," *Journal of the Acoustical Society of America,* vol. 79, pp. 2048-2054, Jun 1986.

[34] T. A. Bigelow*, et al.*, "Estimation of total attenuation and scatterer size from backscattered ultrasound waveforms," *Journal of the Acoustical Society of America,* vol. 117, pp. 1431-1439, Mar 2005.

[35] M. L. Oelze and W. D. O'Brien, "Method of improved scatterer size estimation and application to parametric imaging using ultrasound," *Journal of the Acoustical Society of America,* vol. 112, pp. 3053-3063, Dec 2002.

[36] A. Briggs and W. Arnold, *Advances in acoustic microscopy*. New York ; London: Plenum, 1995.

[37] A. Briggs and O. V. Kolosov, *Acoustic microscopy*, 2nd ed. Oxford: Oxford University Press, 2010.

[38] P. M. Morse and K. U. Ingard, *Theoretical acoustics*. Princeton, N.J.: Princeton University Press, 1986.

[39] E. G. Williams, "Chapter 6: Spherical Waves," in *Fourier acoustics : sound radiation and nearfield acoustical holography*, ed San Diego ; London: Academic, 1999.

[40] F. Jafari*, et al.*, "Exact Evaluation of an Ultrasonic Scattering Formula for a Rigid Immovable Sphere," *Ultrasound in Medicine and Biology,* vol. 7, pp. 293-296, 1981.

[41] F. L. Lizzi*, et al.*, "Ultrasonic spectrum analysis for tissue evaluation," *Pattern Recognition Letters,* vol. 24, pp. 637-658, Feb 2003.

[42] A. V. Oppenheim*, et al.*, *Discrete-time signal processing*, 2nd ed. Upper Saddle River, N.J.: Prentice Hall, 1999.

[43] The MathWorks, *Signal Processing Toolbox™ 6 User's Guide*, 2009.

[44] S. T. Karris, *Signals and systems with MATLAB computing and Simulink modeling, 4th ed.*, 2008 [ebook].

[45] A. Bateman and I. Paterson-Stephens, *The DSP handbook : algorithms, applications and design techniques*. Upper Saddle River, NJ: Prentice Hall, 2002.

[46] R. N. Bracewell, *The Fourier transform and its applications*, 3rd ed. Boston ; London: McGraw Hill, 2000.

[47] E. J. Feleppa*, et al.*, "Quantitative ultrasound in cancer imaging," *Seminars in Oncology,* vol. 38, pp. 136-150, 2011.

[48] F. L. Lizzi, *et al.*, "Theoretical Framework for Spectrum Analysis in Ultrasonic Tissue Characterization," *Journal of the Acoustical Society of America,* vol. 73, pp. 1366-1373, 1983.

[49] T. L. Szabo, *et al.*, "Determining the pulse-echo electromechanical characteristic of a transducer using flat plates and point targets," *Journal of the Acoustical Society of America,* vol. 116, pp. 90-96, Jul 2004.

[50] E. J. Feleppa, *et al.*, "Ultrasonic spectral-parameter imaging of the prostate," *International Journal of Imaging Systems and Technology,* vol. 8, pp. 11-25, 1997.

[51] F. L. Lizzi, *et al.*, "Ultrasonic spectrum analysis for tissue assays and therapy evaluation," *International Journal of Imaging Systems and Technology,* vol. 8, pp. 3-10, 1997.

[52] F. L. Lizzi, *et al.*, "On the statistics of ultrasonic spectral parameters," *Ultrasound in Medicine and Biology,* vol. 32, pp. 1671-1685, Nov 2006.

[53] M. L. Oelze, *et al.*, "Parametric imaging of rat mammary tumors in vivo for the purposes of tissue characterization," *Journal of Ultrasound in Medicine,* vol. 21, pp. 1201-1210, 2002.

[54] M. L. Oelze and J. F. Zachary, "Characterization of tissue microstructure using ultrasonic backscatter: Theory and technique for optimization using a Gaussian form factor," *Journal of the Acoustical Society of America,* vol. 112, pp. 1202-1211, Sep 2002.

[55] F. L. Lizzi, *et al.*, "Ultrasonic spectrum analysis for assays of different scatterer morphologies: Theory and very-high frequency clinical results," in

1996 Ieee Ultrasonics Symposium Proceedings, Vols 1 and 2, pp. 1155-1159, 1996.

[56] L. Kuang-Wei, *et al.*, "Ultrasound backscatter spectral analysis provides image feedback for histotripsy tissue fractionation," *2011 IEEE International Ultrasonics Symposium (IUS),* pp. 33-3636, 2011 2011.

[57] U. Scheipers, *et al.*, "Ultrasonic multifeature tissue characterization for prostate diagnostics," *Ultrasound in Medicine and Biology,* vol. 29, pp. 1137-1149, 2003.

[58] S. K. Alam, *et al.*, "Multi-feature analysis for automated breast lesion classification from ultrasonic data," *Proceedings of the Ieee 28th Annual Northeast Bioengineering Conference,* pp. 287-288, 2002.

[59] S. K. Alam, *et al.*, "Ultrasonic Multi-Feature Analysis Procedure for Computer-Aided Diagnosis of Solid Breast Lesions," *Ultrasonic Imaging,* vol. 33, pp. 17-38, Jan 2011.

[60] K. D. Donohue, *et al.*, "Tissue classification with generalized spectrum parameters," *Ultrasound in Medicine and Biology,* vol. 27, pp. 1505-1514, Nov 2001.

[61] B. Krasner, *et al.*, "Optimization of Quantitative Sonographic Diagnostic-Analysis of Breast-Lesions," *Image Perception,* vol. 2166, pp. 24-31, 1994.

[62] A. V. Alvarenga, *et al.*, "Complexity curve and grey level co-occurrence matrix in the texture evaluation of breast tumor on ultrasound images," *Medical Physics,* vol. 34, pp. 379-387, Feb 2007.

[63] W. Gomez, *et al.*, "Analysis of Co-Occurrence Texture Statistics as a Function of Gray-Level Quantization for Classifying Breast Ultrasound," *Ieee Transactions on Medical Imaging,* vol. 31, pp. 1889-1899, Oct 2012.

[64] M. C. Kolios, *et al.*, "Ultrasonic spectral parameter characterization of apoptosis," *Ultrasound in Medicine and Biology,* vol. 28, pp. 589-597, May 2002.

[65] B. Banihashemi, *et al.*, "Novel low-frequency ultrasound monitoring of tumor cell death in response to therapy," *International Journal of Radiation Oncology Biology Physics,* vol. 72, pp. S684-S684, 2008.

[66] W. A. N. Dorland, *Dorland's pocket medical dictionary*, 27th ed. Philadelphia: Elsevier/Saunders, 2004.

[67] F. Davignon, *et al.*, "A parametric imaging approach for the segmentation of ultrasound data," *Ultrasonics,* vol. 43, pp. 789-801, Dec 2005.

[68] J. A. Noble, "Ultrasound image segmentation and tissue characterization," *Proceedings of the Institution of Mechanical Engineers Part H-Journal of Engineering in Medicine,* vol. 224, pp. 307-316, 2010.

[69] R. M. Vlad, *et al.*, "Quantitative Ultrasound Characterization of Cancer Radiotherapy Effects in Vitro," *International Journal of Radiation Oncology Biology Physics,* vol. 72, pp. 1236-1243, Nov 15 2008.

[70] R. M. Vlad, *et al.*, "High-frequency ultrasound for monitoring changes in liver tissue during preservation," *Physics in Medicine and Biology,* vol. 50, pp. 197-213, Jan 21 2005.

[71] D. Nir, "System and method for analysis of a tissue," Patent US 6785570 B2, Aug 2004.

[72] J. Braeckman, *et al.*, "Computer-aided ultrasonography (HistoScanning): a novel technology for locating and characterizing prostate cancer," *BJU Int,* vol. 101, pp. 293-8, Feb 2008.

[73] L. S. WILKINSON, *et al.*, "Breast HistoScanning - The development of a novel technique to improve tissue characterization during breast ultrasound," in *European Congress of Radiology*, Wien, pp. C-0596, 2011.

[74] R. Gutierrez-Osuna. *Cepstral Analysis*. Available: http://research.cs.tamu.edu/prism/lectures/sp/l9.pdf

[75] K. A. Wear, *et al.*, "Application of Autoregressive Spectral-Analysis to Cepstral Estimation of Mean Scatterer Spacing," *Ieee Transactions on Ultrasonics Ferroelectrics and Frequency Control,* vol. 40, pp. 50-58, Jan 1993.

[76] Y. Bige, *et al.*, "Analysis of microstructural alterations of normal and pathological breast tissue in vivo using the AR cepstrum," *Ultrasonics,* vol. 44, pp. 211-215, Feb 2006.

[77] S. Wan, *et al.*, "Robust deconvolution of high-frequency ultrasound images using higher-order spectral analysis and wavelets," *Ieee Transactions on Ultrasonics Ferroelectrics and Frequency Control,* vol. 50, pp. 1286-1295, Oct 2003.

[78] N. Mannicke, *et al.*, "Application of cepstral analysis for ultrasonic structural parameter characterization," *Biomedizinische Technik,* vol. 55, pp. 104-107107, Oct. 2010.

[79] R. S. Mia*, et al.*, "Quantitative ultrasound tissue characterization using texture and cepstral features," in *Medical Imaging 1998: Image Processing, Pts 1 and 2*. vol. 3338, pp. 211-219, 1998.

[80] C. Scott. (2006, Jan 2014). *EECS 559 Lecture notes: Advanced Signal Processing, University of Michigan*. Available: http://web.eecs.umich.edu/~cscott/past_courses/eecs559/index.html

[81] S. M. Kay and S. L. Marple, "Spectrum Analysis - a Modern Perspective," *Proceedings of the Ieee,* vol. 69, pp. 1380-1419, 1981.

[82] J. M. Gorce*, et al.*, "Processing radio frequency ultrasound images: A robust method for local spectral features estimation by a spatially constrained parametric approach," *Ieee Transactions on Ultrasonics Ferroelectrics and Frequency Control,* vol. 49, pp. 1704-1719, Dec 2002.

[83] E. von Lavante and J. A. Noble, "Improving the contrast of breast cancer masses in ultrasound using an autoregressive model based filter," *Medical Image Computing and Computer-Assisted Intervention - MICCAI 2007, Pt 1, Proceedings,* vol. 4791, pp. 153-160, 2007.

[84] B. Alacam*, et al.*, "Breast tissue characterization using FARMA modeling of ultrasonic RF echo," *Ultrasound in Medicine and Biology,* vol. 30, pp. 1397-1407, Oct 2004.

[85] S. M. Kay, *Modern spectral estimation : theory and application*. Englewood Cliffs, N.J.: Prentice Hall, 1988.

[86] D. H. Evans and W. N. McDicken, *Doppler ultrasound : physics, instrumentation, and signal processing*, 2nd ed. Chichester: Wiley, 2000.

[87] F. Tranquart, *et al.*, "Clinical use of ultrasound tissue harmonic imaging," *Ultrasound in Medicine and Biology,* vol. 25, pp. 889-894, Jul 1999.

[88] M. A. Averkiou, "Tissue harmonic imaging," in *2000 Ieee Ultrasonics Symposium Proceedings, Vols 1 and 2*, pp. 1563-1572, 2000.

[89] F. A. Duck, "Nonlinear acoustics in diagnostic ultrasound," *Ultrasound in Medicine and Biology,* vol. 28, pp. 1-18, Jan 2002.

[90] C. M. Sehgal, *et al.*, "A review of breast ultrasound," *Journal of Mammary Gland Biology and Neoplasia,* vol. 11, pp. 113-123, Apr 2006.

[91] E. L. Rosen and M. S. Soo, "Tissue harmonic imaging sonography of breast lesions improved margin analysis, conspicuity, and image quality compared to conventional ultrasound," *Clinical Imaging,* vol. 25, pp. 379-384, Nov-Dec 2001.

[92] K. T. Szopinski, *et al.*, "Tissue harmonic imaging - Utility in breast sonography," *Journal of Ultrasound in Medicine,* vol. 22, pp. 479-487, May 2003.

[93] K. Ferrara and G. DeAngelis, "Color flow mapping," *Ultrasound in Medicine and Biology,* vol. 23, pp. 321-345, 1997.

[94] D. O. Cosgrove, *et al.*, "BREAST DISEASES - COLOR DOPPLER US IN DIFFERENTIAL-DIAGNOSIS," *Radiology,* vol. 189, pp. 99-104, Oct 1993.

[95] S. Raza and J. K. Baum, "Solid breast lesions: Evaluation with Power Doppler US," *Radiology,* vol. 203, pp. 164-168, Apr 1997.

[96] S. W. Lee, *et al.*, "Role of color and power Doppler imaging in differentiating between malignant and benign solid breast masses," *Journal of Clinical Ultrasound,* vol. 30, pp. 459-464, Oct 2002.

[97] R. L. Birdwell*, et al.*, "Preliminary experience with power Doppler imaging of solid breast masses," *American Journal of Roentgenology,* vol. 169, pp. 703-707, Sep 1997.

[98] T. H. Wilkens*, et al.*, "Evaluation of palpable breast masses with color Doppler sonography and gray scale imaging," *Journal of Ultrasound in Medicine,* vol. 17, pp. 109-115, Feb 1998.

[99] C. M. Sehgal*, et al.*, "Quantitative vascularity of breast masses by Doppler imaging: Regional variations and diagnostic implications," *Journal of Ultrasound in Medicine,* vol. 19, pp. 427-440, Jul 2000.

[100] R. T. Ribeiro*, et al.*, "Improving breast mass visibility in ultrasound images using spectral analysis and contrast enhancement algorithms," *Imaging and Signal Processing in Health Care and Technology*, Baltimore, MD, pp. 5-9, 2012.

[101] Z. Wang and A. C. Bovik, "A universal image quality index," *Ieee Signal Processing Letters,* vol. 9, pp. 81-84, Mar 2002.

[102] B. Furht and O. Marques, *Handbook of Video Databases: Design and Applications*: CRC Press, 2003.

[103] R. Taylor, "Interpretation of the Correlation-Coefficient - a Basic Review," *Journal of Diagnostic Medical Sonography,* vol. 6, pp. 35-39, Jan-Feb 1990.

[104] C. E. Shannon, "A Mathematical Theory of Communication," *Bell System Technical Journal,* vol. 27, pp. 623-656, 1948.

[105] C. Kingsford. (2009, Jan 2014). *Information Theory Hints, CMSC 858L lecture notes: Graphs and Networks in Computational Biology, University of*

Maryland. Available: http://www.cs.umd.edu/class/spring2009/cmsc858l/InfoTheoryHints.pdf

[106] M. Meila, "Comparing clusterings - an information based distance," *Journal of Multivariate Analysis,* vol. 98, pp. 873-895, May 2007.

[107] N. X. Vinh*, et al.*, "Information Theoretic Measures for Clusterings Comparison: Variants, Properties, Normalization and Correction for Chance," *Journal of Machine Learning Research,* vol. 11, pp. 2837-2854, Oct 2010.

[108] D. B. Russakoff*, et al.*, "Image similarity using mutual information of regions," *Computer Vision - Eccv 2004, Pt 3,* vol. 3023, pp. 596-607, 2004.

[109] K. J. Parker*, et al.*, "Imaging the elastic properties of tissue: the 20 year perspective," *Physics in medicine and biology,* vol. 56, pp. R1-R29, 2011.

[110] J. Ophir*, et al.*, "Elastography: A Decade of Progress (2000-2010)," *Current Medical Imaging Reviews,* vol. 7, pp. 292-312, Nov 2011.

[111] R. G. Barr, "Sonographic Breast Elastography," *Journal of Ultrasound in Medicine,* vol. 31, pp. 773-783, May 2012.

[112] R. E. English*, et al.*, "A pilot study to evaluate assisted freehand ultrasound elasticity imaging in the sizing of early breast cancer: a comparison of B-mode and AFUSON elasticity ultrasound with histopathology measurements," *British Journal of Radiology,* vol. 84, pp. 1011-1019, Nov 2011.

[113] A. Sarvazyan*, et al.*, "An Overview of Elastography-An Emerging Branch of Medical Imaging," *Current Medical Imaging Reviews,* vol. 7, pp. 255-282, Nov 2011.

[114] A. Di Battista, "Ultrasound Elastography Techniques for the Therapeutic Monitoring of Breast Cancer," DPhil, Engineering Science, University of Oxford, UK, 2011.

[115] A. Di Battista and J. A. Noble, "A fast and robust 3D ultrasound strain imaging algorithm for freehand scanning," in *IEEE International Symposium on Biomedical Imaging: From Nano to Macro*, 2011, pp. 528-531.

[116] F. Pinto*, et al.*, "Imaging in Prostate Cancer Diagnosis: Present Role and Future Perspectives," *Urologia Internationalis,* vol. 86, pp. 373-382, 2011.

[117] M. Smeenge*, et al.*, "Current status of transrectal ultrasound techniques in prostate cancer," *Current Opinion in Urology,* vol. 22, pp. 297-302, Jul 2012.

[118] D. A. Clevert*, et al.*, "Latest developments in ultrasound of the liver," *Radiology,* vol. 51, pp. 661-670, Aug 2011.

[119] J.-D. Lin*, et al.*, "Clinical applications of thyroid ultrasonography," *Endocrinologist,* vol. 16, pp. 319-322, Nov-Dec 2006.

[120] J. I. Lew*, et al.*, "Developments in the use of ultrasound for thyroid cancer," *Current Opinion in Oncology,* vol. 22, pp. 11-16, Jan 2010.

[121] M. Kadour, "Guide to Making Phantoms " Medical Vision Laboratory, Oxford University, 2003.

[122] T. J. Hall*, et al.*, "Phantom materials for elastography," *IEEE Transactions on Ultrasonics, Ferroelectrics, and Frequency Control,* vol. 44, pp. 1355-1365, 1997.

[123] R. C. Gonzalez and R. E. Woods, *Digital image processing*, 3rd ed. Upper Saddle River, N.J.: Prentice Hall, 2008.